Modeling, Design and Fabrication of MEMS Filters for RF Applications

Siamak Fouladi Azarnaminy

A Thesis

in

The Department

of

Electrical and Computer Engineering

Presented in Partial Fulfillment of the Requirements
for the Degree of Master of Applied Science at
Concordia University
Montreal, Quebec, Canada

April 2005

© Siamak Fouladi Azarnaminy, 2005

Library and
Archives Canada

Published Heritage
Branch

395 Wellington Street
Ottawa ON K1A 0N4
Canada

Bibliothèque et
Archives Canada

Direction du
Patrimoine de l'édition

395, rue Wellington
Ottawa ON K1A 0N4
Canada

Your file Votre référence
ISBN: 0-494-04369-5
Our file Notre référence
ISBN: 0-494-04369-5

NOTICE:
The author has granted a non-exclusive license allowing Library and Archives Canada to reproduce, publish, archive, preserve, conserve, communicate to the public by telecommunication or on the Internet, loan, distribute and sell theses worldwide, for commercial or non-commercial purposes, in microform, paper, electronic and/or any other formats.

The author retains copyright ownership and moral rights in this thesis. Neither the thesis nor substantial extracts from it may be printed or otherwise reproduced without the author's permission.

AVIS:
L'auteur a accordé une licence non exclusive permettant à la Bibliothèque et Archives Canada de reproduire, publier, archiver, sauvegarder, conserver, transmettre au public par télécommunication ou par l'Internet, prêter, distribuer et vendre des thèses partout dans le monde, à des fins commerciales ou autres, sur support microforme, papier, électronique et/ou autres formats.

L'auteur conserve la propriété du droit d'auteur et des droits moraux qui protège cette thèse. Ni la thèse ni des extraits substantiels de celle-ci ne doivent être imprimés ou autrement reproduits sans son autorisation.

In compliance with the Canadian Privacy Act some supporting forms may have been removed from this thesis.

While these forms may be included in the document page count, their removal does not represent any loss of content from the thesis.

Conformément à la loi canadienne sur la protection de la vie privée, quelques formulaires secondaires ont été enlevés de cette thèse.

Bien que ces formulaires aient inclus dans la pagination, il n'y aura aucun contenu manquant.

ABSTRACT

Modeling, Design, and Fabrication of MEMS Filters for RF Applications

Siamak Fouladi Azarnaminy

Currently, micro electro mechanical systems (MEMS) technology has been used in the fabrication and development of several micro devices which cover a broad range of applications. One of these application areas is the telecommunication industry. Current multi-band communication systems depend on off-chip components for frequency selection stages. Since the fabrication of these off-chip components are not compatible with IC fabrication, the electrical connection has to be in the board level, increasing the cost, size and system complexity. Recently MEMS technology has been used in constructing tunable IC components for RF and wireless transceivers, such as resonators, variable capacitors and inductors. These on-chip components can be utilized to implement system on chip (SOC) transceiver architectures with a better performance.

This project is focused on modeling, design, and fabrication of band-pass filters for RF applications using MEMS components. The first class of filters is based on MEMS resonators covering a frequency range from 1MHz to 10MHz and the second class of filters use RF MEMS tunable capacitors. The project has two main parts; the first part is dedicated to the behavioral modeling and generating macro models for MEMS resonators that will be used in system level simulation of the final filter, and the second part discusses the design, fabrication, and post processing of both the MEMS resonators and MEMS variable capacitor, besides the experimental results.

ACKNOWLEDGEMENTS

First of all, I would like to sincerely thank my supervisor, Dr. Mojtaba Kahrizi, who gave me the opportunity to start my masters and without his support, advice, and valuable instructions, I would never be able to achieve my academic goals.

Also I want to thank Canadian Microelectronics Corporation (CMC) for their support in providing the access for fabrication facilities and the simulators for our research group, the Department of Mechanical Engineering for the access to do the bonding, and also the Microwave Laboratory at Electrical and Computer Engineering Department for their help in doing the RF measurements. The financial support of this project was provided by Natural Sciences and Engineering Research Council of Canada (NSERC), without their continuous support, this project would not be accomplished.

Also I wish to express my truly appreciation to my friends and colleagues in the microelectronic device laboratory, especially Alireza for his help in doing the post-processing steps, Dr. Victor Rossokhaty, our lab supervisor Shailesh, and Jun Chen for their help and support in gathering the experimental results.

Finally, I would like to express my deepest appreciation to my family; to my parents for their motivation and love, my uncle who is my best teacher and without his support, life in Canada was impossible for me as an international student, and at last but not least, my dear brothers, they are the only ones giving me the enthusiasm in achieving my goals.

TABLE OF CONTENTS

List of Figures......VIII

List of Tables......XII

Nomenclature......XIII

Chapter 1 Introduction......1

1.1 An Introduction to MEMS and RF MEMS......1

1.1.1 RF MEMS Classification......2

1.1.2 RF MEMS Switches......2

1.1.3 MEMS Inductors and Capacitors......3

1.1.4 Micromachined RF Filters......6

1.1.5 Micromachined Phase Shifters......7

1.1.6 Micromachined Transmission Lines......8

1.1.7 Micromachined Antenna......9

1.2 MEMS Fabrication Technologies......10

1.2.1 Bulk Micromachining......10

1.2.2 Surface Micromachining......11

1.2.3 Wafer Bonding......12

1.2.4 LIGA Process......14

1.2.5 PolyMUMPs and CMOS Foundry Services......15

1.3 RF MEMS Integration......16

1.4 Modeling Methodologies......19

1.5 Thesis Outline......21

Chapter 2 Theory, Modeling, and Simulation of MEMS Band-Pass Filters......22

2.1 Theory of Band-Pass Filters......22

2.1.1 Preliminary Definitions 23

2.1.2 Filter Design Methods......24

2.1.3 Image Parameter Method......25

2.1.4 Insertion Loss Method....27
2.1.5 Filter Transformations....28
2.2 Microelectromechanical Band-Pass Filters....29
2.2.1 MEMS Resonators....30
2.2.2 Theoretical Concepts and Modeling of MEMS Resonators....31
2.2.3 Flexural-Mode Beam Resonator....33
2.2.4 Flexural-Mode Disk Resonator....39
2.2.5 Lumped-Element Mechanical Modeling of Resonators....42
2.2.6 Lumped-Element Electrical Modeling of Resonators....44
2.2.7 Theory of Coupled Resonators....51
2.2.8 Coupling Element....58
2.2.9 Lumped-Element Modeling of Filters....62
2.2.10 Behavioral Modeling and System-Level Simulation....63
2.3 MEMS Variable Capacitors for Filtering Applications....72
2.3.1 Filter Topologies Based on MEMS Capacitors....72
2.3.2 MEMS Variable Capacitors....74

Chapter 3 Design and Fabrication....78
3.1 Flexural-Mode Clapmed-Clamped Beam Resonator....78
3.2 Flexural-Mode Cantilever Beam Resonator....86
3.3 Flexural-Mode Disk Resonator....89
3.4 Microelectromechanical Band-Pass Filter....91
3.5 Fabrication Results....93
3.6 Post-Processing for MUMPs....93
3.7 Variable MEMS Capacitor....93
3.7.1 Design of the Variable MEMS Capacitor....95
3.7.2 Post-Processing for the Variable MEMS Capacitor....98

Chapter 4 Experimental Setup and Results....105
4.1 Bonding and Packaging....105
4.2 Experimental Setup and Results for the MEMS Resonators....106

4.3 Fiber Optic Interferometer....................115
4.4 Experimental Setup and Results for the MEMS Variable Capacitor....................117
Chapter 5 Conclusions and Future Work....................120
5.1 Conclusions....................120
5.2 Contributions....................121
5.3 Future Work....................122

References....................124

List of Figures

1.1 Top and cross-section view of a shunt RF MEMS switch.
1.2 Planar spiral and 3-dimensional solenoid inductors
1.3 Parallel-Plate and Comb-Finger Capacitors
1.4 SEM of a folded-beam micromechanical filter
1.5 A V-band 2-bit MEMS phase shifter based on shunt switches
1.6 Micromachined GSG coplanar waveguide with RF input pads
1.7 Bulk micromachining techniques
1.8 Surface micromachining process steps
1.9 Anodic bonding
1.10 The LIGA process
1.11 Cross-sectional view of PolyMUMPs process
1.12 TSMC CMOS 0.35μm layer stack and the thickness of layers in (μm)
1.13 Flip-chip transfer process steps
2.1 Filter as a two-port network
2.2 Amplitude response, low-pass, high-pass, band-pass, band-stop
2.3 The main characteristics for a band-pass filter
2.4 Constant-k (T) filter sections
2.5 High-pass and Low-pass m-derived (T) sections
2.6 Low-pass composite filter
2.7 Butterworth and Chebyshev filter approximations (N=3, k=1)
2.8 Ladder circuits for low-pass filter prototypes
2.9 Series and parallel RLC resonators
2.10 Perspective view of a clamped-clamped beam micromechanical resonator
2.11 Fundamental flexural-mode beam
2.12 Normalized fundamental resonance frequency, n=1, as a function of beam length/thickness ratio
2.13 Fundamental, 2nd, 3rd, and 4th flexural modal shapes of the clamped-clamped MEMS resonator
2.14 Flexural-Mode disk resonator

2.15 Four lowest flexural vibration modes of a disk resonator
2.16 Schematic view of the MEMS disk resonator
2.17 Lumped-element mechanical modeling of the clamped-clamped beam resonator
2.18 A schematic view of a two-port electromechanical transducer
2.19 Elementary parallel plate electrostatic transducer
2.20 A transverse electrostatic transducer stabilized with a spring
2.21 Equivalent circuit representations of the transverse electrostatic transducer
2.22 An equivalent electrical circuit representation of the MEMS resonator
2.23 Mechanical model for two coupled resonators
2.24 Amplitude and phase response of two coupled resonators versus ω / ω_i
2.25 Amplitude response for three different Q-factors
2.26 Coupled resonators in open ring and closed ring configurations
2.27 Frequency response of each resonator, in a system of four coupled resonators
2.28 Coupled MEMS resonators
2.29 Flexural coupling element and its equivalent transmission line model
2.30 Equivalent electrical model of the flexural coupling element
2.31 Normalized velocity along the beam length
2.32 Lumped-Element mechanical model of the microelectromechanical filter
2.33 Lumped-Element electrical model of the microelectromechanical filetr
2.34 System level modeling methodologies
2.35 Two port electromechanical transducer
2.36 Behavioral macromodel for the transverse electrostatic transducer
2.37 Equivalent large-signal electrical macromodel
2.38 Macromodel of the filter based on ROM
2.39 Harmonic analysis of the band-pass filter using different macromodels
2.40 Frequency response of the closed-ring and open-ring configurations
2.41 Frequency response for different quality factors
2.42 Lumped-element and distributed-element filter topologies based on MEMS capacitors
2.43 Conventional lumped-element band-pass filter and the one using impedance inverters

2.44 Schematic view of parallel-plate MEMS capacitor
2.45 Pull-in voltage and equilibrium points for the parallel-plate capacitor
3.1 Clamped-Clamped flexural beam resonator
3.2 Two different models used for the modal analysis of the resonator
3.3 Fundamental modal frequency versus beam length
3.4 SEM picture of the 10MHz clamped-clamped MEMS resonator
3.5 Frequency response of the 10MHz clamped-clamped MEMS resonator Frequency response of the 10MHz clamped-clamped MEMS resonator
3.6 Beam deformation, because of the applied DC bias voltage $V_P = 80V$
3.7 Flexural-mode cantilever beam resonator
3.8 Transverse modal shapes of the cantilever beam resonator
3.9 Frequency response of the cantilever MEMS resonator
3.10 Flexural-Mode disk resonator
3.11 Deformation of the disk resonator under $V_P = 80V$
3.12 Frequency response of the disk resonator
3.13 Microelectromechanical band-pass filter
3.14 Frequency response of the 10MHz band-pass filter
3.15 SEM picture of the clamped-clamped MEMS resonators (first MUMPs design)
3.16 Layout of the second MUMPs design
3.17 Top and cross-section views of a two parallel-plate MEMS tunable capacitor
3.18 Transient response and C-V characteristic of a MEMS capacitor
3.19 Diagram of the suspension beam
3.20 Oxide removal for MEMS structures
3.21 The fabricated CMOS chip and the mask which will be used for post-processing
3.22 A photograph of the chip after depositing the photoresist layer
3.23 SEM image of the device after removing the oxide layer
3.24 SEM image of the final variable MEMS capacitor after post-processing steps
3.25 TMAH setup
3.26 Anisotropic etching followed by isotropic etching with XeF_2
4.1 Bonded devices
4.2 MEMS resonator as a two port network

4.3 S21 measurement with network analyzer
4.4 Bias-Tee as a three port component
4.5 Experimental setup for the MEMS resonators
4.6 Schematic view of the test setup
4.7 Schematic view of the JFET amplifier
4.8 Simulated gain of the JFET amplifier
4.9 MEMS chip and the required electronic circuitry
4.10 Measured amplitude response of the 10MHz MEMS resonator
4.11 Resonance frequency versus DC bias voltage
4.12 Resonance frequency versus beam length
4.13 Fiber optic Fabry-Perot interferometer
4.14 A single mode optical fiber with a diameter less than 10μm
4.15 RF test fixture and the clamped chip
4.16 MEMS capacitor in GSG configuration
4.17 Measured S11 parameter for the MEMS capacitor

List of Tables

1.1 PolyMUMPs layers and their functionalities

2.1 Direct electromechanical analogy

2.2 Roots of the frequency equation for different boundary conditions

2.3 Characteristics of Flexural-Mode clamped-clamped beam resonator

2.4 Constitutive and Transfer equations of the transverse electrostatic transducer

2.5 Design specifications and geometries of the 10MHz band-pass filter

2.6 Element values for the small signal electrical macromodel

2.7 10MHz filter characteristics using different macromodels and the error with respect to the FEM results

2.8 Fourier analysis results

3.1 Material properties for different layers in PolyMUMPs

3.2 Modal frequencies obtained theoretically and using FEM simulation results

3.3 Design specifications and geometries of the clamped-clamped resonator

3.4 Design specifications and geometries of the Cantilever MEMS resonator

3.5 Design specifications and geometries of the Disk resonator

3.6 Design specifications and geometries of the 10MHz band-pass Filter

3.7 Summary of selected CMOS 0.35 μm process parameters

3.8 CMOS post-processing steps

Nomenclature

A .... Beam cross-section
B .... Constitutive matrix
C_o .... Bias point capacitance
$C(x_t)$ .... Transducer's capacitance
C_r .... Damping constant
c .... Propagation velocity
d_{ox} .... Thickness of oxide
d_o .... Electrode to beam gap
$D(x)$ .... Damping of resonator
E .... Young's Modulus
F_{elec} .... Electrostatic force
F_{net} .... Effective force
f_n .... Modal resonance frequency
F_t .... Total electromechanical force
f_i .... Applied force on each resonator
G .... Shear modulus
h .... Beam thickness
$H(j\omega)$ .... Filter transfer function
I .... Bending moment of inertia
IL .... Insertion loss
i_o .... Output current
$K(x)$ .... Stiffness of resonator
$K.E.$ .... Total kinetic energy
$k_n l$ .... Roots of frequency equation
k_r .... Resonator stiffness
k_{rc} .... Stiffness at the coupling point

k_s .... Stiffness of coupling element

l_c .... Coupling location

L_r .... Beam length

L_s .... Coupling beam length

m_r .... Resonator mass

m_{rc} .... Resonator mass at coupling point

$M(x)$ .... Mass of resonator

M_{eq} .... Equivalent mass of resonator

N .... Filter order

P_{LR} .... Power loss ratio

Q .... Quality factor

Q_{fltr} .... Filter quality factor

Q_{res} .... Quality factor of the resonator

q_0 .... Bias charge

q_t .... Electric charge

R_0 .... Source impedance

R_t .... Termination resistor

t .... Beam thickness

T .... Transfer matrix

$u(x,t)$ .... Displacement

v_0 .... Bias voltage

V_{in} .... Input voltage

$V(x)$ .... Velocity

V_p .... DC bias voltage

V_{PI} .... Pull-in voltage

W_e .... Electrode width

W_{em} .... Electromechanical energy

W_r .... Beam Width

W_s .... Coupling beam width

w .... Beam width

$X(j\omega)$ .... Phasor of the filter output

x_r .... Spring rest position

x_t .... Total displacement

x_{PI} .... Pull-in gap

$Y(j\omega)$ .... Phasor of the filter input

$[C]$ .... Damping matrix

$[K]$ .... Stiffness matrix

$[M]$ .... Mass matrix

$\{F\}$ .... Externally applied force

$\{X\}$ .... Generalized coordinates

ω_o .... Filter center frequency

$\Delta\omega$ .... Filter band-width

ω_c .... Cutoff frequency

ω_1 .... First edge of the pass-band

ω_2 .... Second edge of the pass-band

$\phi(\omega)$ .... Phase response

ρ .... Density

ν .... Poisson's ratio

κ .... Shape factor

ε_o .... Free space permittivity

ε_{ox} .... Oxide relative permittivity

Γ .... Transduction factor

η_c .... Transformer turn ratio

κ .... Modification factor

υ .... Normalized voltage

Chapter 1
Introduction

1.1 An Introduction to MEMS and RF MEMS

Micro electro mechanical systems or MEMS is a fast growing technology in fabricating several components and devices with small dimensions ranging from a few micrometers to a few millimeters, using the very large-scale integrated circuit fabrication technologies. The main advantage of using integrated circuit (IC) technology for MEMS is lower cost through the batch fabrication and mass-production. As another benefit, recent progresses in lithography techniques have enabled us to implement tiny MEMS devices with a sub-micrometer feature size.

Generally MEMS covers a broad range of systems and devices which combine the electronic and non-electronic elements besides each other to perform complex functions including several domains such as, electrical, mechanical, thermal, magnetic, fluidic, and optics. There are numerous applications for MEMS in automotive, military, medical, telecommunications and aerospace industries. For example silicon micro-accelerometers are the first commercialized MEMS devices which have found their application in the automotive industry. As another example biomedical applications exploit the capabilities of silicon micromachining in the medical blood pressure sensors. Micro electro mechanical systems for radio frequency applications, known as RF MEMS, are expected to be the next breakthrough in MEMS devices because of their potential in replacing the current board-level wireless receiver and transmitter architectures with fully integrated communication systems made only on a single chip.

RF MEMS provides a class of new devices and components which display superior high-frequency performance relative to conventional semiconductor devices. A key advantage of the RF MEMS devices compared to semiconductor counterparts is the electromechanical isolation which means that the RF circuit does not couple significantly to the actuation circuit. Lower power consumption is another advantage, in many of the RF MEMS devices the electrostatic actuation occurs within an air gap or vacuum and as a result there is no static power dissipation. However, besides all of these improvements, there are some disadvantages such as lower actuation or switching speed, typically in the

rage of a few hundred microseconds or grater, which is far longer than the semiconductor equivalents. Another disadvantage is a mechanical phenomenon called "stiction" which means the adhesion of microstructures to neighboring surfaces due to the inherent proximity between the structural parts. For some specific RF MEMS components there are some other benefits through the MEMS technology which will be explained later on.

1.1.1 RF MEMS Classification

The term RF MEMS does not necessarily refer to just micro electro mechanical systems operating at RF frequencies, in fact in a large number of RF MEMS devices the micro electro mechanical operation is just used for component adjustment, such as variable MEMS capacitors. Following [1] the RF MEMS terminology covers three classes of devices; *RF extrinsic* devices, where the MEMS structure is located outside the RF circuit, but actuates or controls other devices inside the circuit (ex. tunable micro-machined transmission lines), *RF intrinsic,* where the MEMS structure is located inside the circuit and has the dual, but decoupled actuation and RF functionalities (ex. shunt RF switches and MEMS capacitors) and finally *RF reactive,* where the RF and actuation functionalities are coupled to each other for example micromechanical resonators are categorized in this class of RF MEMS devices. In terms of application RF MEMS components can be categorized into six distinct areas: RF MEMS switches, MEMS inductors and capacitors, micromachined RF filters, micromachined phase shifters, micromachined transmission lines, and micromachined antenna.

1.1.2 RF MEMS Switches

To date several RF MEMS switches have been developed and tested. They are the most extensively studied components and play an important role in any RF system. The main application areas of RF MEMS switches, in the telecommunication industry, are for signal routing, impedance matching, and for changing the gain of amplifiers [2]. Telecommunication covers a broad frequency range from below HF range to higher Ku-band (12~18GHz) or even upper side of W band (75~110 GHz), which require the use of high quality RF switches. Besides the wide frequency spectrum other important requirements for RF MEMS switches are their power consumption, insertion loss,

isolation, and linearity. There are two basic configurations for RF MEMS switches; shunt and push-pull series switches. As an example Figure 1.1 shows a shunt switch in coplanar waveguide (CPW) configuration. It consists of a bridge which is anchored at both ends on the ground lines and a drive electrode located a distance g below the bridge. The bridge can be electrostatically actuated by applying a DC pull-in voltage between the drive electrode and the bridge itself. The drive electrode is coated with a thin dielectric layer which prevents from short circuit when the switch is in the on state [3].

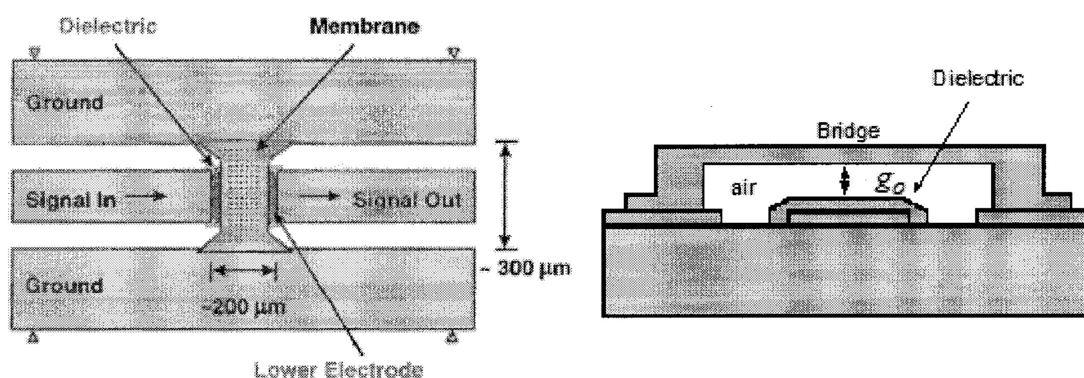

Fig. 1.1 Top and cross-section view of a shunt RF MEMS switch.

The device switches between two capacitance states; C_{off} and C_{on}, and it is designed so that C_{off} is smaller than line capacitance and in the on state, C_{on} is big enough to make an effective short circuit between the signal path and ground lines at RF frequencies. A topic of research for this kind of switches is the lowering of actuation voltage to levels compatible with IC technologies about 5V or lower, by using different support configurations and increasing dielectric constant [2].

1.1.3 MEMS Inductors and Capacitors

For the frequency selection stages of high frequency communication subsystems, such as voltage controlled oscillators (VCO) and tunable filters, we need components with higher quality factor, Q. The Q-factor of conventional spiral inductors and junction diode capacitors are less than the minimum required values for high frequency applications and as a result the off-chip counterparts have gained more popularity for RF applications.

However, since these components can not be integrated on the same chip, they impose a bottleneck in the miniaturization of RF front ends. Fully integrated inductors and capacitors can be fabricated using the MEMS technology and these devices benefit from smaller size, lower power consumption, and lower costs through the mass production.

MEMS inductors can be fabricated in two different configurations; planar spiral inductors and three dimensional solenoid inductors. The planar spiral inductors fabricated on a conductive substrate such as silicon suffer from the parasitic capacitance between the metal traces and the substrate. The parasitic capacitance results in lowering the self resonance frequency of the inductor. For example inductors fabricated on semi-insulating GaAs substrate and insulating sapphire wafers have exhibited a self-resonance frequency around 3 GHz while the ones fabricated on standard silicon wafer have a self-resonance frequency less than 2GHz [2]. Another issue for the planar inductors is the substrate loss which reduces the Q-factor of the final inductor. This drawback can be treated by using etching techniques and removing a part of the substrate under the component. Three dimensional MEMS inductors fabricated using surface micromachining techniques are expected to show a better performance compared to the planar spiral inductors, because in these inductors only one portion of the metal traces are facing the substrate. Figure 1.2 shows a bulk micromachined spiral inductor fabricated on a silicon substrate and its three dimensional solenoid counterpart.

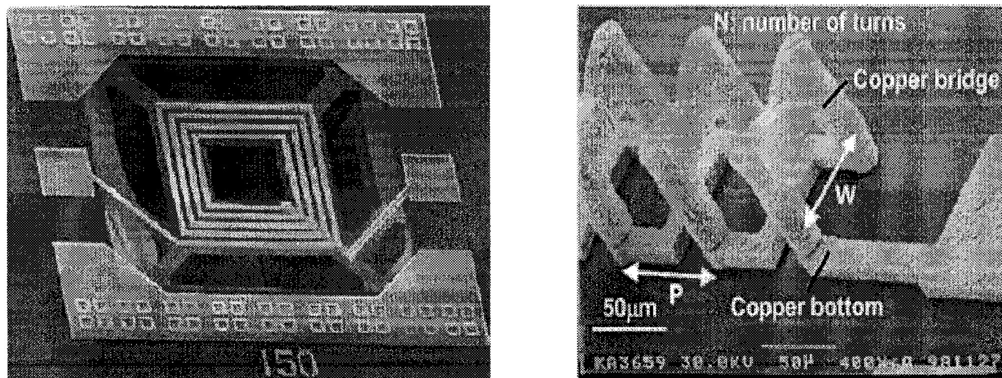

Fig. 1.2 Planar spiral and 3-dimensional solenoid inductors [4, 5].

MEMS tunable capacitors can be classified based on their configuration and the actuation mechanism. In terms of configuration there are two types of MEMS capacitors;

parallel-plate and comb finger capacitors. The parallel plate capacitors are simple to be fabricated and also they can be designed for larger capacitance values, but in terms of tuning range because of the pull-in voltage effect the theoretical maximum tuning range is 1.5:1. The two actuation mechanisms are thermal and electrostatic actuations, thermal actuation results in larger tuning range and linear characteristic while increasing the power consumption. On the other hand for the electrostatic actuation the DC power consumption is almost zero and also it benefits from higher switching speed.

Like the MEMS inductors, the fabricated MEMS capacitors suffer from low Q-factor at RF frequency range due to the stray capacitance between the bottom plate and the silicon substrate which produces high insertion losses. Flip-Chip technology can be used to transfer the fabricated devices to another alumina substrate by an extra fabrication cost or as explained for MEMS inductors, bulk micromachining techniques can be used to etch the silicon substrate and improve the Q-factor of the MEMS variable capacitors at RF frequency range. Figure 1.3, presents the parallel-plate and comb-finger configurations, the 3.26PF parallel-plate tunable capacitor shown in this figure has a maximum Q-factor of 13.6 at 1 GHz and a tuning range of 1.5:1 with an actuation voltage of less than 3.5V [6]. The 1.4PF comb finger MEMS capacitor has a wide tuning range of 8.4:1 and a Q-factor above 30 at 2.25GHz, making it suitable for high frequency applications. The Q-factor for this design has been improved by using a glass substrate instead of conductive silicon substrates. The actuation voltage is around 30V which is larger than the parallel-plate configuration.

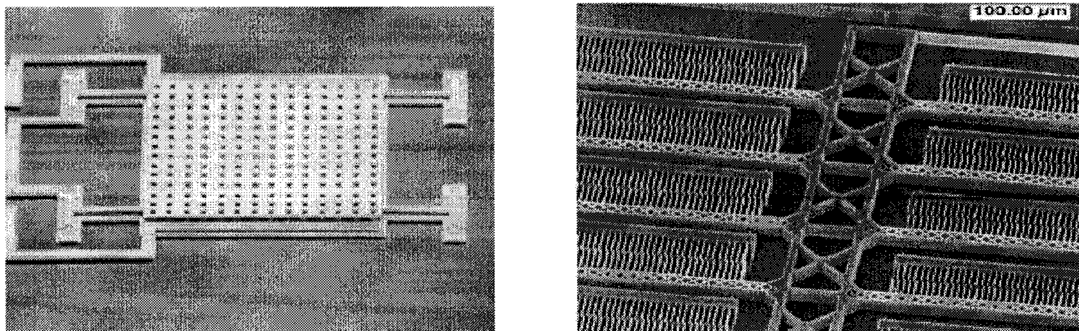

Fig. 1.3 Parallel-Plate and Comb-Finger Capacitors [6, 7]

1.1.4 Micromachined RF Filters

For present multi-band wireless applications one of the most important RF subsystems is the filtering stage which is used to select between many communication channels operating simultaneously. In terms of the transmitted frequency band, these filters can be classified as low-pass, band-pass, high-pass, and band-stop filters. However, in most communication systems the most widely used filters are the band-pass filters. The main characteristics for these band-pass filters are the insertion loss, center frequency, bandwidth, and out-of-band rejection ratio.

Conceptually the easiest way to implement a band-pass filter is to use lumped inductors and capacitors. However for high frequency RF applications this method is limited to the Q-factor of the constituent lumped element components. An alternative method is the digital filter that makes use of recent advances in high-speed signal processing techniques and high-speed processors, but this approach is again limited by the maximum sampling frequency. Another approach is the mechanical filters, from the early days of telecommunications various forms of mechanical filters have been used in systems that demand narrow bandwidth, low loss, and good stability. These requirements can be achieved with mechanical filters because of high Q and excellent temperature and aging characteristics of the mechanical resonators. Mechanical or more precisely electromechanical filters involve the transformation of electrical signals into the mechanical energy domain and after the filtering takes place in the mechanical domain the remaining signals are transformed back into the original electrical form at the output terminal. These mechanical filters are often composed of mechanically (acoustically) coupled mechanical resonators [8].

Among the most widely used mechanical filters are the quartz crystals and SAW filters, which are off-chip components interfacing with signal processing circuitry at the board level, and this constitutes a bottleneck to miniaturization and performance of superheterodyne transceivers. Recent developments in the micromachining technologies that make possible high-Q on-chip micromechanical resonators, suggest a method for miniaturizing and integrating highly selective filters alongside transistors [9]. Several MEMS micromechanical resonators have been fabricated using standard IC technologies for RF filters and oscillators, such as Free-Free Beam [10], Lateral Free-Free Beam [11],

Contour mode Disk [12], SOI-Based resonators with capacitive gaps [13] and Radial Bulk Annular Resonators [14]. The main advantage of micromechanical resonators is their high Q value approaching more than 10,000 and the only drawback is their relatively lower frequency range, however there are intensive efforts in increasing the applicable frequency range for this kind of resonators to higher UHF range, (900 MHz) and is the topic of ongoing research in micromechanical resonator design.

The resonators can be mechanically coupled to implement high frequency filters with applications in communication systems. The high Q factor of the constituting resonators results in very low insertion loss for the filter which is a main concern in filter design. By using different coupling configurations, number of resonators, and the coupling element dimensions, it is possible to design filters with the required frequency response. Figure 1.4 represents a micromechanical filter consisting of three coupled resonators. The filter has a center frequency of 455KHz and a band-width of 981Hz. The high-Q factor of the resonators which is around 40,000 results in a low insertion loss less than 0.26dB [15].

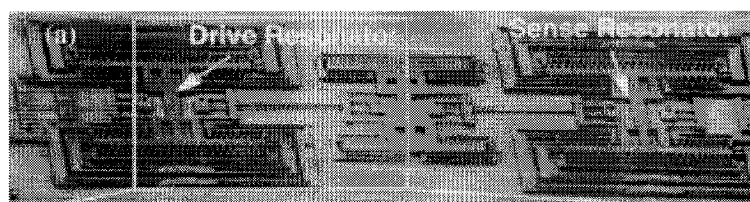

Fig. 1.4 SEM of a folded-beam micromechanical filter [15].

1.1.5 Micromachined Phase Shifters

A phase shifter is a two-port network providing a constant phase difference between the output and input terminals by a control dc bias voltage. Phase shifters are the key components in developing phased array antennas for microwave and millimeter wave applications. The main characteristics for a phase shifter are the insertion loss, bandwidth, power dissipation, and power handling capability. Conventionally these phase shifters have been fabricated using ferrite materials with a low insertion loss and superior power handling capabilities, but higher fabrication cost. Another approach is the semiconductor phase shifters using PIN diodes or FET which are less expensive and smaller in size than ferrite phase shifters however their applications are limited because of high insertion loss

[2]. At RF frequency range MEMS switches can be applied in designing low loss phase shifters using a coplanar waveguide (CPW) transmission line periodically loaded with shunt RF MEMS switches as shown in Figure 1.5. Since MEMS switches have very small up-state capacitance they result in a wider frequency band compared to the similar designs using solid-state devices and also MEMS switches can be fabricated directly with the antenna element on a single substrate, thereby resulting in low-cost phased arrays [16].

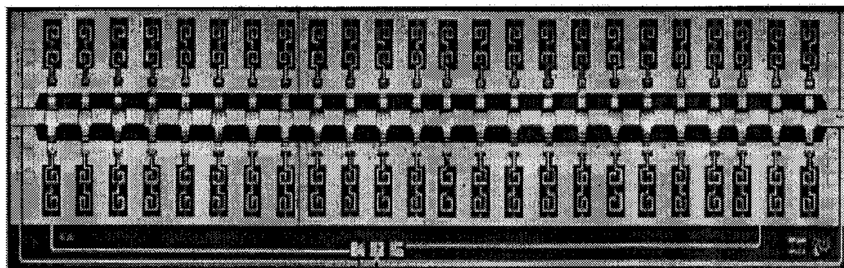

Fig. 1.5 A V-band 2-bit MEMS phase shifter based on shunt switches [17].

1.1.6 Micromachined Transmission Lines

RF transmission lines are usually used to carry signals from passive elements such as filters, capacitors, and inductors and to interconnect them. The most commonly used transmission lines in the microwave integrated circuits (MICs) are classified as microstrip, slotline, and coplanar waveguide structures. Among these structures coplanar waveguide (CPW) transmission lines have found a wide range of applications in MICs because of their flexibility in the circuit design. A conventional CPW on a dielectric substrate consists of a center strip conductor with semi-infinite ground planes on either side. The CPW offers several advantages over conventional microstrip line. First, it simplifies fabrication; second, it facilitates easy shunt as well as series surface mounting of active and passive devices; third, it eliminates the need for wraparound and via holes, and forth, it reduces radiation loss [18]. Furthermore the ground plane which exists between any two adjacent lines reduces the cross talk effects. As a result CPW circuits can be made denser than conventional microstrip circuits. These, as well as several other advantages, make CPW ideally suited for microwave integrated circuits.

Recent advances in micromachining techniques have been used to fabricate miniature microwave coplanar waveguides. For example the design and fabrication of a microwave

waveguide through a standard CMOS process with subsequent top-side etching is presented in [19]. Generally, the silicon substrate is not suitable for the fabricated microwave transmission lines due to the high losses at RF frequencies. The removal of the lossy silicon substrate in the vicinity of metal layers significantly improves the insertion loss, dispertion, and phase velocity characteristics and impedance control capability. Figure 1.6 shows the three coplanar waveguide strips in GSG-configuration (ground-signal-ground), the electrical probing pads, and the open areas that are necessary for micromachining of the fabricated ICs.

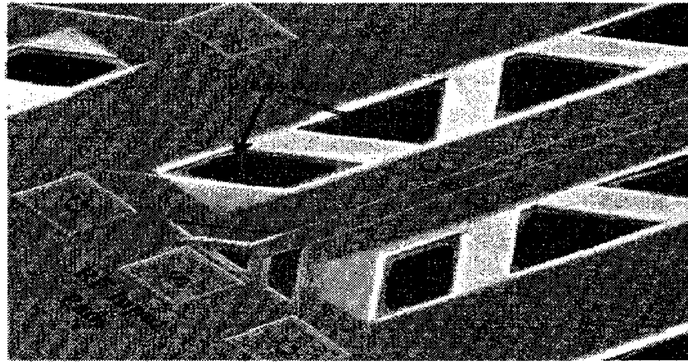

Fig. 1.6 Micromachined GSG coplanar waveguide with RF input pads [20].

1.1.7 Micromachined Antenna

The antenna is an important component in wireless systems that make the connection between the electronics and the outside world. As the frequency of application increases the size of the antenna gets smaller and this poses several manufacturing issues, some of which could be overcome with the use of micromachining techniques. Micromachining techniques offer tremendous potential for fabrication of these small antennas with sub micrometer fabrication tolerance and lower costs through the batch fabrication. As another benefit, using the micromachining techniques, it is possible to fabricate antennas with reconfigurable structures and dimensions. Antennas capable of changing their characteristics are called reconfigurable antennas which are broadly used in satellite broadcast systems.

As explained above, silicon micromachining is a key factor for the vast progress of RF MEMS components, which refers to the fashioning of microscopic mechanical parts out

of the silicon substrates. The following section describes some typical micromachining and MEMS fabrication technologies used in RF MEMS and especially in our work.

1.2 MEMS Fabrication Technologies

Although traditionally silicon is the main material in MEMS technology, in recent years, other materials have been incorporated into MEMS such as metals and their alloys, ceramics, and polymers. For example thick film metal layers are required as the structural parts for RF MEMS components operating at GHz frequency range. The material properties of polymers and ceramics, such as their superior elasticity, yield strength, and stability can be used in the fabrication of both structural and functional parts of MEMS components. As a result the fabrication technologies developed for MEMS should be compatible with a broad class of materials.

Two major MEMS fabrication technologies are bulk micromachining and surface micromachining. In bulk micromachining structures are etched into silicon substrate and in the surface micromachining the micromechanical layers are formed from layers and films deposited on the surface of the substrate. Wafer bonding and LIGA are the other technologies which can be used in the fabrication of 3D microstructures.

1.2.1 Bulk Micromachining

Bulk micromachining is the most mature and the first developed technology which comprises the selective removal and etching of the substrate to form the device membranes. According to the phase of etchants (liquid or vapor), bulk micromachining can be classified as wet or dry etching techniques. Wet etching in most case is done from the back side while the dry etching is used to remove parts of the substrate from the front side.

Wet etching occurs by dipping the substrate into an etching bath containing wet etchants such as tetramethylammonium hydroxide (TMAH), potassium hydroxide (KOH), or ethylenediamine pyrocatechol (EDP) solutions. Wet etching could be isotropic or anisotropic depending on the type of the substrate and etchant materials used. In order to fabricate the desired microstructures using this technique an etch stop region, where the etching speed slows down, should be created. The selective etching can be achieved by

using dopants (doping selective etching) or electrochemically by using a bias voltage (bias dependent etching).

Dry etching utilizes the chemical or physical interaction between the atoms inside the substrate crystal and the ions inside the gaseous etchant. The most common dry etching techniques are the plasma etching and reactive ion etching (RIE), where the external energy in the form of RF power derives chemical reactions in low-pressure reaction chambers. A variety of chlorofluorocarbon gases, sulfur hexafluoride, and oxygen are commonly used for these techniques. Besides plasma and RIE, non-plasma isotropic dry etching is also possible using xenon difluoride which provides a very good selectivity between silicon and aluminum, silicon dioxide, silicon nitride, and photoresist [21]. Figure 1.7 presents the different bulk micromachining technologies.

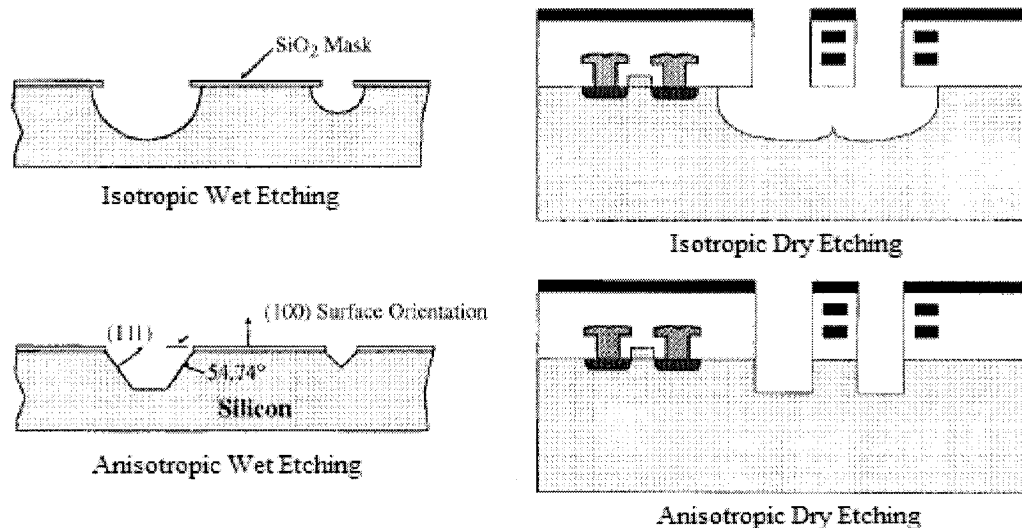

Fig. 1.7 Bulk micromachining techniques [21].

1.2.2 Surface Micromachining

Surface micromachining uses thin films of structural layers on top of the substrate in the fabrication process of microstructures. First a sacrificial layer is deposited on the substrate and then it is followed by the deposition of structural layers. The mechanical structures will be released by eventually removing the sacrificial layers at the end of the process. Figure 1.8 shows the typical processing steps of the surface micromachining. The advantage of the surface micromachining to the bulk micromachining technique is

the smaller size of the devices and its compatibility with standard IC technologies since they are also using the silicon substrate. The materials used in surface micromachining for both the structural and sacrificial layers should have particular characteristics, for example the structural layers must have satisfactory mechanical properties such as, high yield and fracture stress, Young's modulus, and Poisson's ratio. The common IC materials used in surface micromachining are: polysilicon and silicon dioxide, low pressure chemical vapor deposited (LPCVD) polysilicon as the structural layer and the LPCVD deposited oxide as the sacrificial layer. The oxide could be easily dissolved in HF solutions without affecting the polysilicon structural layers.

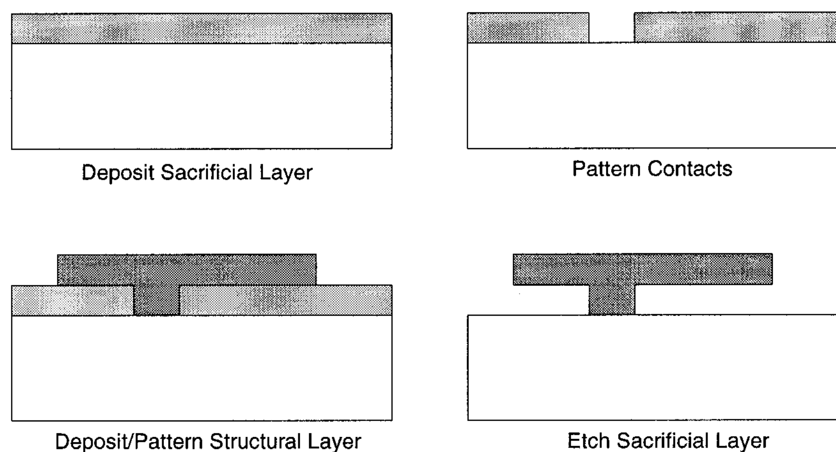

Fig. 1.8 Surface micromachining process steps

Silicon microstructures fabricated using the surface micromachining are called planar or 2D structures because the third dimension, thickness of the structural layers, are fixed for a specific fabrication process. Some other techniques have been applied in extending the capability of surface micromachining in developing 3D structures using the Flip-Chip bonding [22], wafer bonding [23], and LIGA process.

1.2.3 Wafer Bonding

The wafer bonding technique involves the separate fabrication of the various components of a complex system through the standard surface micromachining and then assembling them in a 3D MEMS structure. Wafer bonding is an important step in

micromachining fabrication process. It refers to the mechanical attachment of two or more wafers to each other. Three major bonding techniques are Anodic bonding, Low temperature bonding, and Silicon fusion bonding (SFB) [25]. Anodic or field-assisted thermal bonding is established between a silicon conductive substrate and a sodium rich glass substrate. For the anodic bonding, a cathode and an anode are attached to the glass and silicon wafer respectively. The applied voltage ranges from 200V to 1000V. At the same time, the anode is put on a heater providing the bounding temperature around 180 to 500°C (Figure 1.9). Oxygen ions migrate form the glass substrate to the silicon resulting in the formation of a silicon dioxide layer between two wafers and a strong chemical bond.

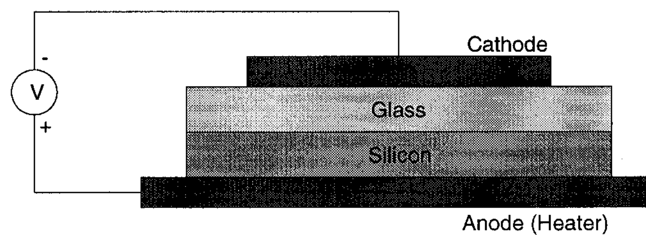

Fig. 1.9 Anodic bonding

The low temperature bonding requires an intermediate thin layer, which can be metal, polymer, solders, or glass, to fulfill the bonding between the wafers. The wafers are placed into contact under pressure and heated to create the bond. The intermediate layer helps to decrease the temperature at which the bonding takes place. Generally bonds created with the low temperature technique are not as strong as the ones achieved by the Anodic method.

Fusion or direct bonding is used for silicon-silicon bonding and it is based on using very high temperature. The fusion bonding usually follows three steps: surface preparation, contacting, and thermal annealing. The surface preparation step involves cleaning the surfaces of the two wafers to form a hydrate surface after achieving the necessary flatness the wafers are aligned and contacted by gently pressing the two wafers at the surface central point. The surface attraction of the two hydrated surfaces then brings the intimate contact over the entire wafer surfaces. The final step is to anneal the

bonding in a temperature around 1200°C. This annealing process increases the bond strength.

1.2.4 LIGA Process

The last process in MEMS fabrication is LIGA. The LIGA process is a process which has been developed to fabricate thick and three dimensional microstructures with high aspect ratios (height-to-width) because of the advanced X-ray lithography. Various materials can be incorporated into the LIGA process, allowing electric, magnetic, piezoelectric and other properties in sensors and actuators, which are not possible to make with the silicon-based processes. A schematic diagram of the LIGA process is shown in figure 1.10. A special kind of photolithography using X-rays is used to produce patters in a very thick layer of photoresist which is sensitive to X-ray. This layer is then developed and the pattern is electroplated with a metal layer, the produced metal layer can be the final structure, however it is common to produce a metal mould which can be filled with a suitable material, such as plastic, to produce the finished product in that material.

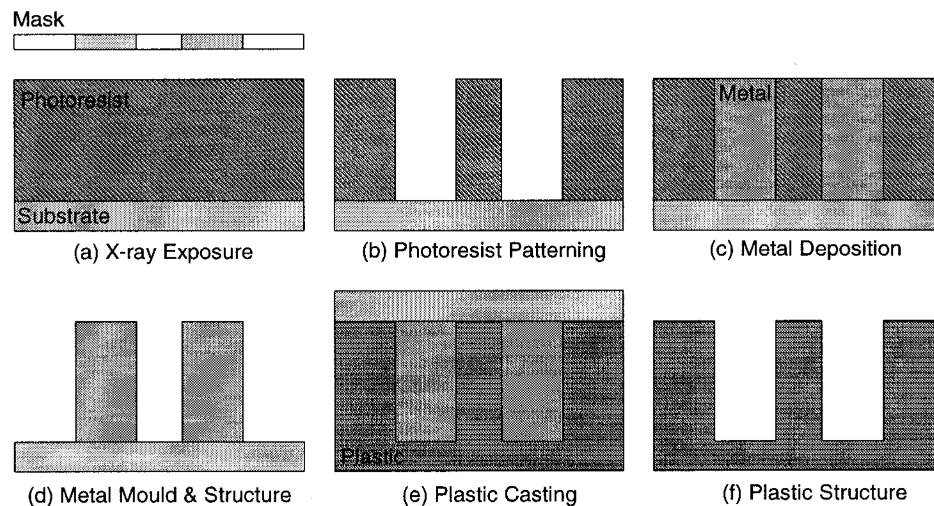

Fig. 1.10 The LIGA process

1.2.5 PolyMUMPs and CMOS Foundry Services

Two commercially available processes will be highlighted in this section, which have been used to fabricate the RF MEMS devices presented in this work. One is the Polysilicon Multi User MEMS Process (PolyMUMPs) [25] and the other is a standard 0.35μm Complementary Metal-Oxide-Semiconductor (CMOS) [26] process. Both processes can be used to create complex MEMS microstructures.

The PolyMUMPs process is a three layer polysilicon surface micromachining process derived from work performed at the Berkeley Sensors and Actuators center in the early 90's. This process has the general features of a standard surface micromachining process: (1) Polysilicon is used as the structural material, (2) Deposited silicon dioxide is used as the sacrificial layer, (3) Silicon nitride is used as an electrical isolation between the polysilicon and the substrate, (4) Metal (usually gold) is the top layer of the device and can be used as a conductive layer. The layer stack of the PolyMUMPs process is shown in figure 1.11.

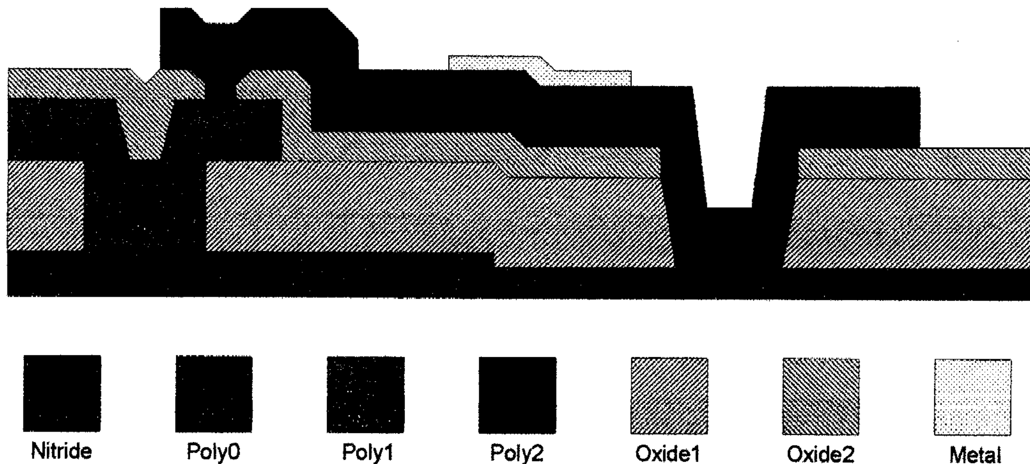

Fig. 1.11 Cross-sectional view of PolyMUMPs process

This process offers two structural layers of polysilicon (Poly1 and Poly2) and two sacrificial layers of silicon dioxide (Oxide1 and Oxide2). The Poly0 layer is used as an electrical ground plane rather than a structural layer. Patterning the layers is done via photolithography and reactive ion etching (RIE). The oxide layers are considered as the sacrificial layers because they do not appear in the final structure. When the chips come

back from the foundry, the oxide is etched, freeing the polysilicon layers and allowing them to move. By connecting Poly1 to Poly2 (or Poly2 to substrate) a variety of hinges can be constructed that allows suspended plates of polysilicon to move out of the plane of the wafer. The required etchant is liquid 49% hydrofluoric acid (HF) which has a very high selectivity between silicon dioxide and polysilicon. Proper drying of the chip after release is important to reduce the possibility of the polysilicon structures sticking to each other and the substrate which is called stiction problem. One of the drying methods is the supercritical carbon dioxide drying [27]. In order to make the process as general as possible, all the layers have a predefined thickness and functionality. Although the standardization of the fabrication process reduces the fabrication cost and allows more and more designers to submit their designs but, it forces the designers to follow the definitions and the design rules which impose limitations to the available physical dimensions. Table 1.1 presents the main limitations and a brief description of each layer's functionality.

Material Layer	Thickness	Lithography Level Name	Purpose
Silicon Nitride	0.6μm		Insulator
Poly0	0.5μm	Poly0 and Hole0	Conductive Layer
Oxide1	2.0μm	Dimple	Bushing for Poly1
Oxide1	2.0μm	Anchor1	Fix Poly1 on Nitride or Poly0
Poly1	2.0μm	Poly1 and Hole1	1st Structural Layer
Oxide2	0.75μm	Poly1-Poly2-Via	Poly1-Poly2 Connection
Oxide2	0.75μm	Anchor2	Fix Poly2
Poly2	1.5μm	Poly2 and Hole2	2nd Structural Layer
Metal	0.5μm	Metal and Metal Hole	Conductive Media

Table 1.1 PolyMUMPs layers and their functionalities

Although the PolyMUMPs process has much to offer, it does not currently support on-chip integrated electronics. Thus, a standard 0.35μm CMOS process is presented here which can be used to create MEMS structures with on-chip sensing electronics. This process is a four metal and dual poly process consisting of totally 19 masks and 23 fabrication steps. The available layer stack for this process is shown in figure 1.12. In this

process MOSFETs are fabricated along with MEMS microstructures. All lithography and thin film patterning was performed during this process.

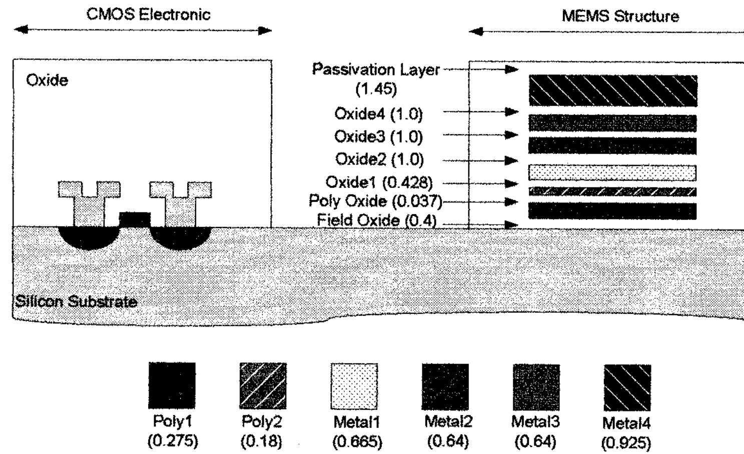

Fig. 1.12 TSMC CMOS 0.35μm layer stack and the thickness of layers in (μm)

When the chips come back from the CMOS foundry, they require a single unmasked etch. In this case, the primary structural materials are the polysilicon and metal layers and the silicon substrate is the sacrificial material. "Vias" are the holes patterned in the oxide layers by which layers of polysilicon and metal are connected to the substrate or each other. Etch window is created by patterning successive vias on top of each other, thereby leaving the silicon substrate exposed. This exposed silicon can then be etched to undercut and release the microstructures and does not require a mask since the etching areas are already patterned at the foundry. The only parameters are the choice of silicon etchant, etch temperature, and etching time. Ideally, the microstructures can be released using any wet silicon etchant such as TMAH or KOH. However, because the aluminum metal layers can not withstand these wet etchants, the metal structural layers should be covered with a thin silicon dioxide layer by a proper layout design. Another option is to use dry-phase etchants, such as XeF_2. This isotropic gas-phase etchant offers high selectivity towards silicon dioxide and aluminum, and it eliminates any liquid bubbles that can damage the microstructures and result in stiction problems.

1.3 RF MEMS Integration

MEMS technology has been extensively used for RF and wireless applications due to its immense commercial and industrial potentials. Although the RF MEMS components can be used to implement high density SOC receivers and transmitters, still there are lots of challenges in MEMS commercialization including integration, reliability, packaging, and etc. which are presently the topic of ongoing research. One of the most important challenges in commercialization of RF MEMS technology is the integration of RF MEMS components with the standard IC components into the RF modules. Two different approaches can be used in integration; monolithic and hybrid integrations.

In hybrid integration each chip is fabricated using the appropriate fabrication process and then wire-bonding and flip-chip bonding techniques are used to combine two different chips into the final module. Flip-chip technology is defined as mounting the chip to another substrate or bigger chip with any kind of interconnect materials and methods, for example; solder bumps, wire interconnects, conductive polymers, and pressure contacts as long as the chip surface or active area is facing the target substrate [28]. Flip-chip technology is attractive to the MEMS industry because of its ability to integrate a system on chip through packaging a number of different dies on a single substrate. This technique can be used to produce highly advanced microstructures for RF, microwave, and optical applications.

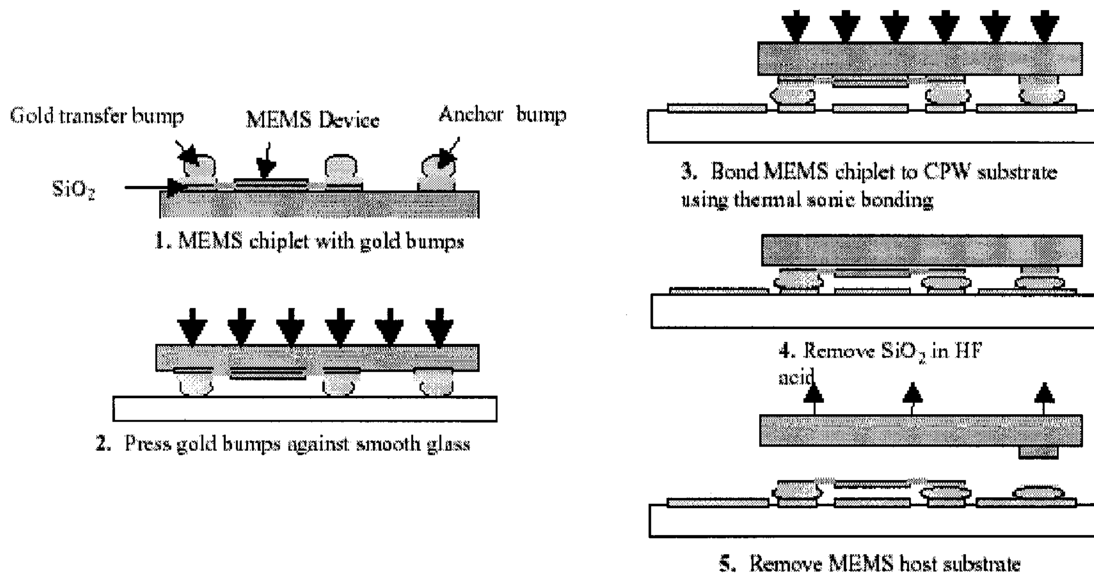

Fig. 1.13 Flip-chip transfer process steps [29]

Figure 1.13 illustrates the flip-chip process steps. The process starts with placing the gold transfer bumps on top of the transfer pads and anchor pads in an unreleased MEMS die. The transfer pads are only connected to the host substrate with the sacrificial silicon dioxide layer and this way the transfer pads and thus the MEMS structure will be disconnected from the host substrate after the HF release. Before putting the target and host substrates on top of each other, the gold bumps are pressed against a smooth glass substrate to flatten the bumps. The host substrate is anchored at the anchor bump, this anchor bump prevents the substrate from contacting the MEMS device and after the HF release it can be removed by using clamps to break it without any damage to the device.

Monolithic integration involves the fabrication of both MEMS and IC circuits on the same chip. This integration method results in higher performance and reduced packaging costs, but due to the limitations in fabrication technology sometimes monolithic solution is impossible and hybrid integration, which makes it possible to fabricate the MEMS independent of the IC, is the only possible option. While RF MEMS inductors are already manufactured in CMOS-compatible lines, for other RF MEMS components like RF switches or tunable capacitors, with a higher number of masks, still dedicated fabrication steps are required to accomplish the monolithic integration. In section 3.7 we will discuss the monolithic integration approach through standard CMOS process. A novel MEMS-CMOS parallel-plate variable capacitor is designed and fabricated. The monolithic integration of this device has been realized using the standard TSMC CMOS 0.35μm technology.

1.4 Modeling Methodologies

Simulation of micro electro mechanical systems requires the interaction of different physics environments due to the mixed mixed-domain nature of the device. Moreover the current system on chip MEMS design requires the combination of the analog and digital signal processing circuitry besides the nonelectrical components and to verify the whole system performance at once, the microelectromechanical models should be integrated in a mixed-domain simulator, for this reason, appropriate system level modeling and simulation techniques are required.

Although, Finite element method (FEM) has been successfully applied to perform coupled-field analysis of MEMS devices, FEM is only suited to handle the individual components and not the system level simulation due to the large number of partial differential equations required to describe the entire microsystem. Simulation of the whole microsystem can be divided to two parts, mixed-signal analog and digital circuit simulation using the conventional IC CAD tools and MEMS device simulation employing differential and integral equation methods. As a result the coupled circuit-device simulation is inevitable in the performance evaluation of microsystems.

MEMS components can be integrated in the simulation phase of mixed-technology systems using two different approaches. The first approach is through the coupling of different circuit and device simulators where the results of the FEM analysis of MEMS component is used as an input for the circuit simultor and vice-versa, multiple passes between two simulators is necessary to achieve an equilibrium state. Integration of circuit and device simulators to design an RF VCO based on MEMS capacitor is presented in [30]. The second approach which will be discussed in more detail is based on developing macromodels for the MEMS components. The macromodel itself can be generated in two different ways; the first method is to extract an equivalent lumped-element electrical network of MEMS device. Second approach, is to generate behavioral macromodels using the mixed-signal hardware description language, VHDL-AMS. The generated behavioral models can be used for the simulation of entire system in both VHDL-AMS simulators or in circuit simulators such as SPICE.

VHDL-AMS, an IEEE standard hardware description language for analog and mixed-signal applications, provides a behavioral modeling environment. This language supports the modeling at various abstraction levels in electrical and nonelectrical energy domains [31]. Modeling of the conventional analog and digital electrical part of the system in VHDL-AMS is straightforward, but still there are challenges in behavioral modeling of the nonelectrical part. Up to date several methods have been applied in computer aided generation of behavioral models for MEMS components such as, reduced order modeling [32], equivalent lumped element networks [33, 34], and discretization of system equations [35]. In section 2.2.10, the reduced order modeling and equivalent electrical

networks will be presented in system level simulation and modeling of RF MEMS components.

1.5 Thesis Outline

As mentioned in section 1.1 RF MEMS devices with their tiny size, lower power consumption, lower cost through batch fabrication, and their superior performance at RF frequency range, have been extensively used in design and implementation of system on chip RF front-ends. A huge number of RF MEMS components have been designed and fabricated under lab and industry environments. Although RF MEMS devices have lots of very competitive advantages over the traditional semiconductor and off-chip counterparts, there also exist some challenges in the design and fabrication of these components, such as integration, packaging, stability, and acceptable performance at RF frequencies.

This project is focused on modeling, design, and fabrication of band-pass filters for RF applications using MEMS components. The first class of filters is based on micromechanical resonators covering a frequency range from 1MHz up to 10MHz and the second class of filters is implemented using RF MEMS tunable capacitors. The devices will be fabricated by a standard surface micromachining process, PolyMUMPs, and also a standard CMOS 0.35μm, followed by some post-processing steps. Chapter 2 will focus on the theory, modeling, and simulation of MEMS band-pass filters comprising the micromechanical resonators and lumped element tunable MEMS variable capacitor. Behavioral modeling and generating macro models for RF MEMS components that will be used in system level simulation of the final filter will be introduced in more detail in this chapter. In chapter 3, design, fabrication, and post-processing of the filters will be presented. In chapter 4, we will report experimental results and observations and conclusion besides future works are given in chapter 5.

Chapter 2
Theory, Modeling, and Simulation of MEMS Band-Pass Filters

In this chapter first we will discus a brief theory of the analog band-pass filters, filter approximations, and the main frequency characteristics of the filter will be introduced. Then the theory of micromechanical filters will be presented and we will study several classes of micromechanical resonators such as, cantilever beam, clamped-clamped beam, and disk resonators. For the micromechanical filters which are based on micromechanical resonators an important issue is to find an equivalent electrical model which can be used in electrical domain simulators for filter simulation. These electrical equivalent models will be constructed using the electromechanical analogy which exists between the electrical and mechanical domains.

As explained in section 1.4, the simulation of micro electro mechanical systems involves the coupling between several physical domains. Although FEM analysis using coupled-field simulators such as ANSYS can be used for simulation purposes, but for the whole system where the MEMS component is located among other analog and digital (mixed-signal) circuits, FEM analysis can not be applied and in this case we need a macro-model of the MEMS component which can be used in a mixed-signal circuit simulator. This is a topic of ongoing research and it will be discussed in more detail in this chapter. Finally the simulation results using FEM analysis with ANSYS, equivalent electrical circuit simulation using SPICE, and the simulation results using the behavioral macro-models with mixed-signal AdvanceMS simulator will be presented and compared with each other.

2.1 Theory of Band-Pass Filters

A filter is a two-port network as shown in figure 2.1 used to control the frequency response at a certain point in a microwave system by providing transmission at frequencies within the pass-band of the filter. Typical frequency responses include low-pass, high-pass, band-pass, and band-reject characteristics. Filters are widely used in microwave communication, radar, or test and measurement systems [36].

2.1.1 Preliminary Definitions

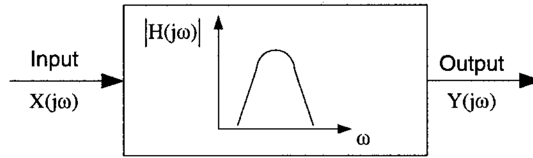

Fig. 2.1 Filter as a two-port network

For a single input, single output filter as represented in figure 2.1, where the filter is composed of linear, lumped elements, then the input and output are related by a linear, ordinary, differential equation. In frequency domain this relation can be shown as

$$Y(j\omega) = H(j\omega) * X(j\omega) \tag{2.1}$$

The network or transfer function is the ratio of the transformed output and input variables. The transfer function is a complex quantity and it can be written in the form

$$H(j\omega) = |H(j\omega)| e^{j\phi(\omega)} \tag{2.2}$$

where $|H(j\omega)|$ is the amplitude or magnitude response and $\phi(\omega)$ is the phase response. The amplitude and phase responses can be used in filter classification. In frequency selection stages the amplitude response is of greater importance than the phase response and based on the location of the pass- and stop-band frequencies they can be classified as shown in figure 2.2. This figure shows the amplitude response for ideal filters where we have assumed a linear phase response, zero loss in the pass-band, and infinite loss in the stop-band. The amplitude $|H(j\omega)|$ can be converted to decibels (dB) as

$$H_{dB} = 20\log_{10}|H(j\omega)| \tag{2.3}$$

then for the pass-band, $H_{dB} = 0dB$ and for the stop-band $H_{dB} = -\infty dB$.

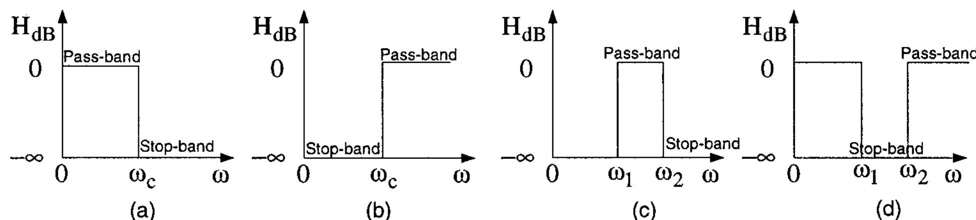

Fig. 2.2 Amplitude response, (a) low-pass, (b) high-pass, (c) band-pass, (d) band-stop

Figure 2.3 shows the amplitude characteristic of a band-pass filter in more detail. The most important characteristic of a filter is the insertion loss. This is the ratio of the signal taken at the output port to that supplied to the input port of the filter. The design goal is to minimize this quantity within its pass-band. The pass-band is defined as the band in which the attenuation of the filter amplitude response is small. The pass-band characteristics of a filter are generally expressed as its quality factor (Q-factor). The quality factor is a measure of the energy stored in the system to the energy dissipated per cycle. In terms of the frequency band this can be expressed as

$$Q = \frac{\omega_0}{\Delta\omega} \tag{2.4}$$

where ω_0 is the center frequency midway between 3dB attenuation frequencies and $\Delta\omega = \omega_2 - \omega_1$ is the filter 3dB bandwidth (figure 2.3). There are few other quantities often encountered in filter design. The region outside the 40dB points is the stop-band and stop-band rejection is the signal transmitted through the system at frequencies beyond the pass-band expressed in decibels, often relative to the minimum insertion loss.

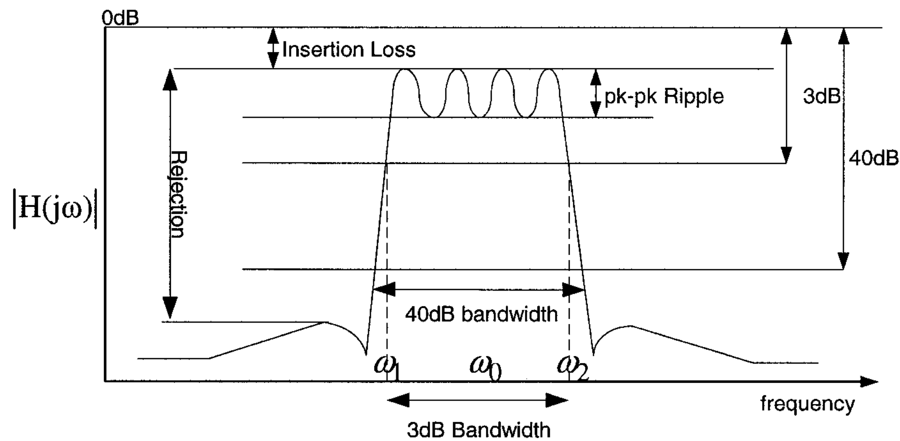

Fig. 2.3 The main characteristics for a band-pass filter

2.1.2 Filter Design Methods

There are two different methods in filter design; image parameter method and insertion loss method. In order to simplify the design procedure we can start with a low-pass prototype filter that is normalized in terms of impedance and frequency and then

impedance and frequency transformations are applied to convert the prototype filter to the desired one (band-pass). Both the methods mentioned above provide lumped-element circuits for filter synthesis. At microwave frequencies such designs usually must be modified to use distributed elements consisting of transmission line sections. The Richard's transformation and Kuroda identities provide this step [36].

2.1.3 Image Parameter Method

The image parameter method of filter design uses a series of cascaded two-port networks to implement a desired pass-band and stop-band characteristic. Tow important types of two-port networks are T and π circuits, which can be made in symmetric form and by cascading them, we can implement the desired filter. In terms of image parameter method, three different filter configurations are possible; Constant-k Filter Sections, m-derived Filter Sections, and Composite Filters.

Low-pass and high-pass constant-k filter sections are implemented in T forms as shown in figure 2.4. There are only two parameters to choose (L and C), which are determined by ω_c, the cutoff frequency, and R_o, the image impedance at zero frequency.

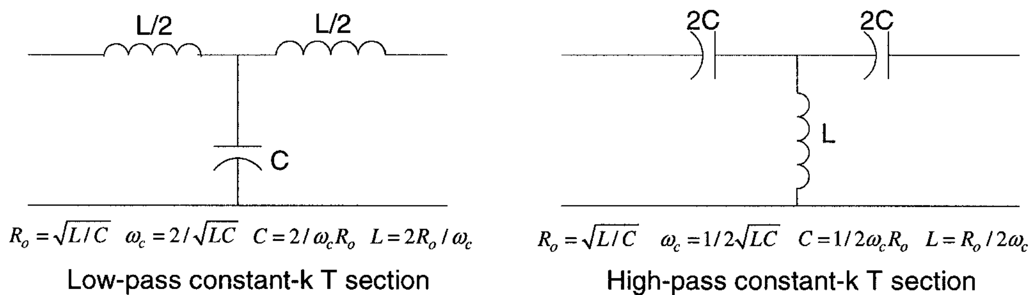

Fig. 2.4 Constant-k (T) filter sections

The above designs are valid only when the filter section is terminated in its image impedance at both ports. This is a major weakness of the design, because the image impedance is a function of frequency, which is not likely to match a given source or load impedance. m-derived sections can be used to remedy this disadvantage.

The m-derived filter section is a modification of the constant-k filter section to overcome the slow attenuation rate past cutoff frequency and the non-constant image

impedance. Figure 2.5 shows the low-pass and high-pass m-derived T sections. L and C can be defined using the same equation for the constant-k sections shown in figure 2.4.

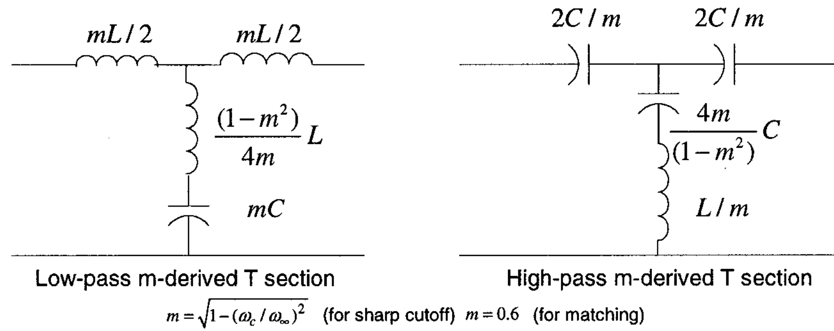

Fig. 2.5 High-pass and Low-pass m-derived (T) sections

One problem with the m-derived section is that its attenuation decreases for $\omega > \omega_\infty$, where ω_∞ is the resonant frequency of the series LC resonator. Since it is often desirable to have infinite attenuation as $\omega \to \infty$, the m-derived section can be cascaded with a constant-k section to give the composite attenuation response. Figure 2.6 shows the schematic of a composite filter.

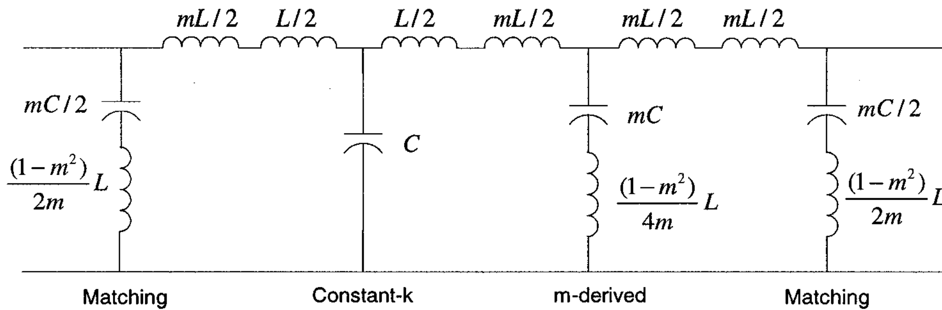

Fig. 2.6 Low-pass composite filter

The image parameter method is relatively simple but has the disadvantage that an arbitrary frequency response can not be incorporated into the design. This is in contrast to the insertion loss method, which is the subject of the following section.

2.1.4 Insertion Loss Method

The insertion loss method allows a high degree of control over the pass-band and stop-band amplitude and phase characteristics of the filter with a systematic way to synthesize a desired response. In the insertion loss method a filter response is defined by its insertion loss

$$P_{LR} = \frac{Available_Power}{Power_Delivered_to_Load} \quad 2.5$$

and the insertion loss in dB is

$$IL = 10 \log P_{LR} \quad 2.6$$

Some practical filter responses are the maximally flat (Butterworth), equal ripple (Chebyshev), and elliptic function. The maximally flat or Butterworth response provides the flattest possible pass-band response. For a low-pass Butterworth filter the power loss ratio is

$$P_{LR} = 1 + k^2 (\frac{\omega}{\omega_c})^{2N} \quad 2.7$$

N is the order of the filter (number of reactive elements) and ω_c is the cutoff frequency. Band-pass extends from $\omega = 0$ to $\omega = \omega_c$ and the power loss ration at the band edge is $1 + k^2$. For a -3 dB insertion loss at the band edge, k=1.

For the equal ripple response the insertion loss of an N-order low-pass filter is specified as

$$P_{LR} = 1 + k^2 T_N{}^2 (\frac{\omega}{\omega_c}) \quad 2.8$$

The pass-band response will have ripples of amplitude $1 + k^2$ and a sharper cutoff will result at the band edge compared to the Butterworth response. The attenuation in the stop band for the maximally flat and equal ripple responses increases monotonically. For the Elliptic response there is specified minimum stop band attenuation as well as a maximum attenuation in the pass-band, such as the equal ripple response. Figure 2.7 compares the amplitude response of the Butterworth and Chebyshev filters. Other general filter specifications can be obtained, but the above cases are the most common ones.

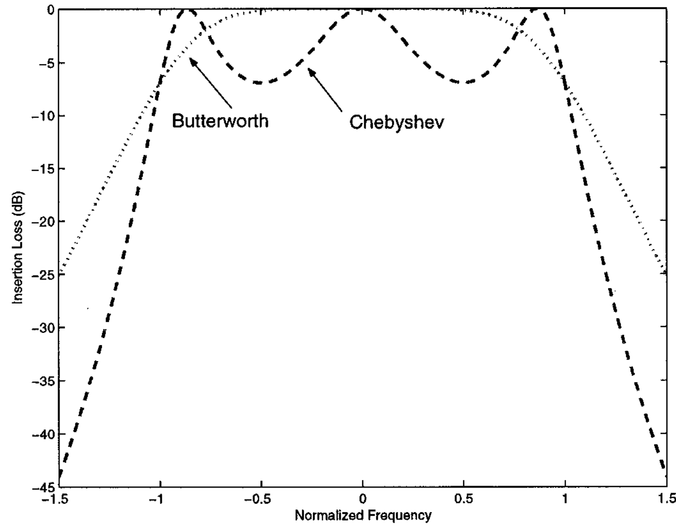

Fig. 2.7 Butterworth and Chebyshev filter approximations (N=3, k=1)

The ladder circuits shown in figure 2.8 can be used in low-pass prototype filter design. For a normalized low-pass design where the source impedance is 1 Ω and the cutoff frequency is $\omega_c = 1$, the element values, i.e. $g_1, g_2, \dots$, for the ladder circuits are tabulated in filter cookbooks [36].

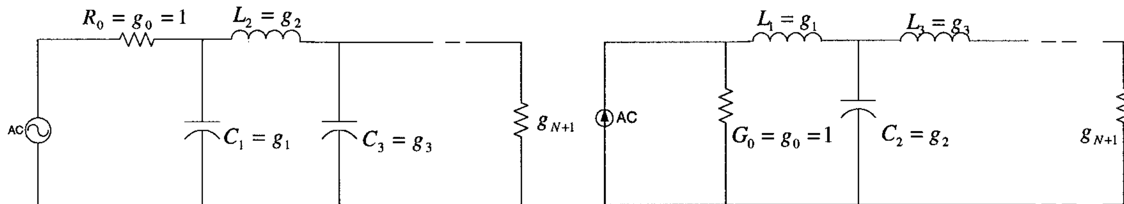

Figure 2.8 Ladder circuits for low-pass filter prototypes

2.1.5 Filter Transformations

The low-pass filter prototypes can be scaled in terms of impedance and frequency and converted to give high-pass, band-pass or band-stop characteristics. Impedance scaling involves the multiplication of the impedances for the prototype filter by R_0 which is the source impedance of the real filter. To change the cutoff frequency from unity to ω_c the frequency should be scaled by a factor of $1/\omega_c$. When both impedance and frequency scaling are performed, we have the new filter component values given by

$$L' = \frac{R_0 L}{\omega_c}, \quad C' = \frac{C}{R_0 \omega_c}, \quad R_L' = R_o R_L, \quad R_S' = R_0 \qquad 2.9$$

Low-pass filter can also be transformed to a band-pass filter using the band-pass transformation. If ω_1 and ω_2 represent the edges of the pass band, then a band-pass filter can be obtained using the following frequency substitution [36]

$$\omega \leftarrow \frac{\omega_0}{\omega_2 - \omega_1}\left(\frac{\omega}{\omega_0} - \frac{\omega_0}{\omega}\right) \qquad 2.10$$

Using 2.10 the series inductor transforms to a series LC circuit with element values

$$L'' = \frac{L'}{\Delta \omega_0} \text{ and } C'' = \frac{\Delta}{\omega_0 L'} \text{ where } \Delta = \frac{\omega_2 - \omega_1}{\omega_0} \qquad 2.11$$

and the shunt capacitor is transformed as a shunt LC circuit with element values

$$L'' = \frac{\Delta}{\omega_0 C'} \text{ and } C'' = \frac{C'}{\Delta \omega_0} \qquad 2.12$$

In these equations L and R are the component values for the original prototype and L'' and C'' are the new filter component values.

2.2 Microelectromechanical Band-Pass Filters

The term electromechanical filter covers many types of filters such as, crystal filters, ceramic filters, and surface acoustic wave (SAW) filters, so we must further define what we mean by the word microelectromechanical filter. A microelectromechanical filter is composed of mechanically coupled resonators. This differentiates a mechanical filter from quartz-crystal filters or ceramic filters which are composed of electrically coupled resonators. A microelectromechanical filter is differentiated from a SAW filter by the fact that signals in a SAW filter are propagated in only one direction while, signals in a microelectromechanical filter are allowed to propagate back and forth between the output and input ports [8].

The term electromechanical comes from the transformation within the filter. These filters use two electromechanical transducers, one at the input port and another at the output side and a form of mechanical transmission line connecting them. The electrical energy is converted into a form of mechanical energy such as vibration at the first electromechanical transducer. This mechanical energy is propagated using a mechanical

transmission line where the filtering takes place and then the remaining signals are transformed back into the original electrical form at the output transducer.

High-Q microelectromechanical filters using mechanical resonators are widely used in many communication systems in the HF range. As the frequency is increased the size of these resonators become smaller, almost impossible to be fabricated using the conventional methods and here is the area where the MEMS technology can be used. MEMS resonators with proper packaging techniques can be used in developing filters for frequencies up to 100 megahertz with high Q factors of 1000s [37]. In next sections we will discuss the micromechanical resonators such as, beam and disk resonators and then using the electromechanical analogies the equivalent electrical models will be developed.

2.2.1 MEMS Resonators

Resonators are the basic building blocks in filter and oscillator design. Figure 2.9 shows the simplest types of resonators which are the parallel and series RLC resonators. These resonators are made of lumped element resistors, capacitors, and inductors. Other types of resonators can be implemented using distributed elements such as transmission lines, waveguides, and dielectric cavities.

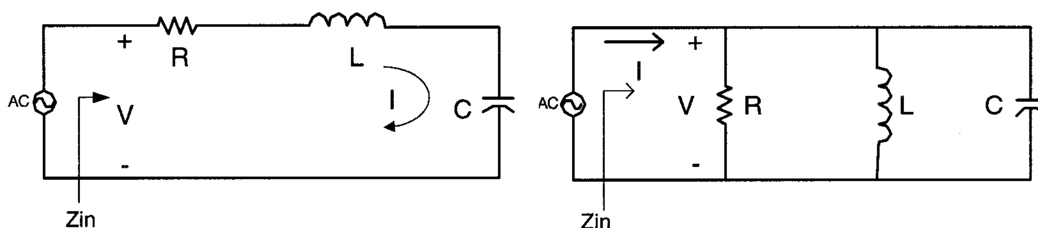

Fig. 2.9 Series and parallel RLC resonators

An alternative approach is to use MEMS resonators and they will represent the same electrical behavior as the ones shown in figure 2.9, based on the analogy in the mathematical description that exists between electrical and mechanical phenomena. These analogies are a result of the similarities of the equations governing the behavior of electrical and mechanical systems. For example, Newton's second law of motion relating

the force F and velocity u for a rigid mass m, $F = mdu/dt = md^2x/dt^2$ is mathematically analogous to the constitutive equation of an electric inductor, $v = Ldi/dt = Ld^2q/dt^2$. In this analogy, the force F plays the same role as the voltage v, the velocity u as the current i, and the displacement x as the charge q. The mass m in mechanical systems corresponds to the inductance L in electrical circuits. This example illustrates the direct analogy, summarized in Table 2.1 [33].

Mechanical Parameter	Electrical Parameter
Mass, M	Inductance, L
Damping, D	Resistance, R
Compliance, 1/K	Capacitance, C
Velocity, u	Current, i
Displacement, x	Charge, q
Momentum, p	Magnetic flux linkage, λ
Force, F	Voltage, v

Table 2.1 Direct electromechanical analogy

As explained in section 1.1.4 recently several MEMS resonators have been fabricated for RF filters and oscillators. A contour mode disk resonator is presented in [12] with a measured frequency and Q of 156 MHz and 9400, respectively the highest to date for electro statically driven micromechanical resonators. The main advantage of micromechanical resonators is their high Q value approaching more than 10,000 and the main drawback is their relatively low frequency range and the research in this area is focused on increasing the frequency range of this MEMS resonators.

2.2.2 Theoretical Concepts and Modeling of MEMS Resonators

In this section the basic principles of laterally vibrating beam resonators and disk resonators are discussed and then the modal resonance frequency of the resonators versus the geometry and material properties is calculated. Mechanical models and their equivalent electrical circuits will be introduced and finally based on these equivalent circuits an electrical model will be created for the MEMS resonators in this work.

Figure 2.10 presents the perspective view of a clamped-clamped beam resonator, along with appropriate bias, excitation, and sensing circuitry. As shown, the resonator consists of a beam clamped at ends, a drive electrode which serves as a capacitive transducer to induce resonator vibration in a direction perpendicular to the substrate, and a sense electrode. If the frequency of the input voltage is within the bandwidth of micromechanical resonator then the input voltage will result in excitation of the resonator and the beam starts to vibrate with its natural resonant frequency. Vibration of the resonator beam creates a time-varying capacitor between the conductive resonator beam and sense electrode, which then sources an output current. The output current is then directed to the output termination resistor and the current is converted to an output voltage.

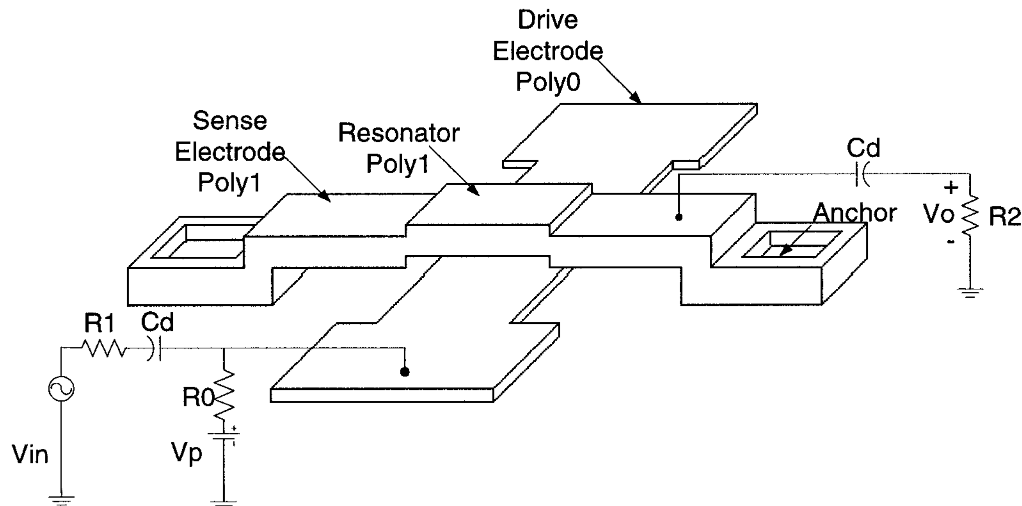

Fig. 2.10 Perspective view of a clamped-clamped beam micromechanical resonator

In effect, this device takes an electrical input signal, converts it to a mechanical signal, processes it in the mechanical domain, then reconverts the resulting signal to an electrical output signal.

In this section, we will discuss the classical method of calculating modal frequencies for the MEMS resonators in absence of electromechanical effects and we will just consider the problem in mechanical domain, later we will include the electromechanical

coupling effects and drive an equation for the final modal resonant frequencies. In using this method we will make these assumptions [8]:

1. The amplitude of vibration is small and the strain-stress characteristics are linear.
2. There are no internal losses for example due to the air damping effect and the vibration takes place in vacuum.

2.2.3 Flexural-Mode Beam Resonator

The starting point for the analysis is a set of linear partial differential equations called wave-equations in the mechanical domain, which is a differential equation to describe the lateral vibration of the resonant beam. This equation is usually second or fourth order in terms of the coordinates (x, θ, etc) and second order in time t. The differential equation is determined in [38] and here we will not go through the driving of this mechanical wave-equation. The mechanical wave-equation, called Euler equation, of a thin flexural-mode beam is

$$\frac{\partial^2 u}{\partial t^2} = (\frac{EI}{\rho A})\frac{\partial^4 u}{\partial x^4} \qquad 2.13$$

where u is the displacement in the y direction as shown in figure 2.11 and I is the bending moment of inertia which for a rectangular beam can be written as [8]

$$I = \frac{wt^3}{12} \qquad 2.14$$

In the equations above E is the elastic modulus, ρ is the material density, w and t are the width and thickness of the rectangular bar as shown in figure 2.11

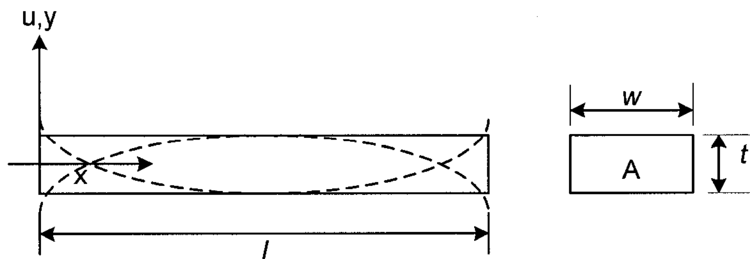

Fig. 2.11 Fundamental flexural-mode beam

Next by substituting $u = u_1 e^{j\omega t}$ into 2.13 we can eliminate the time dependency. Then we can write

$$\frac{\partial^4 u_1}{\partial x^4} = (\omega^2 \frac{\rho A}{EI}) u_1 \qquad 2.15$$

which is a fourth-order differential equation having the solution

$$u_1(x) = A\cosh(kx) + B\sinh(kx) + C\cos(kx) + D\sin(kx) \qquad 2.16$$

The next step is to apply the boundary conditions to the displacement equation 2.16 to eliminate the amplitude constants. For a clamped-clamped beam which is fixed at both ends the boundary conditions are

$$\text{At } x = 0, l \; : \; u_1 = 0 \, , \, \frac{\partial u_1}{\partial x} = 0 \qquad 2.17$$

Substituting the boundary conditions at $x = 0$ in the general solution 2.16 we obtain the relationship between the amplitude constants

$$(u_1)_{x=0} = A + C = 0 \therefore A = -C \qquad 2.18$$

$$\left(\frac{\partial u_1}{\partial x} \right)_{x=0} = k(B + D) = 0 \therefore B = -D \qquad 2.19$$

For $x = l$ we can write the remaining equations in a matrix form

$$\begin{bmatrix} \cosh(kl) - \cos(kl) & \sinh(kl) - \sin(kl) \\ \sinh(kl) + \sin(kl) & \cosh(kl) - \cos(kl) \end{bmatrix} \begin{bmatrix} A \\ B \end{bmatrix} = 0 \qquad 2.20$$

This set of homogenous equations can be solved only if the determinant is equal to zero. By setting the determinant equal to zero, we obtain the frequency equation

$$\cos(kl) = \frac{1}{\cosh(kl)} \qquad 2.21$$

Equation 2.21 should be solved numerically. The first three roots are located at

$$\begin{aligned} k_1 l &= 4.730 \\ k_2 l &= 7.853 \\ k_3 l &= 10.996 \end{aligned} \qquad 2.22$$

Next substituting the solution 2.16 into equation 2.15 we obtain the dispersion relationship

$$k^4 = \frac{\rho A}{EI} \omega^2 \qquad 2.23$$

and the equation for the resonant frequency is

$$f_n = \frac{(k_n l)^2}{2\pi l^2}\sqrt{\frac{EI}{\rho A}} \qquad 2.24$$

Where the value of ($k_n l$) depends on the boundary conditions of the problem. The following Table lists numerical values of $(k_n l)^2$ for typical end conditions for the flexural-mode beam resonator.

Beam Configuration	$(k_1 l)^2$	$(k_2 l)^2$	$(k_3 l)^2$
Simply supported	9.87	39.5	88.9
Cantilever	3.52	22.0	61.7
Free-Free	22.4	61.7	121.0
Clamped-Clamped	22.4	61.7	121.0
Clamped-Hinged	15.4	50.0	104.0
Hinged-Free	0	15.4	50.0

Table 2.2 Roots of the frequency equation for different boundary conditions

Substitution of the roots in 2.22 for the clamped-clamped boundary condition into 2.24 allows us to calculate the resonance frequencies. The ratios of the higher order modes to the fundamental mode, f_n / f_1, are shown in Table 2.3.

Mode	N	$k_n l$	f_n / f_1
Fundamental (f_1)	1	4.730	1.000
1st Harmonic	2	7.853	2.757
2nd Harmonic	3	10.996	5.404
3rd Harmonic	4	14.137	8.932
4th Harmonic	5	17.279	13.344

Table 2.3 Characteristics of Flexural-Mode clamped-clamped beam resonator

Using equation 2.14 for the bending moment of inertia then equation 2.24 can be written as

$$f_n = \frac{(k_n l)^2}{2\pi\sqrt{12}} \sqrt{\frac{E}{\rho}} \frac{t}{l^2} \qquad 2.25$$

Based on equation 2.24 the main design parameters affecting the fundamental modal frequency and also the higher harmonics of the clamped-clamped beam are the beam length (l), thickness (t), and the material properties of the structural layer; Young's modulus (E), and density (ρ). For so called wide beams where $w > 5t$, Young's modulus is replaced by

$$E_{effective} = \frac{E}{(1-\nu^2)} \qquad 2.26$$

where ν denotes the Poisson's ratio [34].

When the spatial wavelength of the vibration is not large compared to the beam thickness, Timoshenko theory is used to find the resonance frequency. This means that effects of rotary inertia and shear deflections should be taken into account [39]. When the effects of shear deformation and rotary inertia are considered, the beam is sometimes called the Timoshenko beam. The rotary inertia is equivalent to an increase in mass and therefore will cause a decrease in natural frequency. Furthermore the effect is more pronounced at higher frequencies and more influential on higher modes. The equation of motion for the lateral vibration of a uniform beam including the shear deformation and rotary inertia effects can be written as [38]

$$EI\frac{\partial^4 u}{\partial x^4} + \rho A\frac{\partial^2 u}{\partial t^2} - \rho I(1+\frac{E}{\kappa G})\frac{\partial^4 u}{\partial x^2 \partial t^2} + \frac{\rho^2 I}{\kappa G}\frac{\partial^4 u}{\partial t^4} = 0 \qquad 2.27$$

where, A is the cross-sectional area, G is the shear modulus, I is the bending moment of inertia, and κ is a shape factor of the cross-section (for a rectangular cross-section $\kappa = 2/3$) [40].

$$G = \frac{E}{2(1+\nu)} \qquad 2.28$$

For a clamped-clamped Timoshenko beam the boundary conditions at the ends of the beam are the same as the boundary conditions for a simple clamped-clamped beam, listed in 2.17. Exact solution for the vibration of Timoshenko beams exist just for a very

restricted number of simple cases. For the fundamental transverse mode the frequency equation can be written as [41, 10]

$$\tan\frac{\beta}{2}+\frac{\beta}{\alpha}\left(\frac{\alpha^2+p^2(\kappa G/E)}{\beta^2-p^2(\kappa G/E)}\right)\tanh\frac{\alpha}{2}=0 \tag{2.29}$$

where

$$p^2=\omega^2 l^2/c_o^2 \tag{2.30}$$

$$c_o=\sqrt{E/\rho} \tag{2.31}$$

$$\left.\begin{matrix}\alpha^2\\ \beta^2\end{matrix}\right\}=\frac{p^2}{2}\left[\mp\left(1+\frac{E}{\kappa G}\right)+\sqrt{\left(1-\frac{E}{\kappa G}\right)^2+\frac{4l^2wt}{p^2 I}}\right] \tag{2.32}$$

Figure 2.12 shows the normalized fundamental resonance frequency ω/ω_o, plotted as a function of l/t using the Classical and Timoshenko beam theories.

$$\omega_o=\frac{(k_n l)^2}{l\sqrt{12}}\sqrt{\frac{E}{\rho}} \tag{2.33}$$

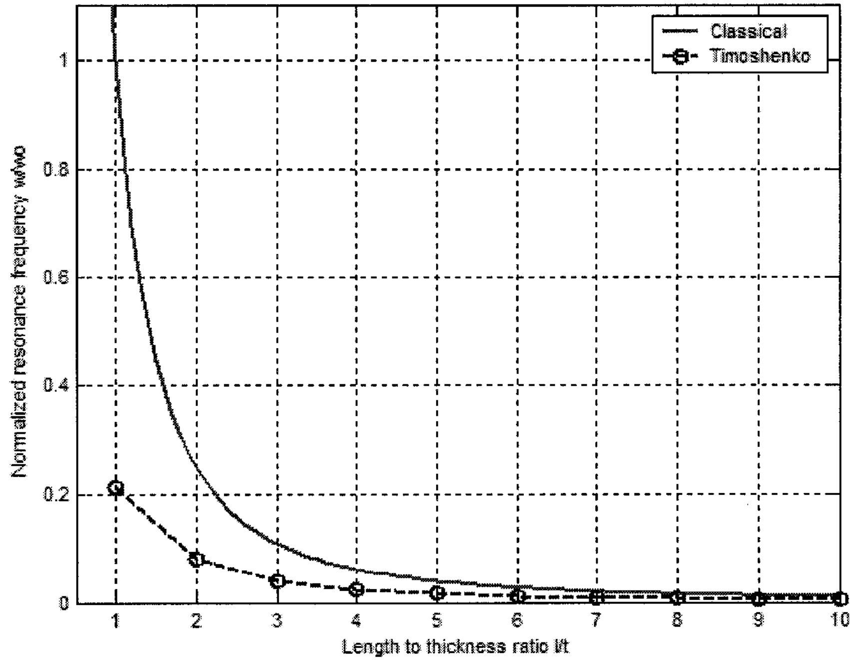

Fig. 2.12 Normalized fundamental resonance frequency, n=1, as a function of beam length/thickness ratio

As l/t decreases, the frequency using the Timoshenko theory (equation 2.29) drops with respect to the classical theory (equation 2.25) but, at values of l/t above 10 the two theories result in almost identical normalized resonance frequencies.

Figure 2.13 presents the first four flexural modal shapes for the fabricated MEMS resonators, as shown in this figure for the first or fundamental mode in (a) there are only two nodes, fixed points, at the ends but, for the higher modes there are extra nodes along the beam. For example, for the second transverse modal shape in (b) there is another node at the center of the beam.

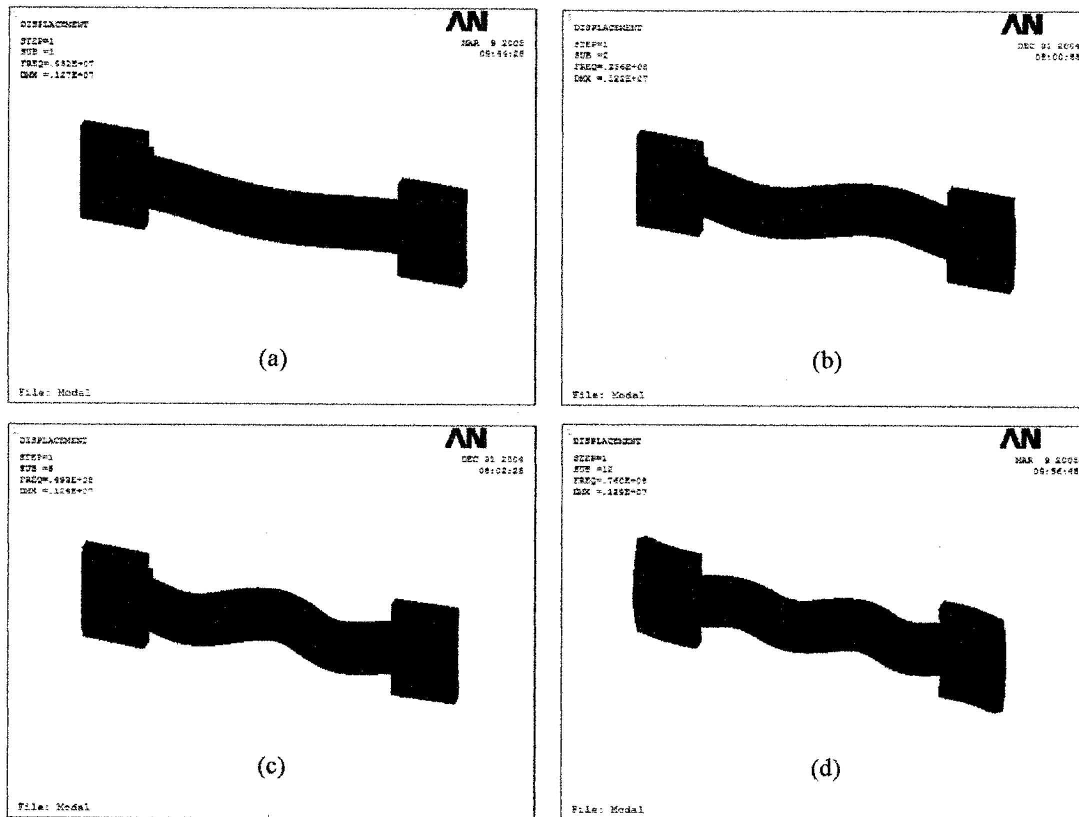

Fig. 2.13 Fundamental (a), 2nd (b), 3rd (c), and 4th (d) flexural modal shapes of the clamped-clamped MEMS resonator

The modal shape of the MEMS resonator vibrating in the transverse direction depends on the frequency of the applied ac input signal. If the frequency of the input signal is within the bandwidth for the first modal frequency, then the resonator vibrates in the first mode and by increasing the frequency of input signal, it vibrates in higher modes. The

vibration in higher modes is not strong enough to generate considerable deflection along the beam and as a result the induced output current by the capacitive transducer is very small and it's very difficult to sense this current to generate an output voltage. To be able to use the described micromechanical resonators in higher modes it is necessary to reduce the capacitive gap between the resonator beam and the drive electrode which is a limitation of the technology used to fabricate these devices.

2.2.4 Flexural-Mode Disk Resonator

In this section the analysis of a freely vibrating thin flexural-mode disk is presented. The mechanical wave-equation in Cartesian coordinates involves derivatives in both x and y directions compared to the mechanical wave-equation for the flexural beam in equation 2.13, which is a function of only x and t [8].

$$\frac{\partial^4 u}{\partial x^4}+\frac{\partial^4 u}{\partial y^4}+2\frac{\partial^4 u}{\partial x^2 \partial y^2}=\frac{1}{c^2}\frac{\partial^2 u}{\partial t^2} \quad 2.34$$

where the propagation velocity c is

$$c=\sqrt{\frac{Et^2}{12\rho(1-\upsilon^2)}} \quad 2.35$$

t is the disk thickness, υ is the Poisson's ratio, and u is the displacement in the z direction as shown in figure 2.14.

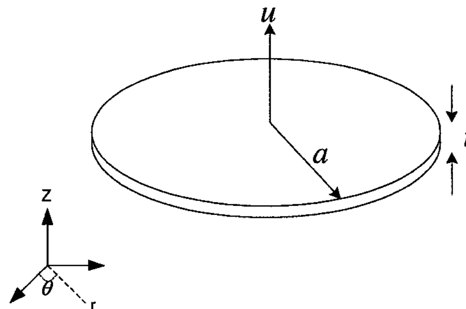

Fig. 2.14 Flexural-Mode disk resonator

Equation 2.34 can be solved by substituting $u = u_1 e^{j\omega t}$ into 2.34 and transferring it to the polar coordinates. The procedure is the same classical method used for the flexural-mode beam resonators and the general solution is obtained as [8]

$$u(r,\theta) = \left[AJ_n(kr) + BI_n(kr)\right]\cos n\theta \qquad 2.36$$

where r is the radial distance from the center of the disk and θ is the angular distance shown in figure 2.13. n is the number of nodal diameters and J and I are the Bessel functions. The dispersion relationship can be found by substituting 2.36 in 2.34 as

$$k^2 = \frac{\omega}{c} \qquad 2.37$$

The propagation constant k has a different value for each combination of nodal diameters n and nodal circles s. The next step is to apply the boundary conditions to the general solution in 2.36, the fabricated MEMS resonators are anchored around the periphery of the disk and the boundary condition is

$$u(a,\theta) = 0 \qquad 2.38$$

The frequency equation can be determined using the boundary conditions and because of the complexity in calculations we just state the frequency equation as [8]

$$2(\upsilon - 1) + \left[ka\frac{J_0(ka)}{J_1(ka)} + \frac{I_0(ka)}{I_1(ka)}\right] = 0 \qquad 2.39$$

Then the resonant frequency for $n = 0$ is obtained using the dispersion equation in 2.37 as

$$f_s = (ka)_s^2 \frac{t}{\pi d^2}\sqrt{\frac{E}{3\rho(1-\upsilon^2)}} \qquad 2.40$$

$(ka)_s$ is the root of the frequency equation for $s = 1,2,3,\dots$, which is a function of Poisson's ratio, υ, this is in contrast with the flexural-mode beam resonator [8]. As in the case of the flexural-mode beam, the classical theory ignores the effects of rotary inertia and shear, for thick disk resonators we have to use a theory such as Timoshenko but, due to the fact that for the fabricated disk resonators the radius is much larger than the thickness, we can use the classical theory and we will use equation 2.40 during the design phase. The four lowest possible vibration modes of a disk resonator clamped around the

periphery is depicted in figure 2.15, the blue color shows the nodal circles and diameters and the red color is used for the regions with maximum vibration.

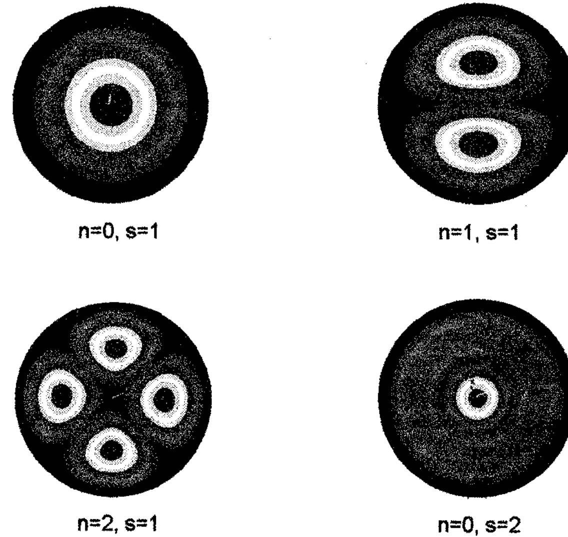

Fig. 2.15 Four lowest flexural vibration modes of a disk resonator

A schematic view of the fabricated MEMS resonator is presented in figure 2.16 along with the drive and sensing circuitry. As the flexural-mode beam resonator if the frequency of the applied electrical input signal v_{in} is close to one of the modal resonance frequencies of the MEMS resonator then the electrical energy will be converted to mechanical vibration through the capacitive transducer. This vibration generates an output electrical current at the output port following through the load resistor and hence an output electrical signal. As a result the structure shown in this figure acts like a band-pass filter with a very narrow bandwidth.

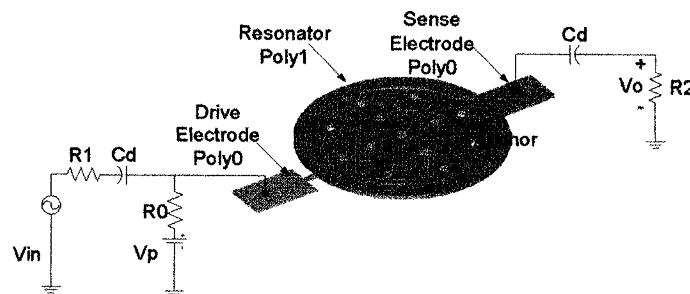

Fig. 2.16 Schematic view of the MEMS disk resonator

2.2.5 Lumped-Element Mechanical Modeling of Resonators

The equivalent lumped-element mechanical and electrical circuits of micromechanical resonators which will be explained in this section simplify the design process and make our understanding of micromechanical filters more clear. First we will drive an equivalent mechanical circuit consisting of springs, masses, and dampers then using the electromechanical analogy the mechanical circuit will be converted to its electrical analogy.

Converting from the flexural-mode beam resonator to a spring-mass-damper system is a network simplification but it is not an exact conversion. The beam resonator as shown before has infinite number of modal resonance frequencies; however the number of lumped-element equivalent circuit resonance frequencies are limited by the number of springs and masses used in the model, thus lumped-element model can be used only for a frequency range near one of the modal resonance frequencies but, due to the fact that high-Q MEMS resonators are narrow-bandwidth devices, the lumped-element models are still very useful in filter synthesis. This disadvantage of lumped-element modeling can be treated using distributed-element modeling as explained in [34].

For the flexural-mode beam resonators, the displacement along the x-axis can be found by substituting the roots 2.22 of each mode into equation 2.20 and then calculating the ratio

$$\frac{A}{B} = \frac{\sinh(kl) - \sin(kl)}{\cosh(kl) - \cos(kl)} \qquad 2.41$$

From 2.16 and the fact that $A = -C$ and $B = -D$,

$$u_1(x) = B\left[\frac{A}{B}(\cosh kx - \cos kx) + (\sinh kx - \sin kx)\right] \qquad 2.42$$

The final solution for the mechanical wave-equation is

$$u(x,t) = u_1(x)e^{j\omega t} = B\left[\frac{A}{B}(\cosh kx - \cos kx) + (\sinh kx - \sin kx)\right]e^{j\omega t} \qquad 2.43$$

Using the displacement $u(x,t)$ we can find the equivalent mass of the resonator in y-direction. Since $V(x)$ is the time derivative of $u(x,t)$,

$$V(x) = \frac{\partial u(x,t)}{\partial t} = j\omega u(x,t) \qquad 2.44$$

We can use equation 2.43 to find [8]

$$M_{eq} = \frac{K.E.}{1/2V_x^2} = \frac{1/2\rho A \int_0^l V^2(x)dx}{1/2V_x^2} \qquad 2.45$$

The kinetic energy is found by numerically integrating and evaluating the square of equation 2.42 and then multiplying the integral by ω^2. The first modal frequency of the beam resonator is found by the general equation 2.24 and setting $n = 1$. By assuming that K and M are the effective stiffness and mass of the resonator respectively, then this fundamental modal frequency can be used to find the effective stiffness

$$f_1 = \frac{1}{2\pi}\sqrt{\frac{K}{M}} \qquad 2.46$$

$$K(x) = (2\pi f_1)^2 M(x) \qquad 2.47$$

where $M(x)$ is the effective mass along the beam according to equation 2.45 and Finally the equivalent damping of the beam at location x along the beam length can be written as

$$D(x) = \frac{\sqrt{K(x)M(x)}}{Q_{res}} \qquad 2.48$$

Q_{res} is the quality factor of the resonator. Figure 2.17 shows a simplified lumped element mechanical model of the clamped-clamped flexural-mode beam resonator in figure 2.10, based on the values for the equivalent mechanical circuit elements found in 2.45, 2.47, and 2.48. C_o is a capacitor representing the capacitive electromechanical transduction which will be explained in the next section and C_d is the coupling capacitor which is assumed to be short circuit at the operating frequency range.

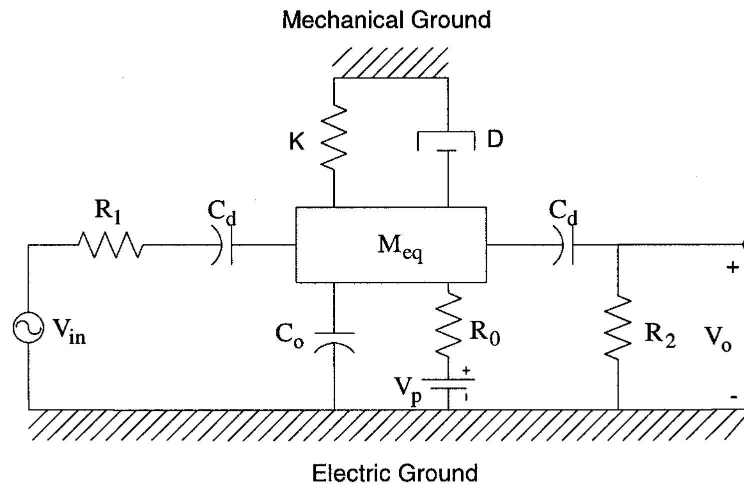

Fig. 2.17 Lumped-element mechanical modeling of the clamped-clamped beam resonator

2.2.6 Lumped-Element Electrical Modeling of Resonators

The electrical equivalent circuit model is of most importance in filter synthesis and design since most of the computer programs and literature on filter design is expressed in electrical terms. Therefore instead of using the mechanical equivalent circuits, the mechanical networks are usually transformed to their electrical analogies. The resonators in this work utilize capacitive transduction, for the described clamped-clamped beam resonator the capacitor is formed between the resonator beam and the underlying drive electrode as shown in figure 2.10. To actuate the resonator an input voltage comprised of a dc-bias potential V_p and an ac signal v_{in}, is applied across the electrode to resonator transducer capacitor. The dc bias V_p is applied to one plate of the capacitor and there is no dc current associated with it, so no dc power consumption. This combination of voltages generates an electrostatic force between the electrode and resonator, with the most dominant component at the frequency of v_{in}. Here in order to find the relationship between the applied voltages and the resonator operation the principals of electromechanical transducers will be presented.

Electromechanical transducers are used to convert electrical energy into mechanical energy and vice versa. They are used for electrical actuation and sensing of mechanical displacements and forces in a wide variety of applications. An illustrative example of a sensing device is a microphone in which a sound pressure is converted into an electrical

signal. In a loudspeaker, on the other hand, an electromechanical transducer is used to convert the electrical output signal into a mechanical vibration of the speaker's diaphragm [33].

The behavior of electromechanical transducers can be described by the differential equations, by the characteristic equations of the transducer element, and by a set of boundary conditions. However a very explanatory and quick way of gaining a deeper insight into the dynamic behavior of the transducer is the equivalent circuit approach, in which both electrical and mechanical portions of the transducer are represented by electrical equivalent circuits. The purpose of this section is to derive equivalent circuit representation of a two-port electromechanical transducer based on electrostatic transduction principle and then to obtain a lumped-parameter electrical model for the MEMS resonators.

Figure 2.18 shows a schematic view of a linear electromechanical transducer with a single electrical and a single mechanical port. Exchange of energy between the transducer and the outside world is achieved through the ports, depicted as a pair of terminals.

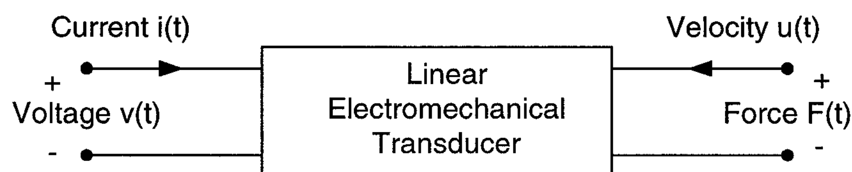

Fig. 2.18 A schematic view of a two-port electromechanical transducer

A port is defined by a pair of conjugate dynamic variables called '*effort*' and '*flow*'. The power exchange through the port is given by the product of effort and flow. The flow is given by the time derivative of the corresponding '*state*' variable. Electrical ports are defined by the {voltage (v), current (i) } pair, and mechanical ports by the {force (F), velocity (u) } pair. The state variables associated with the mechanical and the electrical ports are displacement x and the electric charge q, respectively.

An elementary electromechanical transducer with electrostatic transduction is shown in figure 2.19. This transducer is a transverse electrostatic transducer where the plates move transverse or perpendicular to each other.

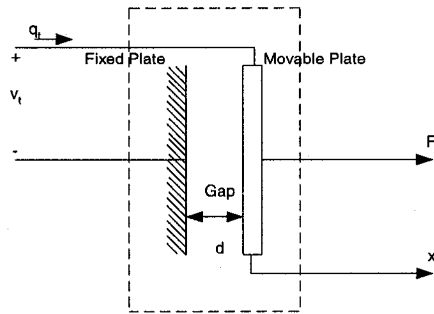

Fig. 2.19 Elementary parallel plate electrostatic transducer [33]

The transducer shown in figure 2.19 displays non-linear behavior because of the quadratic dependency of the electrostatic force on the charge or the applied voltage as will be further clarified. Linear behavior is achieved for incremental or small-signal variations around bias or equilibrium levels. In fact, if only the first two terms in a Taylor series expansion about a static equilibrium point are included, the total signal, which is indicated with a subscript 't', can be written as the sum of an equilibrium signal, indicated by a subscript '0', and the incremental signal, without any subscript, example, $x_t(t) = x_0(t) + x(t)$. It is further assumed that the incremental small-signals are sinusoidal with driving frequency ω, $x(t) = x\exp(j\omega t)$, where x denotes a phasor. This is not a real limitation since for a linear system by knowing the system's response to the sinusoidal small-signal input and using the techniques of Fourier transforms and Fourier series the response to any arbitrary signal is achievable [33].

The characteristic equations of an electromechanical transducer describe the linear relations that exist between small-signal variations of the port variables around the bias point. The characteristic equations of the two-port electrostatic transducer can be represented with matrix algebra. Two variables are chosen as the independent variables and the remaining two variables form the dependent set. For instance, in *constitutive* matrix representation of characteristic equations, we can choose effort variables {voltage $v(t)$ and force $F(t)$ } as the dependent variables and express them as a function of the state variables {charge $q(t)$ and displacement $x(t)$ }. The *transfer* matrix on the other hand relates the effort-flow variables at the electrical port, {voltage $v(t)$ and current $i(t)$ }, to those at mechanical port, {force $F(t)$ and displacement $x(t)$ }.

Here based on the conservation of system energy we will drive the constitutive matrix for the transverse electrostatic transducer in figure 2.19 [33, 34]. The electric energy W_e contained in the electrostatic transducer is given by [42]

$$W_e = W_e(q_t, x_t) = \frac{q_t^2}{2C(x_t)} = \frac{q_t^2(d + x_t)}{2\varepsilon_0 A_e} \qquad 2.49$$

Where $C(x_t) = \varepsilon_0 A_e /(d + x_t)$ denotes the capacitance as a function of x_t, A_e is the area of the capacitor plates, and d the spacing of the uncharged plates. Taking the total differential of W_e results in

$$dW_e = \left(\frac{\partial W_e}{\partial q_t}\right)_{x_t = cons} dq_t + \left(\frac{\partial W_e}{\partial x_t}\right)_{q_t = cons} dx_t \qquad 2.50$$

For a conservative transducer, the energy put into the transducer through the electrical and mechanical ports is given by [42]

$$dW_e = v_t dq_t + F_t dx_t \qquad 2.51$$

where v_t is the voltage between the plates and F_t is the mechanical force acting on the movable plate. Using equations 2.50 and 2.51

$$v_t(q_t, x_t) \equiv \left.\frac{\partial W_e(q_t, x_t)}{\partial q_t}\right|_{x_t = cons} = \frac{q_t(d + x_t)}{\varepsilon_0 A_e} \qquad 2.52$$

$$F_t(q_t, x_t) \equiv \left.\frac{\partial W_e(q_t, x_t)}{\partial x_t}\right|_{q_t = cons} = \frac{q_t^2}{2\varepsilon_0 A_e} \qquad 2.53$$

The force displays a quadratic dependence on the charge, which makes the system non-linear. The equations which describe the linear relations between the small-signal effort variables and state variables are called the constitutive equations. For the electrostatic transducer these are given by [33]

$$v(q, x) = \left.\frac{\partial v_t}{\partial q_t}\right|_{x=0} q + \left.\frac{\partial v_t}{\partial x_t}\right|_{q=0} x = \frac{(d + x_0)}{\varepsilon_0 A_e} q + \frac{q_0}{\varepsilon_0 A_e} x = \frac{1}{C_0} q + \frac{v_0}{x_0 + d} x \qquad 2.54$$

and

$$F(q, x) = \left.\frac{\partial F_t}{\partial q_t}\right|_{x=0} q + \left.\frac{\partial F_t}{\partial x_t}\right|_{q=0} x = \frac{q_0}{\varepsilon_0 A_e} q + 0.x = \frac{v_0}{x_0 + d} q + 0.x \qquad 2.55$$

To obtain the very last expression on the right hand side, the following equality was used: $q_0 = C_0 v_0 = \varepsilon_0 A_e v_0 / x_0$, where v_0 is the bias voltage and C_0 is the static capacitance.

The ideal transducer described in figure 2.19 is not stable. If the system is in equilibrium then the externally applied mechanical force is counterbalanced by the electrostatic force. Now if, due to some disturbance, the moveable plate is displaced a little in the direction of the fixed plate, the electrostatic force will be increased and the plates move toward each other, this in its turn results in a further increase of the electrostatic force. This will go on until the plates touch each other. Stability is easily attained by including a mechanical spring with constant k, as shown in figure 2.20.

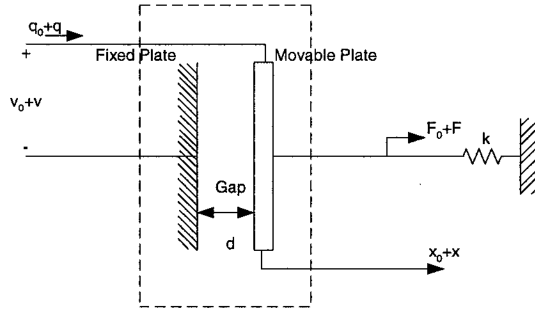

Fig. 2.20 A transverse electrostatic transducer stabilized with a spring [33]

Analytically this means that a mechanical energy term must be added to the energy function of 2.49, resulting in

$$W_{em} = W_{em}(q_t, x_t) = \frac{q_t^2}{2C(x_t)} + \frac{1}{2}k(x_t - x_r)^2 = \frac{q_t^2(d + x_t)}{2\varepsilon_0 A_e} + \frac{1}{2}k(x_t - x_r)^2 \qquad 2.56$$

Where x_r denotes the rest position of the spring. Equation 2.52 is not affected this way, but 2.53 becomes

$$F_t(q_t, x_t) \equiv \left.\frac{\partial W_{em}(q_t, x_t)}{\partial x_t}\right|_{q_t = cons} = \frac{q_t^2}{2\varepsilon_0 A_e} + k(x_t - x_r) \qquad 2.57$$

Finally the second constitutive equation, 2.55, must be replaced by

$$F(q,x) = \left.\frac{\partial F_t}{\partial q_t}\right|_{x=0} q + \left.\frac{\partial F_t}{\partial x_t}\right|_{q=0} x = \frac{q_0}{\varepsilon_0 A_e} q + kx = \frac{v_0}{x_0 + d} q + kx \qquad 2.58$$

The constitutive equations 2.54 and 2.58 are expressed as a function of the state variables (q,x). Sometimes it is useful to choose the voltage and the displacement as the independent variables. The electromechanical interactions are now described by equations of the (v,x) type, given by

$$q(v,x)=\frac{\varepsilon_0 A_e}{d+x_0}v-\frac{q_0}{d+x_0}x=\frac{\varepsilon_0 A_e}{d+x_0}v-\frac{\varepsilon_0 A_e v_0}{(d+x_0)^2}x \qquad 2.59$$

$$F(v,x)=\frac{q_0}{d+x_0}v+\left(k-\frac{q_0^2}{\varepsilon_0 A_e(d+x_0)}\right)x=\frac{\varepsilon_0 A_e v_0}{(d+x_0)^2}v+\left(k-\frac{\varepsilon_0 A_e v_0^2}{(d+x_0)^3}\right)x \qquad 2.60$$

The system is stable as long as $k>k'$, where $k'=\varepsilon_0 A_e v_0^2/(d+x_0)^3$, i.e., the second term within parentheses in 2.60. The constitutive equations in 2.54 and 2.58 can be defined by a matrix representation as

$$\begin{pmatrix} e_1 \\ e_2 \end{pmatrix}=B\begin{pmatrix} q_1 \\ q_2 \end{pmatrix} \qquad 2.61$$

The transfer matrix, as mentioned before relates the effort-flow variables at the electrical port to the effort-flow variables at the mechanical port.

$$\begin{pmatrix} e_1 \\ f_1 \end{pmatrix}=T\begin{pmatrix} e_2 \\ f_2 \end{pmatrix} \qquad 2.62$$

Table 2.4 summarizes the constitutive and transfer equations of the lumped-parameter transducer shown in figure 2.20, completed with a stabilization spring k at the mechanical port. The matrix equations describe the relations between the phasor quantities of the sinusoidal signals. The characteristic equations for the transducer without the spring k, as depicted in figure 2.19, can easily be obtained from the matrices in Table 2.4 by taking $k=0$.

State variables $\{q_1,q_2\}$	Effort variables $\{e_1,e_2\}$	Flow variables $\{f_1,f_2\}$	$\begin{pmatrix} e_1 \\ e_2 \end{pmatrix}=B\begin{pmatrix} q_1 \\ q_2 \end{pmatrix}$	$\begin{pmatrix} e_1 \\ f_1 \end{pmatrix}=T\begin{pmatrix} e_2 \\ f_2 \end{pmatrix}$
$\{q(t),x(t)\}$	$\{v(t),F(t)\}$	$\{i(t)=\dot{q}(t),u(t)=\dot{x}(t)\}$	$\begin{bmatrix} \frac{1}{C_0} & \frac{\Gamma}{C_0} \\ \frac{\Gamma}{C_0} & k \end{bmatrix}$	$\begin{bmatrix} \frac{1}{\Gamma} & \frac{-1}{j\omega\Gamma}\left(k-\frac{\Gamma^2}{C_0}\right) \\ \frac{j\omega C_0}{\Gamma} & -\frac{kC_0}{\Gamma} \end{bmatrix}$

Table 2.4 Constitutive and Transfer equations of the transverse electrostatic transducer

In the above matrix equations, Γ is the transduction factor and is equal to

$$\Gamma = \frac{q_0}{d + x_0} = \frac{\varepsilon_0 A_e v_0}{(d + x_0)^2} \qquad 2.63$$

The construction of the equivalent circuits starts with the transfer matrix given in Table 2.4. The transfer matrix of the transverse electrostatic transducer can be split into its constituent transfer matrices as follows

$$\begin{pmatrix} v \\ i \end{pmatrix} = \begin{bmatrix} \dfrac{1}{\Gamma} & \dfrac{-1}{j\omega}(k - k') \\ \dfrac{j\omega C_0}{\Gamma} & -\dfrac{kC_0}{\Gamma} \end{bmatrix} \begin{pmatrix} F \\ u \end{pmatrix} = \begin{bmatrix} 1 & 0 \\ j\omega C_0 & 1 \end{bmatrix} \begin{bmatrix} 1/\Gamma & 0 \\ 0 & -\Gamma \end{bmatrix} \begin{bmatrix} 1 & \dfrac{-1}{j\omega}(k - k') \\ 0 & 1 \end{bmatrix} \begin{pmatrix} F \\ u \end{pmatrix} \qquad 2.64$$

where $k' = \Gamma^2 / C_0$. In the matrix equation above, the center matrix represents the transducer. Each of the constituent transfer matrices can be represented by an equivalent network. The overall equivalent network consists of a cascade connection of these networks and is shown in figure 2.21 [33].

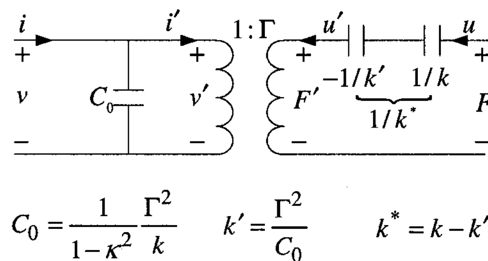

$$C_0 = \frac{1}{1 - \kappa^2} \frac{\Gamma^2}{k} \qquad k' = \frac{\Gamma^2}{C_0} \qquad k^* = k - k'$$

Fig. 2.21 Equivalent circuit representations of the transverse electrostatic transducer

According to the direct analogy between the electrical and mechanical systems, a spring is represented by a capacitor and the electromechanical coupling is modeled through an ideal electromechanical transformer with a transformer ratio given by Γ , called the transduction factor, which was introduced in Table 2.4. The transformer relations, are given by $F' = \Gamma v'$ and $i' = -\Gamma u'$. There is a spring with a negative constant $-k' = -\Gamma^2 / C_0 = -\varepsilon_0 A_e v_0^2 / (d + x_0)^3$, this spring is a result of the electromechanical coupling and leads to a lowering of the overall dynamic spring constant. This can be seen

by combining the two spring constants into a single spring with constant $k^* = k - k'$. As long as $k^* > 0$, the system is mechanically stable.

By considering the lumped-element mechanical model of the MEMS resonator shown in figure 2.17 and then by using the electrical circuit model of the transverse electrostatic transducer depicted in figure 2.21, an equivalent lumped-parameter electrical model can be defined for the whole system. The mechanical parts shown in figure 2.17 can be replaced by equivalent electrical components using the Newton's second law of motion to the mass m

$$\begin{aligned} F_m(t) - F_e(t) - kx(t) - D\dot{x}(t) - m\ddot{x}(t) = 0 \\ F_m - F_e - \frac{k}{j\omega}u - Du - j\omega mu = 0 \end{aligned} \qquad 2.65$$

where the second of the above equations is given in terms of the phasors of the respective quantities. Recalling that Newton's second law of motion is the electromechanical analogue of KVL, it is easy to show that the final circuit shown in figure 2.22 defines an equivalent circuit of the system. The equivalent circuit of figure 2.21, enclosed by the dashed box represents the transducer plus stabilization spring k.

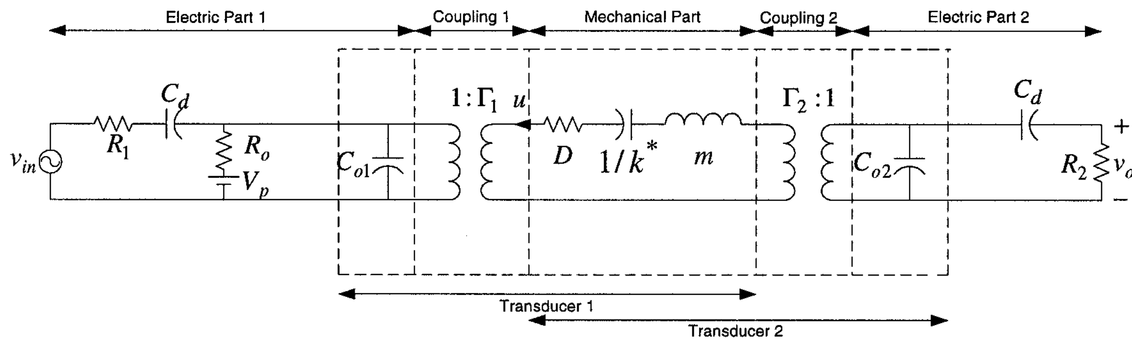

Fig. 2.22 An equivalent electrical circuit representation of the MEMS resonator

2.2.7 Theory of Coupled Resonators

The microelectromechanical band-pass filters in this work consist of mechanically coupled resonators and our starting point in discussing these band-pass filters is the simple system of spring-mass-damper coupled resonators as shown in figure 2.23. Each

mass element, m_i, is supported by a massless linear spring element with stiffness k_i and a damping factor c_i. The mechanical coupling between the resonators is presented with a coupling element of stiffness k_{12}.

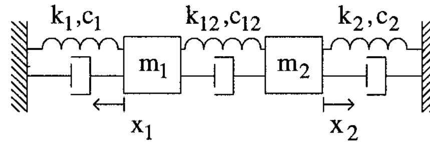

Fig. 2.23 Mechanical model for two coupled resonators

Assuming that an external mechanical force at frequency ω is applied on each resonator, the system of differential equations can be written as

$$\begin{aligned} m_1\ddot{x}_1 + (c_1 + c_{12})\dot{x}_1 + c_{12}\dot{x}_2 + (k_1 + k_{12})x_1 + k_{12}x_2 = f_1 e^{i\omega t} \\ m_2\ddot{x}_2 + (c_2 + c_{12})\dot{x}_2 + c_{12}\dot{x}_1 + (k_2 + k_{12})x_2 + k_{12}x_1 = f_2 e^{i\omega t} \end{aligned} \quad 2.66$$

For a system of n coupled resonators If an external mechanical force, $f_i e^{j\omega t}$, is applied on each resonator then the system of differential equations can be written in a matrix notation as [43]

$$[M]\{\ddot{X}\} + [C]\{\dot{X}\} + [K]\{X\} = \{F\}e^{j\omega t} \quad 2.67$$

where the column matrix $\{X\}$ is a set of generalized coordinates, x_i $(i = 1, 2, \ldots, n)$, describing the motion of the system and $\{F\}$ represents the externally applied force. $[M]$, $[C]$, and $[K]$ are called the mass, damping, and stiffness matrices, respectively. For example for $n = 4$

$$X = \begin{pmatrix} x_1 \\ x_2 \\ x_3 \\ x_4 \end{pmatrix} \text{ and } F = \begin{pmatrix} f_1 \\ f_2 \\ f_3 \\ f_4 \end{pmatrix} \quad 2.68$$

$$M = \begin{bmatrix} m_1 & 0 & 0 & 0 \\ 0 & m_2 & 0 & 0 \\ 0 & 0 & m_3 & 0 \\ 0 & 0 & 0 & m_4 \end{bmatrix} \quad 2.69$$

$$C = \begin{bmatrix} c_1 + c_{12} & c_{12} & 0 & 0 \\ c_{12} & c_2 + c_{12} + c_{23} & c_{23} & 0 \\ 0 & c_{23} & c_3 + c_{23} + c_{34} & c_{34} \\ 0 & 0 & c_{34} & c_4 + c_{34} \end{bmatrix} \quad 2.70$$

$$K = \begin{bmatrix} k_1 + k_{12} & k_{12} & 0 & 0 \\ k_{12} & k_2 + k_{12} + k_{23} & k_{23} & 0 \\ 0 & k_{23} & k_3 + k_{23} + k_{34} & k_{34} \\ 0 & 0 & k_{34} & k_4 + k_{34} \end{bmatrix} \quad 2.71$$

By assuming an exponential solution $\{X\} = \{A\}e^{j\omega t}$ and then introducing this solution in equation 2.67 it becomes

$$[-M\omega^2 + i\omega C + K]A = SA = F \quad 2.72$$

The natural resonance frequencies can be determined using equation 2.72 and setting the determinant of matrix S equal to zero. For example the resonance frequency of each coupled resonator in figure 2.23 is

$$\omega_i = \sqrt{\frac{k_i}{m_i}} \quad i = 1,2 \quad 2.73$$

If the resonators are identical then they are tuned to the same resonance frequency $\omega_1 = \omega_2 = \omega$. When x_1 and x_2 are $180°$ out of phase, there is no stretching in the coupling spring, k_{12} and it can be removed without affecting the vibration of the system. In other words the first natural resonance frequency occurs at ω. On the other hand when x_1 and x_2 are in phase with each other, the coupling spring will be stretched, however there is no displacement at the center of the spring and it can be replaced with a spring with stiffness $2k_{12}$ and the second natural resonance frequency is

$$\omega' = \sqrt{\frac{k_i + 2k_{12}}{m_i}} \quad 2.74$$

The bandwidth of a microelectromechanical filter consisting of a system of two coupled resonators, using 2.73 and 2.74 is equal to

$$\Delta\omega = \omega_i \left(\sqrt{1 + \frac{2k_{12}}{k_i}} - 1 \right) \quad 2.75$$

while for a single resonator the bandwidth depends on the quality factor of the resonator and is given by.

$$\Delta\omega_i = \frac{\omega_i}{Q_i} \quad i = 1, 2, ..., n \tag{2.76}$$

For each resonator the quality factor, Q_i, is defined as

$$Q_i = \frac{m_i \omega_i}{c_i} = \frac{\sqrt{k_i m_i}}{c_i} \tag{2.77}$$

Figure 2.24 shows the amplitude and phase response of the input and output resonators in a system of two coupled resonators obtained by SystemVision where the input force is applied only to the first resonator, $f_1 = 1$ and $f_2 = 0$. The resonators are identical, $m_1 = m_2$, $k_1 = k_2$, and are weakly coupled with a spring constant $k_{12} = 0.01k_i$. For the amplitude response there are two peaks, one at ω_i and the other one at $\omega' = \sqrt{1.02}\omega_i$ according to equations 2.73 and 2.74.

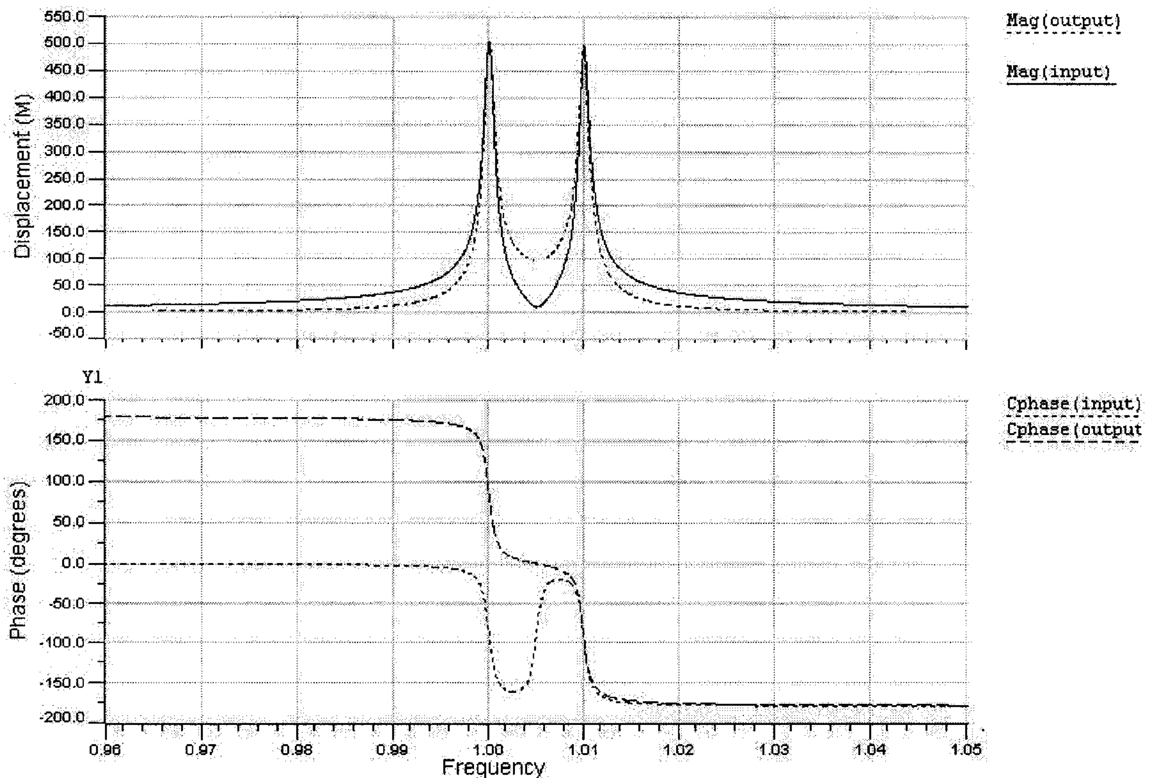

Fig. 2.24 Amplitude and phase response of two coupled resonators versus ω / ω_i

The Q factor of each resonator is supposed to be $Q_i = 1000$. Because of such a big quality factor the bandwidth of constituent resonators obtained by equation 2.76 is much smaller than the filter bandwidth in 2.75 which results in a non-uniform amplitude characteristic. For a filter to have a flat frequency response the band-width of constituent resonators should be equal to or greater than the overall band-width of the filter

$$\frac{\omega_i}{Q_i} \geq \left(\sqrt{1+\frac{2k_{12}}{k_i}}-1\right)\omega_i \text{ or } Q_i \leq \left(\sqrt{1+\frac{2k_{12}}{k_i}}-1\right)^{-1} \qquad 2.78$$

For the amplitude response presented in figure 2.24 in order to have a flat characteristic the quality factor should be less than 100 using equation 2.78, where the stiffness of the coupling spring, k_{12} is $k_{12} = 0.01k_i$. Figure 2.24 shows the amplitude response of the output resonator, the same conditions are applied for the resonators and three different values of quality factor, $150, 100,$ and 75 have been used, instead of 1000. According to equation 2.77 lower quality factor results in higher damping loss and as shown in figure 2.25 the amplitude of the output resonator is decreased by around $5dB$ because of the reduced quality factor.

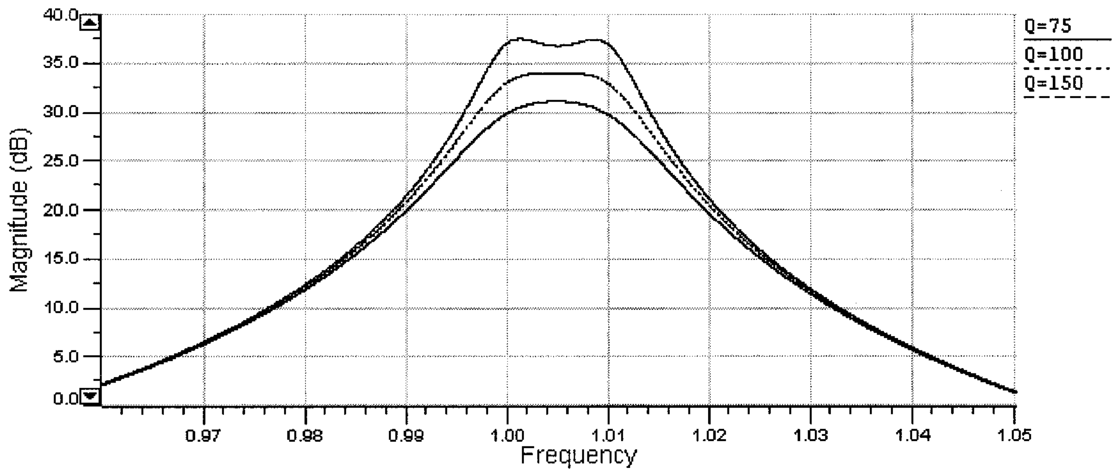

Fig. 2.25 Amplitude response for three different Q-factors

In a system of more than two coupled resonators as shown in figure 2.26(a) the end resonators are only coupled to the nearest resonators while the interior resonators are coupled from both sides, this will cause an asymmetry in filter's characteristics. This asymmetry is more evident in equations 2.70 and 2.71 where the $(c,k)_{11}$ and $(c,k)_{44}$

elements are not equal to the remaining diagonal elements. By arranging the resonators in a closed ring as shown in figure 2.26(b) this asymmetry will be resolved [44].

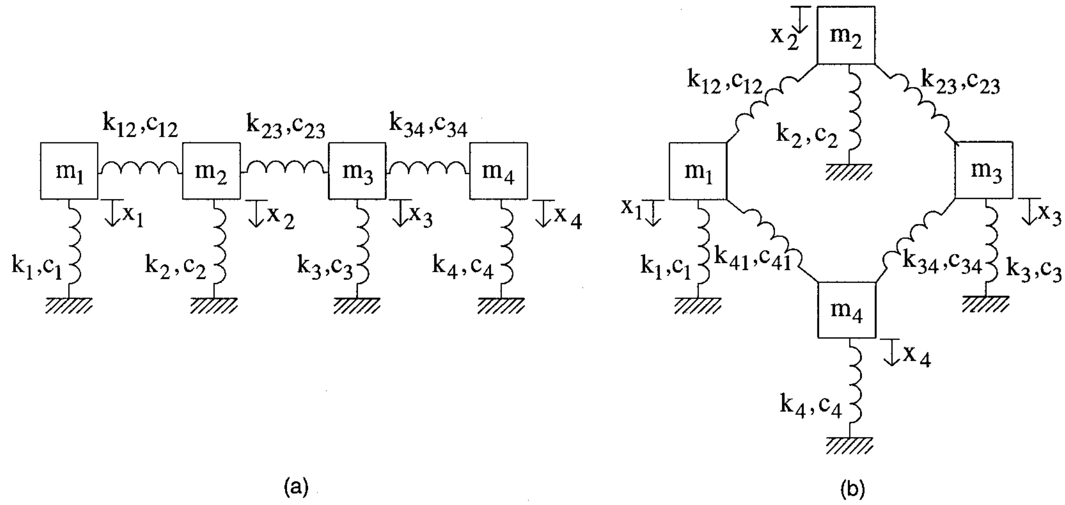

Fig. 2.26 Coupled resonators in open ring (a) and closed ring (b) configurations

For a system of four coupled resonators the new damping and stiffness matrices become

$$C = \begin{bmatrix} c_1 + c_{12} + c_{41} & c_{12} & 0 & 0 \\ c_{12} & c_2 + c_{12} + c_{23} & c_{23} & 0 \\ 0 & c_{23} & c_3 + c_{23} + c_{34} & c_{34} \\ 0 & 0 & c_{34} & c_4 + c_{34} + c_{41} \end{bmatrix} \qquad 2.79$$

$$K = \begin{bmatrix} k_1 + k_{12} + k_{41} & k_{12} & 0 & 0 \\ k_{12} & k_2 + k_{12} + k_{23} & k_{23} & 0 \\ 0 & k_{23} & k_3 + k_{23} + k_{34} & k_{34} \\ 0 & 0 & k_{34} & k_4 + k_{34} + k_{41} \end{bmatrix} \qquad 2.80$$

The calculated amplitude and phase response for the third resonator in the system of four coupled identical resonators in both closed ring and open ring configurations are shown in figure 2.27. The drive signal is applied to the first resonator. For the open ring configuration the smallest amplitude response is obtained for the 4th resonator but, for the closed ring configuration the smallest amplitude is for the 3rd resonator which is the furthest one from the drive resonator (resonator 1). From figure 2.27 we can see that the response in the closed ring configuration is symmetric about the center frequency.

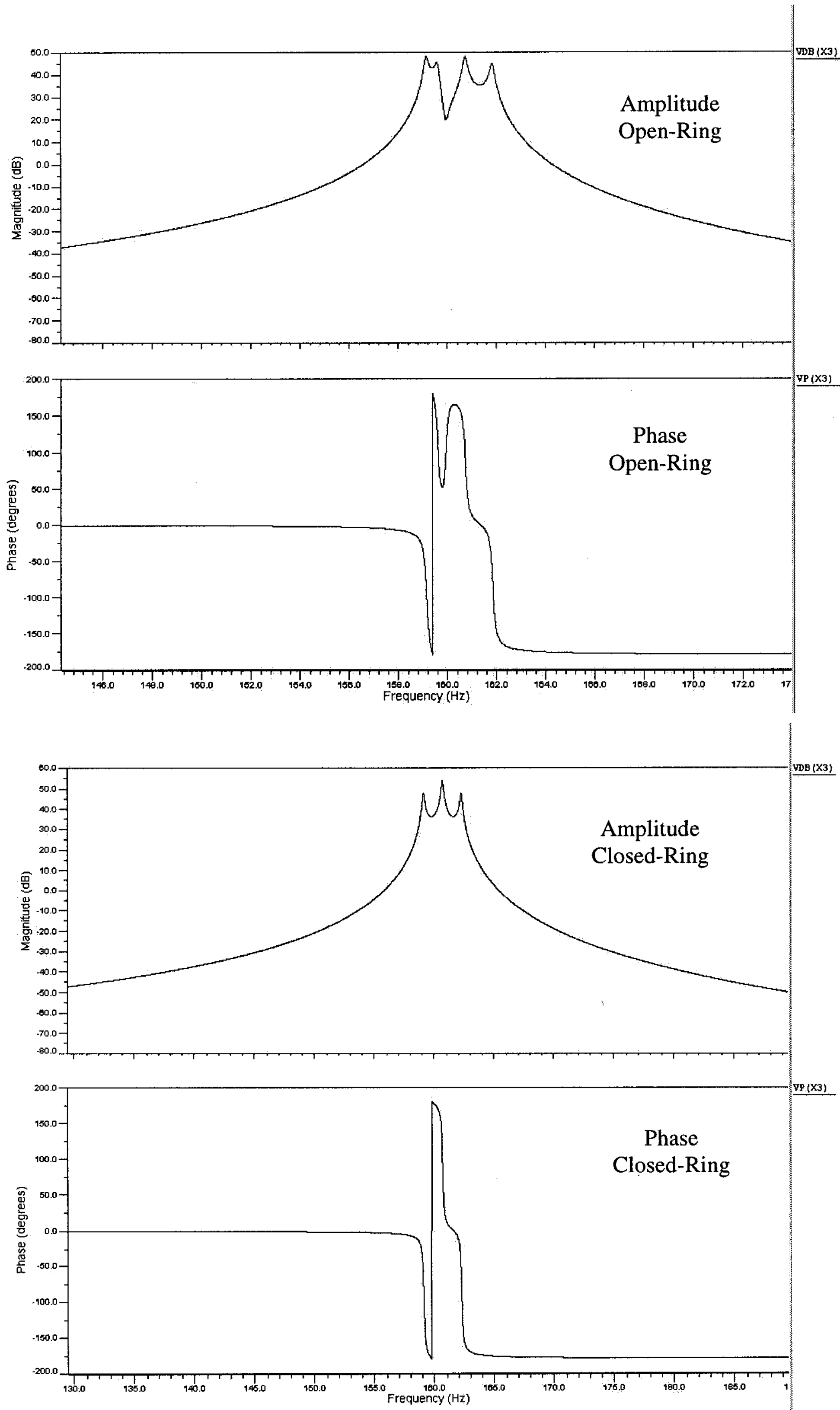

Fig. 2.27 Frequency response of the 3rd resonator, in a system of four coupled resonators

2.2.8 Coupling Element

If the coupled resonators are identical with the same resonance frequency then the overall filter pass-band and center frequency will be determined by the stiffness of the coupling element, k_s, and the effective stiffness of resonators at the coupling location, k_{rc} as [37]

$$\frac{\Delta\omega}{\omega_o} = \frac{k_s}{k_{rc}k_{12}} \quad 2.81$$

where k_{12} is the normalized coupling coefficient between resonator tanks for a given filter type (Butterworth, Chebyshev, ...) and depends on the filter insertion loss and can be found in filter handbooks. The stiffness of the coupling element can be determined by using equation 2.81 and proper element geometry. The most common coupling method is simply to attach the resonators by means of another flexural beam element with a smaller cross-section as shown in figure 2.28. However there are other coupling methods such as extensional and torsional modes [8] which won't be discussed in this work.

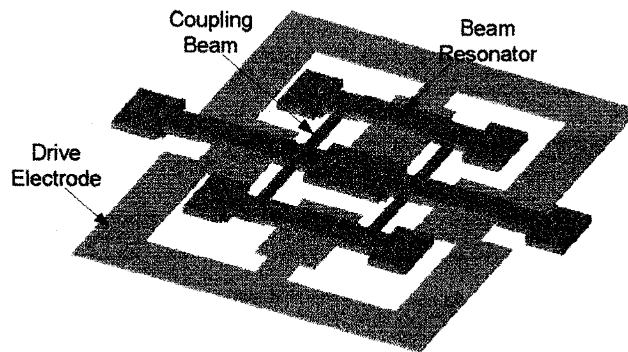

Fig. 2.28 Coupled MEMS resonators

An important issue which should be taken into account during the coupling beam design is the effect of its mass on the center frequency of the resonators. Especially in the case of micro beams, the mass of the coupling beam is in the same order of the resonator itself and will be added to the resonator mass, changing its center frequency and in turn, changing the filter center frequency. The equations describing flexural-mode coupling are very complicated because they include the bending moment M and angular velocity $\dot{\theta}$

variables as forces and velocities [8]. The equivalent networks for transversely vibrating beams under various end conditions were discussed in literature completely [45]. Figure 2.29(a) shows the typical end conditions for the flexural coupling elements used in this work. At high frequencies the coupling beam is more accurately modeled by an acoustic transmission line [37] which is the mechanical analog to the electrical transmission line as shown in figure 2.29(b).

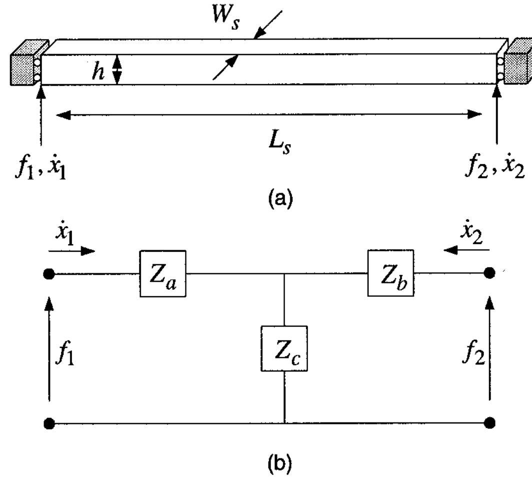

Fig. 2.29 Flexural coupling element (a) and its equivalent transmission line model (b)

From reference [45] the mechanical impedance behavior of the coupling beam as seen by the attached resonators can be conveniently modeled via an impedance matrix of the form

$$\begin{bmatrix} f_1 \\ \dot{x}_1 \end{bmatrix} = \begin{bmatrix} \dfrac{H_6}{H_7} & -\dfrac{2EI_s\alpha^3 H_1}{j\omega L_s^3 H_7} \\ -\dfrac{j\omega L_s^3 H_3}{EI_s\alpha^3 H_7} & \dfrac{H_6}{H_7} \end{bmatrix} \begin{bmatrix} f_2 \\ \dot{x}_2 \end{bmatrix} \tag{2.82}$$

$$\begin{aligned} H_1 &= \sinh\alpha \sin\alpha \\ H_3 &= \cosh\alpha \cos\alpha - 1 \\ H_6 &= \sinh\alpha \cos\alpha + \cosh\alpha \sin\alpha \\ H_7 &= \sin\alpha \sinh\alpha \\ \alpha &= L_s(\rho W_s h\omega^2 /(EI_s))^{0.25} \end{aligned} \tag{2.83}$$

I_s is the bending moment of inertia defined by equation 2.14 for the coupling beam and the other dimensions are shown in figure 2.29(a). Equating the transfer matrix of the T network in figure 2.29(b) to the transfer matrix in 2.82, then solving for the shunt and series impedances yields [36]

$$Z_a = Z_b = \frac{jEI_s\alpha^3(H_6 - H_7)}{\omega L_s^3 H_3} \text{ and } Z_c = \frac{jEI_s\alpha^3 H_7}{\omega L_s^3 H_3} \qquad 2.84$$

In order to cancel the effect of the coupling element mass on the filter center frequency, the coupling beam should be designed to correspond to a quarter wavelength of the filter center frequency. This can be achieved by choosing coupling beam dimensions such that the series and shunt impedances of figure 2.29(b) take on equal and opposite values, and thus, cancel each other. From equation 2.84, this happens when

$$H_6 = \sinh\alpha\cos\alpha + \cosh\alpha\sin\alpha = 0 \qquad 2.85$$

With quarter wavelength dimensions for the coupling element, the impedances are given by

$$Z_a = Z_b = \frac{EI_s H_7}{j\omega L_s^3 H_3} = \frac{1}{C_{sa} j\omega} \qquad 2.86$$

$$Z_c = -\frac{EI_s H_7}{j\omega L_s^3 H_3} = \frac{1}{C_{sc} j\omega} \qquad 2.87$$

Figure 2.30 presents an equivalent electrical circuit for the coupling element between the resonators. This circuit is developed using equations 2.86 and 2.87, η_c is the transformer turns ratio which depends on the coupling beam location and can be obtained by

$$\eta_c = \sqrt{\frac{k_{rc}}{k_r}} \qquad 2.88$$

k_{rc} and k_r are the stiffness of the resonator beam at the coupling point and the overall effective stiffness as defined by 2.47.

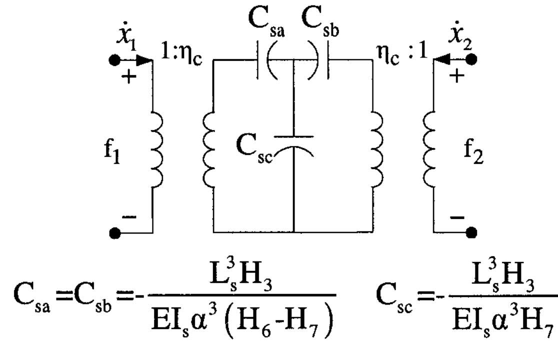

Figure 2.30 Equivalent electrical model of the flexural coupling element

The quality factor of the final filter is proportional to the ratio of the coupling element stiffness and the resonator stiffness at the location point and is given by using 2.81

$$Q_{fltr} = \frac{\omega_o}{\Delta\omega} = k_{12}(\frac{k_{rc}}{k_s}) \qquad 2.89$$

In microelectromechanical filters, the resonators and the couplers are almost the same size and this limits the maximum attainable quality factor. On the other hand as mentioned before in order to cancel the effect of the coupling element mass on the filter center frequency we need quarter wavelength coupling beam. A new method to design filters with different bandwidths, with the same quarter wavelength coupling beam, takes advantage of the fact that the dynamic spring constant k_{rc} of a clamped-clamped flexural-mode beam varies along the beam length and is larger at locations closer to the anchor points, i.e., it is larger at points moving with lower velocity at resonance. This can be verified using 2.45 and 2.47. Figure 2.31 illustrates this point with a plot of the velocity along the beam length, where the velocity is maximized at the center of the beam. Thus by changing the coupling point along the beam it is possible to obtain different filter bandwidth and quality factor with the same geometries.

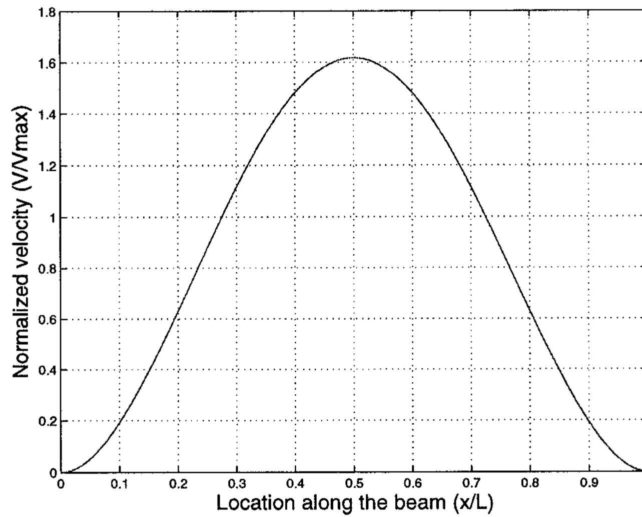

Fig. 2.31 Normalized velocity along the beam length

2.2.9 Lumped-Element Modeling of Filters

Based on the lumped-element models developed for the MEMS resonators and coupling elements in previous sections, the equivalent lumped-parameter mechanical model of a filter composed of two coupled resonators is shown in figure 2.32 where the resonators are modeled with a spring-mass-damper system. For simulation purposes it is more convenient to develop a macromodel that represents both the mechanical and electrical parts by equivalent electrical circuits which is presented in figure 2.33.

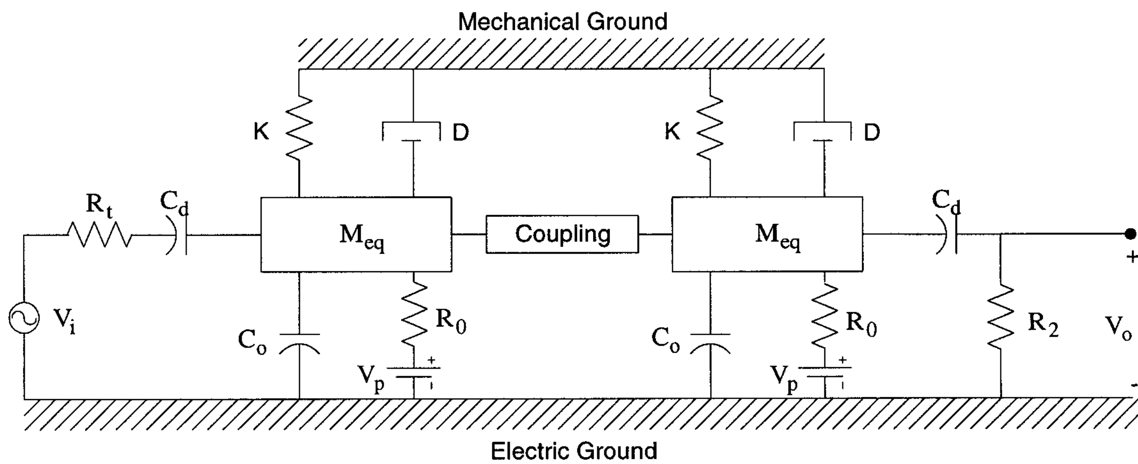

Fig. 2.32 Lumped-Element mechanical model of the microelectromechanical filter

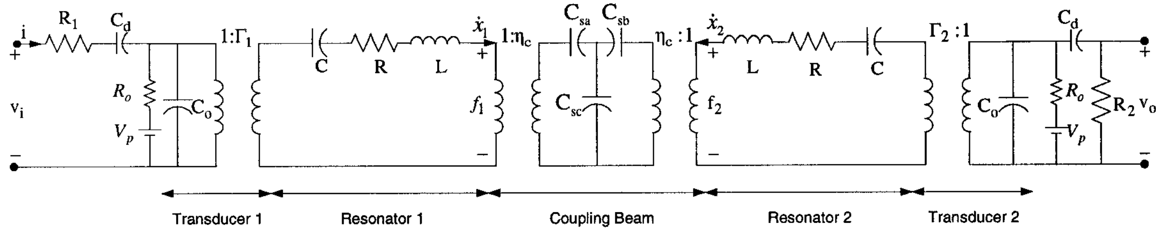

Fig. 2.33 Lumped-Element electrical model of the microelectromechanical filter

In developing the equivalent electrical model presented in figure 2.33 as explained in section 2.2.6 we used the basic principles of electromechanical transduction and the electrical and mechanical equations of equilibrium. However these equivalent circuits can be used for a better visualization of the system and to investigate the effects of modifications to the structure, but as they are developed by linearization around a bias point, they can not reflect the nonlinear and large signal behavior of the system. This limitation of lumped-element electrical models will be resolved using the behavioral modeling and Reduced Order Modeling (ROM) techniques which will be explained in next section.

2.2.10 Behavioral Modeling and System-Level Simulation

As explained in section 1.4 system-level simulation of current system on chip MEMS designs require the integration of the analog and digital sensing circuitry besides the nonelectrical MEMS components in a unique mixed-domain simulator. However the equivalent electrical models for the MEMS resonators discussed before can be used in a circuit simulator besides the analog and digital circuits, but they are limited to small-signal analysis and furthermore these models are based on analytical description of the structure which is not possible for MEMS structures having complex geometries. Behavioral modeling and reduced order modeling approaches can be used respectively to overcome these shortcomings of equivalent electrical models. Figure 2.34 presents the system level modeling methodologies using equivalent lumped element networks and reduced order models imported from a FEM analysis by ANSYS. The generated macromodels are used as inputs to a VHDL-AMS simulator, AdvanceMS from Mentor Graphics. [46]

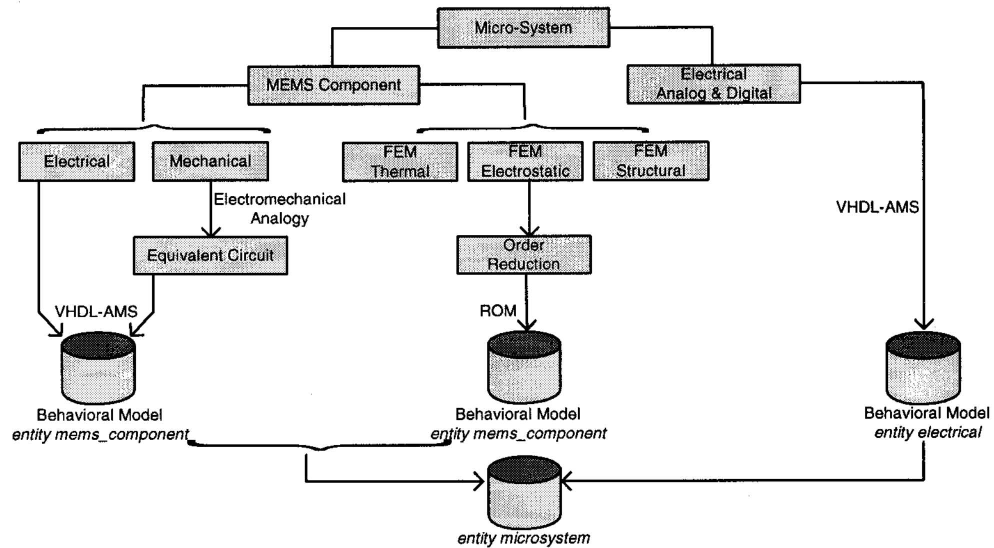

Fig. 2.34 System level modeling methodologies [46]

In this part, we present the application of lumped element equivalent networks and reduced order modeling (ROM) in behavioral modeling of a 10MHz microelectromechanical filter based on four coupled flexural-mode MEMS resonators. Design specifications, material properties, and geometries of the resonators, coupling elements, and the filter itself, are summarized in Table 2.5. More details on the fabrication and design of the filter using the PolyMUMPs process will be explained in chapter 3.

Parameter	Value	Units	Parameter	Value	Units
Beam Length, L_r	40	μm	Filter Band Width, $\Delta\omega$	19.31	KHz
Beam Width, W_r	8	μm	Filter Quality Factor, Q_{fltr}	500	–
Beam Thickness, h	2	μm	Coupling Beam Length, L_s	17.25	μm
Electrode Width, W_e	16	μm	Coupling Beam Width, W_s	2	μm
Electrode-to-Beam Gap, d_o	0.75	μm	Coupling Location, l_c	5	μm
Resonator Q	13834	–	Center Frequency, f	9.6562	MHz
Resonator Mass, m_r	5.9058×10^{-13}	Kg	Modification Factor, κ	0.9002	–
m_r at coupling point, m_{rc}	1.8726×10^{-11}	Kg	Poisson's Ratio, ν	0.225	–
Resonator Stiffness, k_r	2174	N/m	Young's Modulus, E	163	GPa
k_r at coupling point, k_{rc}	68931	N/m	Density of Polysilicon, ρ	2330	Kg/m^3
Damping Constant, C_r	2.5901×10^{-9}	Ns/m	DC Bias, V_p	80	V

Table 2.5 Design specifications and geometries of the 10MHz band-pass filter

For the 10MHz filter, we will use the same small-signal lumped-parameter model presented in figure 2.33 with four coupled MEMS resonators and element values listed in Table 2.6. In developing small-signal electrical macromodels the electrical models of the transverse electrostatic transducer have been developed using the linearization method around a bias point and as a result it can not be used for large-signal non-linear analysis. This limitation can be resolved by using behavioral description of the transducers in VHDL-AMS during the generation of macromodels.

Parameter	**Value**	**Units**	**Parameter**	**Value**	**Units**
L	5.9058×10^{-13}	H	η_c	5.6309	C/m
C	4.5998×10^{-4}	F	C_{sa}	-3.3133×10^{-3}	F
R	2.5901×10^{-9}	Ω	C_{sb}	-3.3133×10^{-3}	F
C_o	1.5111	fF	C_{sc}	1.7036×10^{-3}	F
Γ	1.6118×10^{-7}	C/m	R_t	1.86	$M\Omega$

Table 2.6 Element values for the small signal electrical macromodel

VHDL 1076.1 also called VHDL-AMS (VHDL analog and mixed signal) is of considerable interest in order to create behavioral models based on analytical expressions including ordinary differential and algebraic equations. The lumped parameters models created using the behavioral system description may now be non-linear functions of efforts, follows or state variables and such models adequately describe the device behavior for small and large signals [47]. Figure 2.18 which represents a two port electromechanical transducer is repeated here again for clarity. As shown in this figure each terminal port has an *effort* variable and a *flow* variable, the product of which is a power. The *flow* variable is defined as the time derivative of the *state* variable. By convention, the *flow* variable is positive when entering a port and increasing the transducer energy [42].

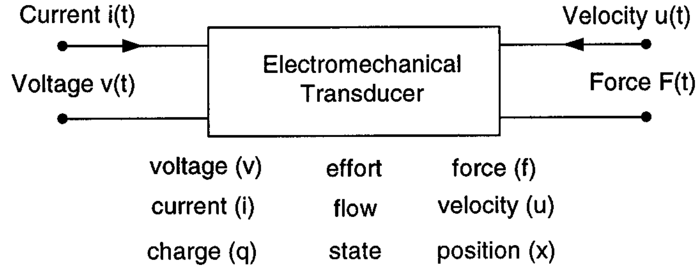

Fig. 2.35 Two port electromechanical transducer

The terms *across* and *through* are used in VHDL-AMS to describe the *effort* and *through* variables respectively and the physical domain in question is described as a *nature* [48]. There are two possible descriptions for the electromechanical analogy, direct or force-voltage and mobility or force-current analogies. Using the direct analogy the mechanical and electrical nets have dual topologies where the across variables are equated to through variables and conversely through variables are equated to across variables. As we have used this analogy in constructing the small-signal lumped-element electrical models, we will use the same analogy in behavioral modeling of the electrostatic transducer.

The large-signal behavioral model of the electrostatic transducer will be developed from the existing analytical expression for the internal energy in 2.49. In a conservative electromechanical transducer, the effort variable of each port can be determined by deriving the energy in the transducer with respect to the state variable of each port

$$v_t = \frac{\partial W_e}{\partial q_t} = \frac{q_t(d + x_t)}{\varepsilon_o W_r W_e} \tag{2.90}$$

$$f_t = \frac{\partial W_e}{\partial x_t} = \frac{q_t^2}{2\varepsilon_o W_r W_e} \tag{2.91}$$

where W_r and W_e are the width of the resonator beam and the drive electrode respectively. The flow variables for the electrical and mechanical ports, current and velocity, are the first derivates of the corresponding state variables

$$i_t = \dot{q}_t \text{ and } u_t = \dot{x}_t \tag{2.92}$$

Then the expressions in 2.90, 2.91, and 2.92 are directly used to link the effort and flow variables in the equation block of the VHDL-AMS model. The listing in figure 2.36 is the

VHD-AMS coding for the transverse electrostatic transducer between the drive electrode and the resonator beam.

```
LIBRARY IEEE;
LIBRARY DISCIPLINES;
USE IEEE.MATH_REAL.ALL;
USE DISCIPLINES.ELECTROMAGNETIC_SYSTEM.ALL;
USE DISCIPLINES.KINEMATIC_SYSTEM.ALL;
ENTITY transducer IS
    GENERIC (wr  : REAL := 8.0e-6;
             we : REAL  := 16.0e-6;
             d   : REAL :=  0.75e-6
             Vp :  REAL := 80.0);
    PORT (TERMINAL  t1,t2 : TRANSLATIONAL;
            TERMINAL e1,e2 : ELECTRICAL);
END ENTITY transducer;
ARCHITECTURE behav OF transducer IS
    QUANTITY f ACROSS u THROUGH t1 TO t2;
    QUANTITY v ACROSS i THROUGH e1 to e2;
    QUANTITY  q,x  : REAL;
    QUANTITY qo    : REAL;
    CONSTANT epi  : REAL := 8.85e-12;
BEGIN
qo == epi*wr*we/d*Vp;
x  == u'integ;
q  == i'integ+qo;
v == q*(d+x)/(epi*wr*we);
f == q*q/(2.0*epi*wr*we);
END ARCHITECTURE behave:
```

Fig. 2.36 Behavioral macromodel for the transverse electrostatic transducer

The transducer is defined as a two port entity with two electrical terminals (e1,e2) and two translational terminals (t1,t2). W_r, W_e, d, and V_p are the parameters of the 10MHz band-pass filter listed in table 2.5. The proposed large-signal electrical macromodel in figure 2.37 will be used as an input for a mixed-signal simulator to find the band-pass filters characteristics. The element values are listed in Table 2.6.

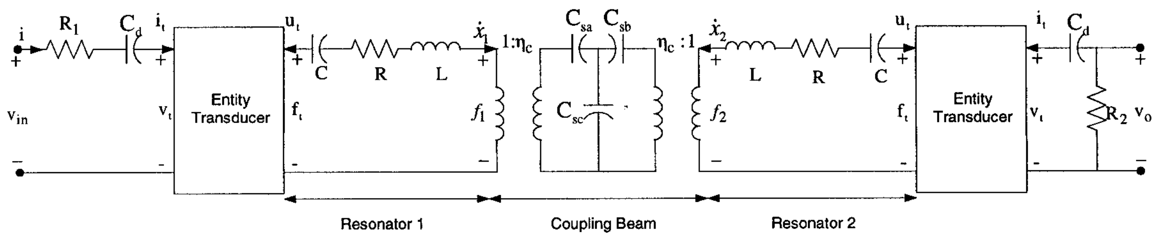

Fig. 2.37 Equivalent large-signal electrical macromodel

The modeling approaches presented before are based on analytical description of the structure using the differential and algebraic eqautions. For MEMS structures with complex geometries this approach is almost impossible, because of the lack of ability in theoretical description of the whole structure. In addition for the simple MEMS structures during the theoretical modeling the physical phenomena must be simplified to be expressed in an equation wich results in loss of accuray in the simulation reslts.

Finite element tools such as ANSYS have been successfully applied for the design of MEMS devices on the physical level of abstraction. These methods are very accurate to study complicated problems but in practice they are difficult to handle and too cumbersome for daily design tasks. Moreover if one tries to perform system simulations or wants to consider electronic circuitry and MEMS components at once, FEM methods are inappropriate [50]. Reduced order modeling is an approach to develop a simplified macromodel of MEMS components based on the FEM analysis results. The basic idea of ROM is to describe the deformation state of the structural part by a series of weighted modal shape functions [49] and the ultimate goal is to obtain an accurate black-box model of the MEMS device using behavioral description languages such as VHDL-AMS. Since all model information are extracted from 3D finite element simulations we are able to capture mechanical non-linearities and large-signal behaviour with the same order of accuracy. The theoretical background of reduced order modeling which is based on system matrix reduction process is explained in more detail in [51]. Here we will use the ANSYS/Multiphysics tool capabilities in reduced order modeling of the microelectromechanical filters and the simulation results will be compared with the results obtained using the previously defined macromodels.

The microelectromechanical filter is divided to the resonators and the coupling elements, and then reduced order models of the resonators along with the equivalent electrical circuits of the coupling elements, shown in figure 2.30, have been used to develop the final macromodel of the band-pass filter presented in figure 2.38. The first step in generating the reduced order model is to create a 3D finite element model of the resonator with appropriate structural and electrostatic physics environments. During this step the master nodes which represent the coupling beam attachment locations should be specified. The next step is to perform a static analysis followed by a modal analysis to

select the dominant modes, for the resonators in this work we have selected the first fundamental mode as the dominant mode. Then strain energy and capacitance-stroke functions are derived from a multiple FE structural-electrostatic simulations and finally a fitting procedure is performed to derive the polynomials describing the MEMS component. The reduced order models exported in VHDL-AMS describe the electrostatic structural interaction within the resonator and can be used in large-signal, non-linear analysis.

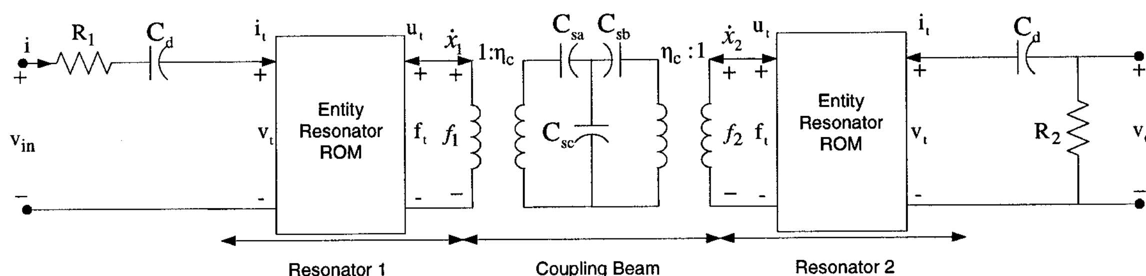

Fig. 2.38 Macromodel of the filter based on ROM

All the simulations have been done using AdvanceMS from Mentor Graphics, a mixed-signal simulator which can simulate a VHDL-AMS model containing SPICE netlist, a SPICE netlist containing VHDL-AMS behavioral models, or even a pure SPICE netlist.

The functionality of the generated macromodels can be proven by performing a harmonic analysis within the pass band frequency range to find the filter characteristics. The frequency response of the microelectromechanical filter with parameters listed in Table 2.5, is plotted in figure 2.39. Three different macromodels, small-signal, large-signal, and ROM have been used during the simulation and the results are compared with the ones obtained with FEM analysis in Table 2.7.

Model	Center Frequency	Insertion Loss
Small-Signal	9.6835 MHz (0.603%)	6.6326 dB
Large-Signal	9.7145 MHz (0.284%)	6.5691 dB
ROM	9.7426 MHz (0.004%)	3.5315 dB
FEM	9.7422 MHz	–

Table 2.7 10MHz filter characteristics using different macromodels and the error with respect to the FEM results

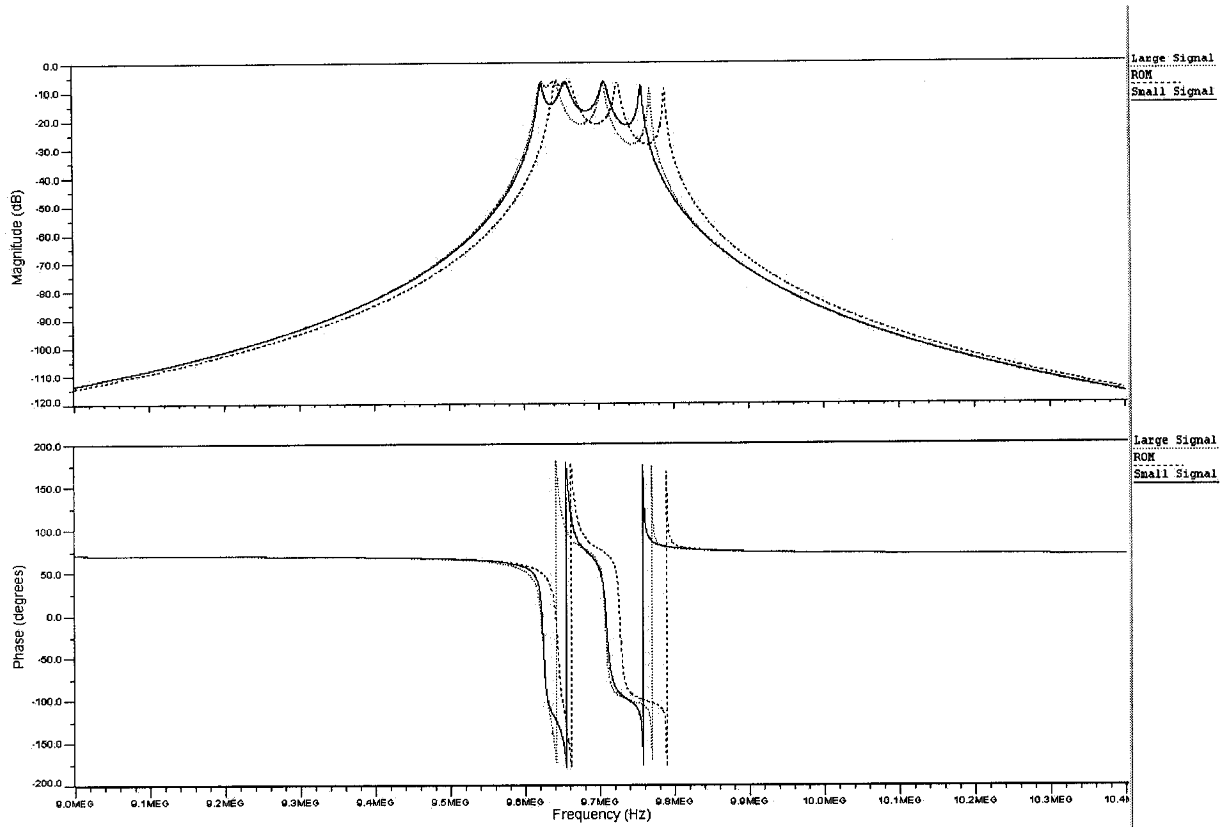

Fig. 2.39 Harmonic analysis of the band-pass filter using different macromodels

In order to demonstrate the effectiveness of the large-signal electrical macromodels and the reduced order models in large-signal non-linear modeling of the filter, Fourier analysis has been performed using two different voltage levels for the input signal. This kind of analysis is almost impossible using FEM and comparison has been made between the models themselves. The discrepancy between the small-signal and large-signal models will be more evident at a frequency far from the center frequency. For the first Fourier analysis the input signal frequency is adopted to 8MHz and the voltage amplitude is 30mV (small signal) and three harmonics have been used. For the second analysis the voltage amplitude is 5V (large signal) and the input frequency is the same as the first simulation. For small signal analysis all the models give almost the same result, but for higher input voltage levels the small-signal model can not represent the nonlinear behavior of the device. As shown in Table 2.8, for large signal analysis using the ROM and large-signal macromodels the second Fourier naormalized component is around 16% which is only 7% using the small-signal models.

	Small Signal (30mv)			Large Signal (5v)		
Harmonic #	**Small**	**Large**	**ROM**	**Small**	**Large**	**ROM**
1 (9.6562MHz)	100%	100%	100%	100%	100%	100%
2 (19.312MHz)	4.06%	6.66%	5.43%	7.00%	16.3%	15.4%
3 (28.969MHz)	2.16%	4.63%	3.98%	5.59%	9.41%	8.74%

Table 2.8 Fourier analysis results

Moreover the generated macromodels can be used to examine the effect of the quality factor, number of resonators, and the coupling configuration in the filter frequency response. Figure 2.40 shows the difference between the closed ring and open ring coupling configurations in the amplitude response of the 10MHz band-pass filter. By arranging the MEMS resonators in a closed ring, where the last resonator is coupled to the first resonator, the asymmetry in the amplitude response has been resolved as depicted in this figure. Figure 2.41 shows the frequency response for three different values of filter quality factor Q_{fltr} by adjusting the termination resistors R_t. Lower quality factor results in higher band-width for the resonators and a flatter frequency response for the filter as explained in section 2.2.7.

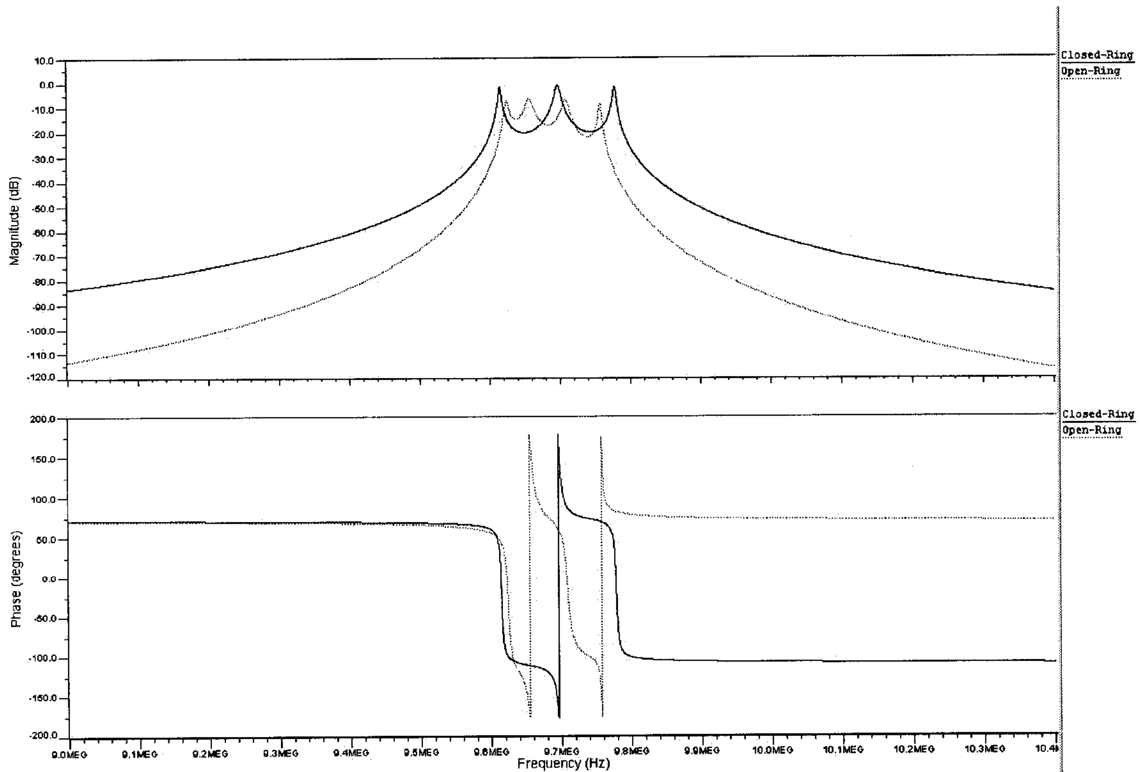

Fig. 2.40 Frequency response of the closed-ring and open-ring configurations

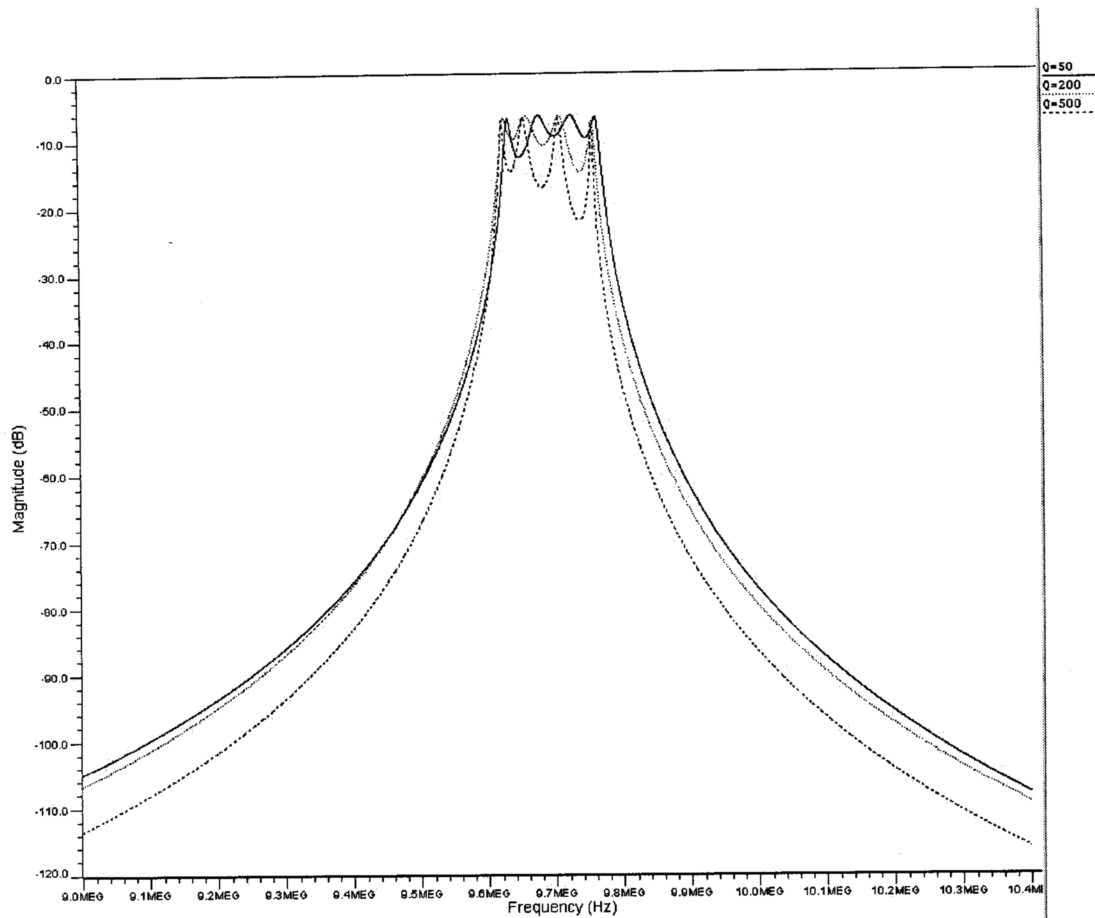

Fig. 2.41 Frequency response for different quality factors

2.3 MEMS Variable Capacitors for Filtering Applications

The microelectromechanical filters discussed in previous sections are suitable for VHF frequency range and for UHF and higher frequency ranges the conventional filters based on lumped element capacitors, varactor diodes, and inductors are preferred. The recent advances in micromachining technology have been used in constructing on-chip tunable capacitors which can be used for RF tunable filtering applications. The benefits of using MEMS variable capacitors instead of the conventional varactor diodes are lower loss, higher Q-factor, lower power consumption, and linear characteristics at high frequencies.

2.3.1 Filter Topologies Based on MEMS Capacitors

There are two different topologies for filters constructed using the variable MEMS capacitors; distributed-element type and lumped-element type. Distributed-element type

filters employ transmission lines and the center frequency is controlled by means of a MEMS variable capacitor attached at the end of the transmission line while in lumped-element filters the MEMS variable capacitors are combined with fixed spiral inductors. These two different filter topologies are depicted in figure 2.42.

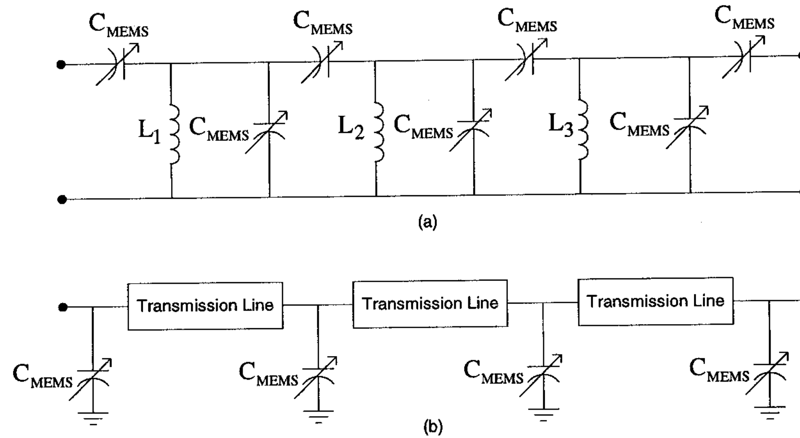

Fig. 2.42 Lumped-element (a) and distributed-element (b) filter topologies based on MEMS capacitors

Typically filters are tuned by changing both inductors and capacitors so one of the challenges in designing tunable filters with MEMS variable capacitors is to find a method to change the center frequency without the need to tune the inductors. Once we design a filter for a specified center frequency and bandwidth, the filter can be scaled to any desired center frequency and impedance using appropriate scaling techniques as explained in section 2.1.5. A conventional band-pass filter topology is shown in figure 2.43(a) For this topology we have used both series and parallel LC resonators and in order to change the center frequency for this filter while maintaining a given bandwidth, both the shunt capacitors and series inductors within each of the series and shunt resonators should be tuned. And it means that a tunable filter needs more than only tunable capacitors, but variable inductors as well. One of the common techniques used in designing microwave band-pass filters is to use impedance inverters to convert series resonators to shunt resonators. This is the key ingredient to design RF MEMS filters, which are tuned only by varying the capacitors in the parallel resonators. A band-pass filter utilizing this technique is shown in figure 2.43(b) [52].

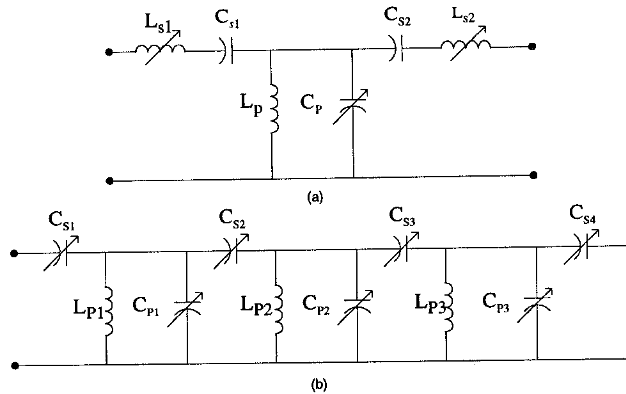

Fig. 2.43 Conventional lumped-element band-pass filter (a) and the one using impedance inverters (b)

2.3.2 MEMS Variable Capacitors

As mentioned in section 1.1.3 there are two different MEMS variable capacitor configurations; parallel-plate and comb-finger capacitors and also there are two actuation mechanisms for the tuning of these MEMS components; thermal and electrostatic. In this section we will introduce the principles of operation for the parallel-plate electrostatic MEMS capacitors and then in chapter 3 we will discuss the design and fabrication in more detail. Figure 2.44 shows a schematic view of an electrostatic parallel-plate capacitor. The top plate of the capacitor is suspended by a spring with a stiffness of k and the bottom plate is fixed on the substrate.

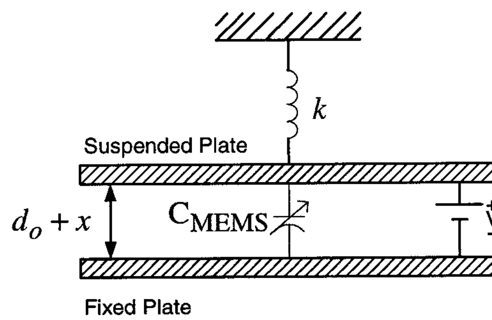

Fig. 2.44 Schematic view of parallel-plate MEMS capacitor

When a bias voltage is applied between the plates, the top plate is attracted towards the bottom plate and under equilibrium condition the relation between the electrostatic and

mechanical forces can be written as [53]

$$kx = \frac{\varepsilon A V^2}{2(d_o - x)^2} \qquad 2.93$$

where ε is the dielectric constant of air, A is the area of the capacitor plates, and d_o is the initial separation between the capacitor plates. The capacitance between the plates can be obtained as follows

$$C(V) = \frac{\varepsilon A}{d_o - x(V)} \qquad 2.94$$

and $x(V)$ is obtained using equation 2.93. The electrostatic parallel-plate capacitor exhibits an important behavior which is called pull-in effect. If we consider the stability of the equilibrium which exists between the electrostatic force pulling the plate down and the spring force pulling the spring up, the effective force on the beam at voltage V and gap d_o, is

$$F_{net} = \frac{\varepsilon A V^2}{2(d_o - x)^2} - kx \qquad 2.95$$

At a point of equilibrium, F_{net} is zero. With a small perturbation of the gap to $x + \delta x$, we can write [53]

$$\delta F_{net} = \left.\frac{\partial F_{net}}{\partial x}\right|_{V=cte} \delta x \qquad 2.96$$

If $\partial F_{net}.\partial x > 0$ then we are in an unstable equilibrium point, because a small increase ∂x creates a force tending to increase it further. We can evaluate ∂F_{net} using equation 2.95 as

$$\partial F_{net} = \left(\frac{\varepsilon A V^2}{(d_o - x)^3} - k \right) \delta x \qquad 2.97$$

For a stable equilibrium point, the expression in parenthesis must be negative, which means that

$$k > \frac{\varepsilon A V^2}{(d_o - x)^3} \qquad 2.98$$

Since the equilibrium gap decreases with increasing voltage, there will be a specific voltage at which the stability of the equilibrium is lost. This is called the pull-in voltage, denoted by V_{PI}. Using 2.98 and 2.93 it is readily shown that the pull-in occurs at

$$x_{PI} = \frac{1}{3} d_0 \qquad 2.99$$

And at this value of gap, the equilibrium voltage is

$$V_{PI} = \sqrt{\frac{8kd_0^3}{27\varepsilon A}} \qquad 2.100$$

By normalizing the voltage to the pull-in voltage, and using the normalized displacement of the top plate from its equilibrium position we can write

$$v = \frac{V}{V_{PI}} \qquad 2.101$$

$$\xi = \frac{x}{d_0}$$

And using these variables, the condition for equilibrium is

$$\frac{4}{27} \frac{v^2}{(1-\xi)^2} = \xi \qquad 2.102$$

Figure 2.45 shows the two sides of this equation plotted simultaneously for the specific value $v = 0.8$. There are two intersections, meaning two equilibrium points. However, only one of them is stable. As the voltage increased, the dashed curve moves in the direction of the arrow, and the two equilibrium points move toward each other, exactly merging when $\xi = \frac{1}{3}$ and $v = 1$. For normalized voltages greater than 1, the two curves never intersect and there is no stable equilibrium.

$$y_1 = \xi \, , \; y_2 = \frac{4}{27}\frac{v^2}{(1-\xi)^2}$$

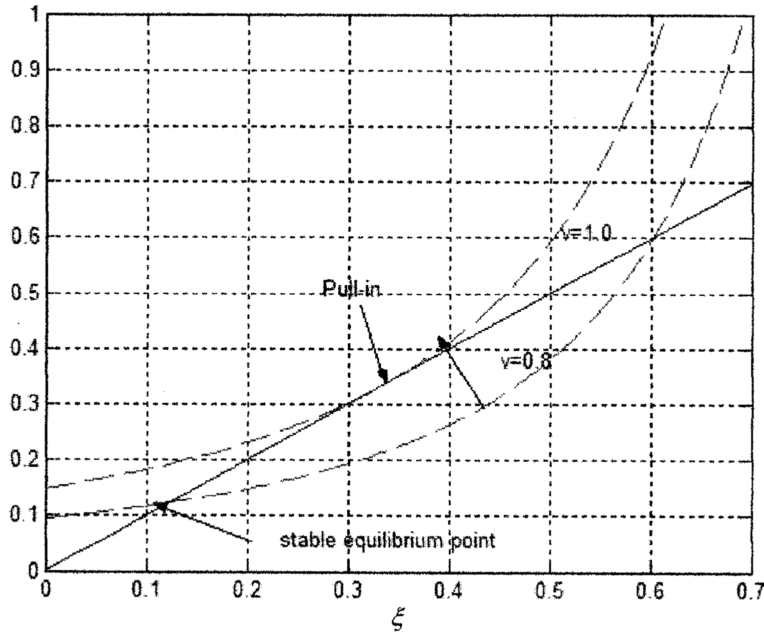

Fig. 2.45 Pull-in voltage and equilibrium points for the parallel-plate capacitor

In this work, we have designed and fabricated different parallel-plate MEMS variable capacitors with electrostatic actuation mechanism. The fabricated MEMS capacitors suffer from low Q-factor at RF frequency range due to the stray capacitance between the bottom plate and the silicon substrate which produces high insertion losses. However Flip-Chip technology [28] can be used to transfer the fabricated devices to another alumina substrate with an extra fabrication cost. Our work describes a novel approach based on wet etching of Silicon substrate with TMAH that improves the Q-factor of the fabricated MEMS variable capacitors at RF frequency range. The details of fabrication process and design will be discussed in chapter 3.

Chapter 3
Design and Fabrication

In this chapter, we focus on the design, fabrication, and post-processing of the proposed devices. We use the PolyMUMPs process technology to fabricate the microelectromechanical filters. For the variable MEMS capacitors another standard CMOS technology has been used which enables the integration of MEMS devices besides the electronic circuitry. All the designs presented here are based on the theory developed in the previous chapter. First the design of MEMS resonators will be discussed, these resonators are categorized in three different classes; cantilever beam, clamped-clamped beam, and disk flexural-mode resonators. Then the mechanical coupling between these resonators will be employed in designing microelectromechanical band-pass filters. The last section presents the design, fabrication, and post-processing of the variable MEMS capacitors which can be used in RF tunable filters.

3.1 Flexural-Mode Clamped-Clamped Beam Resonator

The flexural clamped-clamped beam micromechanical resonator consists of a poly-silicon beam clamped at both ends through the anchors and a drive electrode as shown in figure 3.1 below.

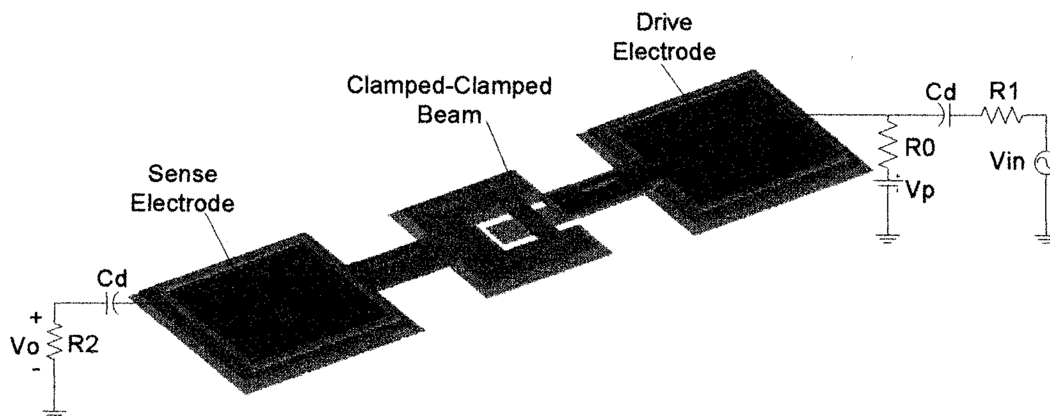

Fig. 3.1 Clamped-Clamped flexural beam resonator

The resonator beam and the bottom electrode which is located at the center of the beam are fabricated using the Poly1 and Poly0 poly-silicon layers respectively, therefore the capacitive gap between the resonator beam and the drive electrode is around 2μm however after fabrication and the HF release this gap will be slightly increased due to the minor etching of poly-silicon layers in HF. The MEMS resonator along with the biasing, drive and sensing circuitry as shown in figure 3.1 can be used as a frequency selection stage. Based on the theory of vibration, the transverse vibration of the resonator beam, perpendicular to the substrate, leads to a form of boundary-value problem, a partial differential equation of second order in the time domain as defined in equation 2.13. The fundamental modal frequency of the beam depends on the geometries of the beam and the material properties of the constructing layers as obtained by equation 2.25. The resonator should be DC biased and the input signal V_{in} is coupled through a coupling capacitor to the drive electrode. The applied input signal creates an electrostatic force given by [9]

$$F_{elec} = V_P \frac{\partial C}{\partial y} V_{in} \qquad 3.1$$

where y is the vertical displacement and $\partial C / \partial y$ is the change in electrode to resonator capacitance per unit displacement of resonator beam. If the frequency of the input signal is close to one of the modal resonance frequencies of the resonator beam then the electrical energy will be transferred to the mechanical vibration of the beam. The vibration of the beam generates a DC biased time varying capacitor between the sense electrode and ground, which results in an output current given by [9]

$$i_o = V_p \frac{\partial C}{\partial y} \frac{\partial y}{\partial t} \qquad 3.2$$

The current i_o is then directed to the output termination resistor R_2 which converts the output current to an electrical output signal. In effect, this device takes an electrical input signal, converts it to a mechanical signal, processes it in the mechanical domain, then converts the resulting signal to an electrical output signal, ready for further processing by subsequent electronic stages [9].

The modal resonance frequencies of the clamped-clamped beam resonator, in figure 3.1, is obtained using equation 2.25 with $k_n l$ values listed in Table 2.2. The first modal resonance frequency is given by

$$f_1 = 1.0291\sqrt{\frac{E}{\rho}}\frac{t}{L_r^2} \qquad 3.3$$

E, ρ, and t are the Young's modulus, density, and the thickness of the structural layer, Poly1, which depend on the process technology. Table 3.1 shows the material properties and thickness of different layers in the PolyMUMPs technology [25, 54].

Film	Thickness (A°)			Young's Modulus (GPa)			Poisson's Ratio			Resistance (Ω/□)			Density (Kg/m^3)
	Min	Typ	Max	Min	Typ	Max	Min	Typ	Max	Min	Typ	Max	
Nitride	5300	6000	6700	230		265	0.24			N/A			3100
Poly0	4700	5000	5300	62	163	202	0.22	0.22	0.278	15	30	45	2330
Oxide1	17500	20000	22500	73			0.17			N/A			2206
Poly1	18500	20000	21500	62	163	202	0.22	0.22	0.278	1	10	20	2330
Oxide2	6700	7500	8300	73			0.17			N/A			2206
Poly2	14000	15000	16000	62	163	202	0.22	0.22	0.278	10	20	30	2330
Metal	4600	5200	5800	80			0.44			0.05	0.06	0.07	19280

Table 3.1 Material properties for different layers in PolyMUMPs

The only design parameter is the length of the resonator beam l which defines the modal resonance frequencies. The finite element method (FEM) analysis has been performed using ANSYS. For this purpose the layout file along with a technology file describing the whole fabrication process have been imported into the CAD MEMSPro software and then based on these two files a 3D model of the final device can be extracted. The extracted 3D model will be directly imported in ANSYS. The procedure described above results in the speed up of modeling and simulation by automating the laborious task of generating the 3D model of MEMS devices with complex geometries.

To determine the modal frequencies of the micromechanical resonator, we have used the 10-node tetrahedral structural element, SOLID92, and then the boundary conditions have been applied in such a way to clamp both ends of the resonator beam. The FEM modal analysis results have been used to verify the calculated modal frequencies obtained using equation 2.25.

As shown in figure 3.2 two different 3D models have been used for the FEM analysis of the same MEMS resonator, the first model is the one imported from MEMSPro and has exactly the same geometry as the real fabricated device, and the other structure is just a simple beam fixed at both ends. The reason to use two different structures for the FEM simulation is that we obtained equation 2.25 for the modal frequency of a simple beam as shown in figure 3.2(b), but the real device shown in figure 3.2(a) deviates from this simple model and using the classical mechanical methods described before it is almost impossible to find a mathematical equation for the modal resonance frequency of the fabricated MEMS resonator with complex geometries at the anchor regions.

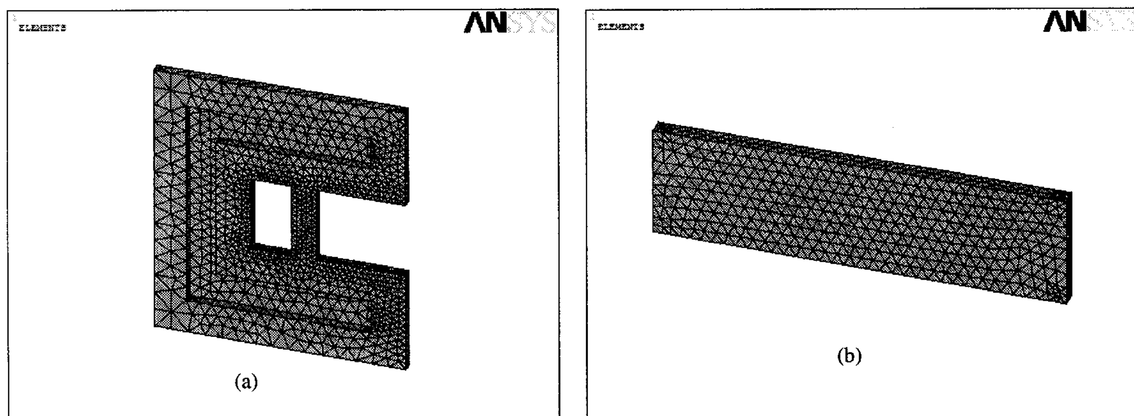

Fig. 3.2 Two different models used for the modal analysis of the resonator

Table 3.2 presents the simulation results for these two different 3D models along with the theoretical results. The theoretical model deviates from the FEM simulation results for both the fabricated device and a simple beam and the deviation for the higher modes is larger than the fundamental mode. While the simple clamped-clamped beam in figure 3.2(b) should follow the theoretical results using equation 2.25, still we can see a minor divergence between the theoretical results and FEM simulation results, this difference can be explained using the Timoshenko beam theory as discussed in section 2.2.3.

Mode Number	Theoretical	FEM (Fig. 3.2.a)	FEM (Fig. 3.2.b)	Deviation (Fig. 3.2.a)	Deviation (Fig. 3.2.b)
1st mode	10.759 MHz	9.6957	10.686	11.42%	0.57%
2nd mode	29.623 MHz	25.570	28.880	13.68%	2.51%
3rd mode	58.079 MHz	49.270	55.244	15.17%	4.88%
4th mode	95.997 MHz	85.791	88.698	10.63%	7.60%

Table 3.2 Modal frequencies obtained theoretically and using FEM simulation results

The fundamental frequency of MEMS resonator versus the beam length is plotted in figure 3.3 based on FEM simulation results and the classical and Timoshenko beam theories. For this resonator the beam width $W=8\mu m$ and the beam thickness $t=2\mu m$. The beam length varies between $9.98\ \mu m$ and $40\ \mu m$. As shown in this figure for the resonators with a length bigger than $25\,\mu m$, the simulation results match with theory, however for short beams, the Timoshenko beam gives a resonant frequency more closer to the one obtained by FEM analysis.

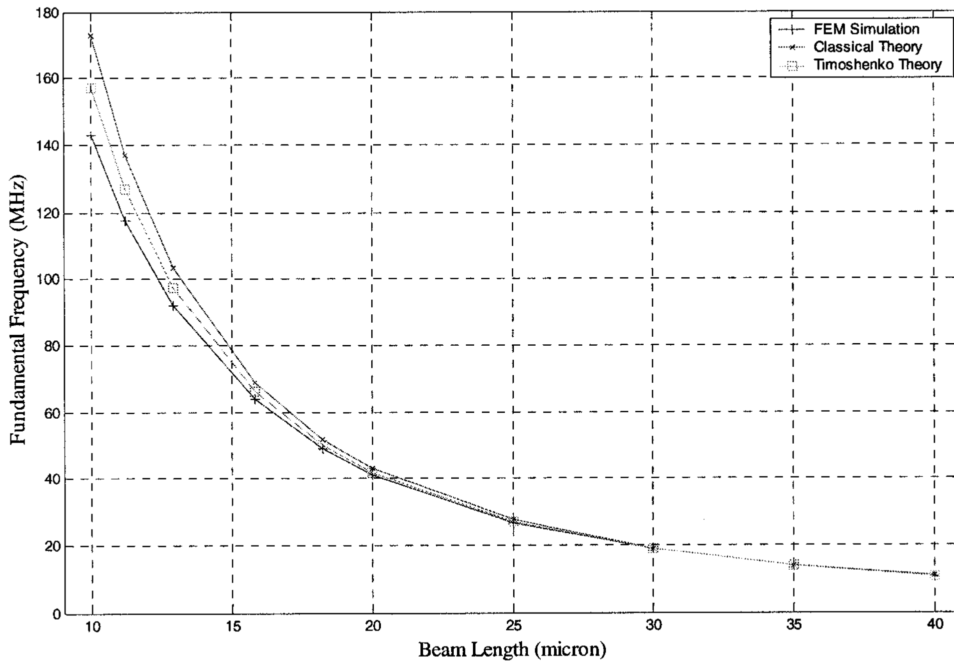

Fig. 3.3 Fundamental modal frequency versus beam length

The Scanning Electron Microscopy (SEM) image of a clamped-clamped 10MHz MEMS resonator fabricated using the PolyMUMPs technology is presented in figure 3.4. The dimensions and other design specifications of the resonator are listed in Table 3.3.

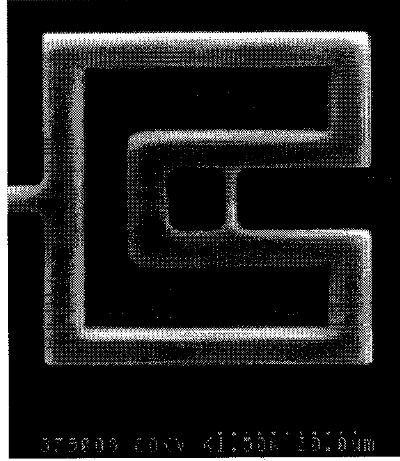

Fig. 3.4 SEM picture of the 10MHz clamped-clamped MEMS resonator

Parameter	Value	Units	Parameter	Value	Units
Beam Length, L_r	40	μm	Resonator Stiffness, k_r	2174	N/m
Beam Width, W_r	8	μm	Center Frequency, f	9.6562	MHz
Beam Thickness, h	2	μm	Resonator Band Width, Δf	698	Hz
Electrode Width, W_e	16	μm	Modification Factor, κ	0.9012	–
Electrode-to-Beam Gap, d_o	2.0	μm	Poisson's Ratio	0.225	–
Resonator Q	13834	–	Young's Modulus, E	163	GPa
Resonator Mass, m_r	5.9058×10^{-13}	Kg	Density of Polysilicon, ρ	2330	Kg/m^3
Damping Constant, C_r	2.5901×10^{-9}	Ns/m	DC Bias, V_P	80	V

Table 3.3 Design specifications and geometries of the clamped-clamped resonator

The design starts with determining the center frequency of the resonator, in order to model the effects of complex geometries in the beam structure, a modification factor κ is introduced in equation 3.3 and it can be rewritten as

$$f_1 = 1.0291\kappa\sqrt{\frac{E}{\rho}}\frac{t}{L_r^2} \qquad 3.4$$

For the resonator in Table 3.3, the center frequency is 9.6957MHz based on the FEM simulation results for the real structure imported from MEMSPro, and we have used a modification factor of $\kappa = 0.9012$. The electromechanical coupling between the drive

electrode and the beam results in lowering of the overall resonant frequency which is called stiffness softening effect. As explained in section 2.2.6 in equation 2.60 which is repeated here for more clarity, there is a spring with a negative stiffness $-k' = -\Gamma^2 / C_0 = -\varepsilon_0 A_e v_0^2 /(d + x_0)^3$,

$$F(v,x) = \frac{q_0}{d + x_0} v + \left(k - \frac{q_0^2}{\varepsilon_0 A_e (d + x_0)} \right) x = \frac{\varepsilon_0 A_e v_0}{(d + x_0)^2} v + \left(k - \frac{\varepsilon_0 A_e v_0^2}{(d + x_0)^3} \right) x \quad 3.5$$

This spring is a result of the electromechanical coupling and leads to the lowering of the overall resonance frequency of the resonator by increasing the DC bias voltage V_P or v_o. This can be used advantageously to implement filters with tunable center frequencies as indicated by [9]

$$f = f_1 \sqrt{1 - g(d, V_P)} \quad 3.6$$

g is a function of V_p, the bias voltage, and d, the gap between the drive electrode and the resoantor beam. The resonant frequency and hence the filter center frequency can be adjusted by varying g through the bias voltage.

$$g(d, V_p) = \frac{1}{k_r} V_p^2 \frac{\varepsilon_o W_r W_e}{d_o^3} \quad 3.7$$

For the resonator in this work the DC bias voltage is $V_P = 80V$ which results in lowering the center frequency to 9.6562MHz. For simulation purposes we will need an equivalent spring-mass-damper mechanical model. The equivalent mass at the center of the beam m_r can be found by 2.45 and 2.44

$$m_r(L_r / 2) = \frac{\rho t W_r \int_0^{L_r} [Y_{\text{mod}}(x')]^2 dx'}{[Y_{\text{mod}}(x = L_r / 2)]^2} \quad 3.8$$

where for a clamped-clamped beam [8]

$$Y_{\text{mod}}(x) = 1.01781(\cosh kx - \cos kx) + (\sin kx - \sinh kx) \text{ and } k = 4.73 / L_r \quad 3.9$$

For small values of air damping ratio ζ defined by 3.11 the quality factor of the resonator will be obtained by

$$Q \cong \frac{1}{2\zeta} \sqrt{1 - g(d, V_p)} \quad 3.10$$

$$\zeta = \frac{\alpha \mu L_r^2}{W_r h^2 (4.73)^2} \sqrt{\frac{3}{E\rho}} \qquad 3.11$$

α is a scaling factor which for a rectangular beam is equal to 10, and $\mu = 1.81\times10^{-5}$ is the dynamic viscosity of air [55]. For the resonator stiffness k_r and damping constant C_r, we have used the results in section 2.2.5.

Figure 3.5 presents the frequency response of the MEMS resonator with the input and output configurations as shown in figure 3.1. The harmonic simulation has been performed by SPICE and using the equivalent electrical macromodels based on the element values listed in Table 3.3. The resonance frequency obtained by this simulation is 9.657MHz.

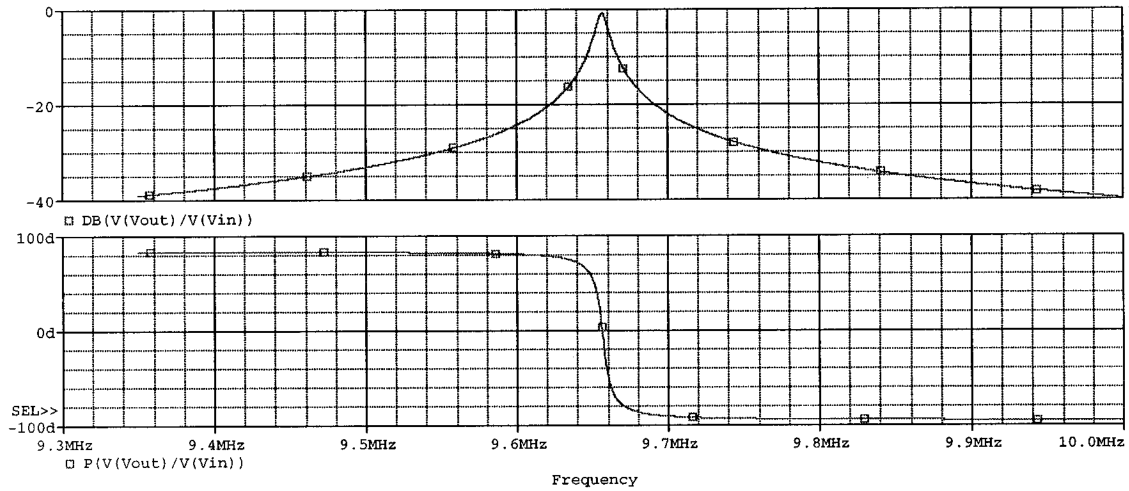

Fig. 3.5 Frequency response of the 10MHz clamped-clamped MEMS resonator

The applied DC bias voltage V_P has a superior effect on the transduction factor obtained by equation 2.63. By increasing the DC bias voltage the transduction factor will be increased which means that more electrical power will be transferred to the mechanical energy and the beam vibrates with larger amplitude. However as discussed in section 2.3.2 because of the pull-in effect we can not increase V_P beyond the pull-in voltage. For this reason FEM analysis has been performed to find the safety region for the applied DC bias voltage. Figure 3.6 shows the deformation of the resonator beam under

$V_P = 80V$ as shown in this figure, the maximum deflection at the center of the beam is just $4\times10^{-4}\mu m$ far less than the pull-in deformation which is $2/3\mu m$.

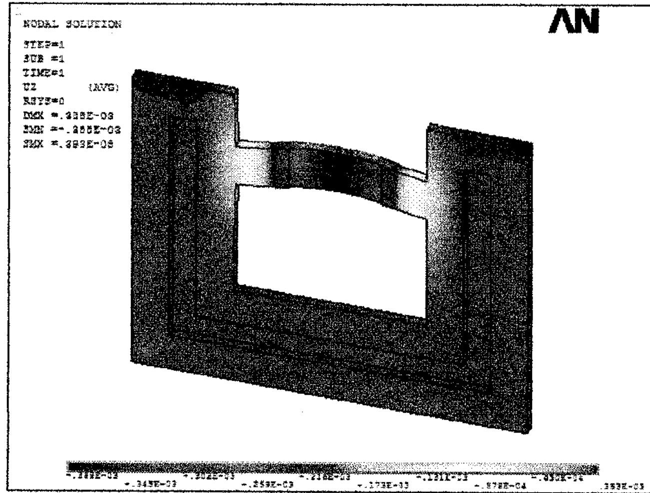

Fig. 3.6 Beam deformation, because of the applied DC bias voltage $V_P = 80V$

3.2 Flexural-Mode Cantilever Beam Resonator

Figure 3.7 presents the schematic diagram of the flexural-mode cantilever beam resonator which has been fabricated using the PolyMUMPs surface micromachining fabrication technology. The main advantage of this resonator compared to the clamped-clamped resonator, is its lower stiffness and as a result it needs a lower DC bias voltage.

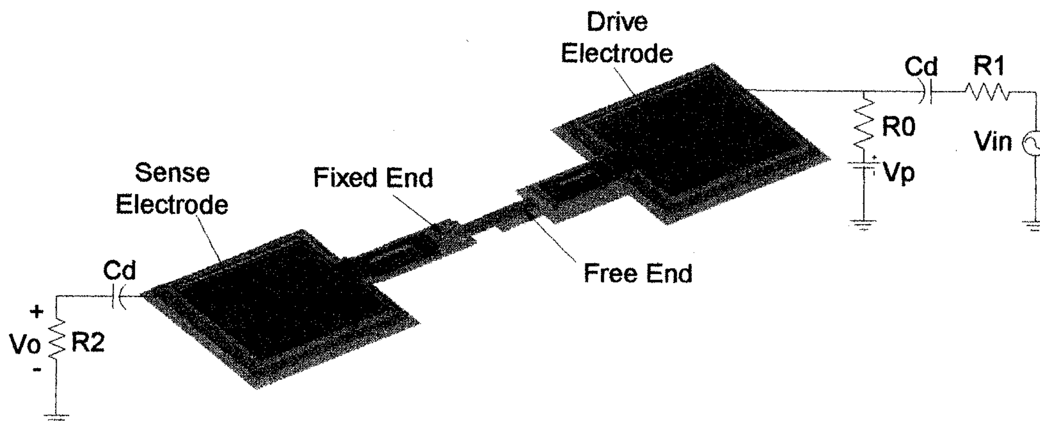

Fig. 3.7 Flexural-mode cantilever beam resonator

As shown in figure 3.7 the drive electrode is made of Poly0 layer and the cantilever beam is fabricated using the first structural layer, Poly1, with a total thickness of $2\,\mu m$ and the air gap between the drive electrode and the resonator beam is $2\,\mu m$.

The modal resonance frequencies of the cantilever beam resonator are obtained using equation 2.25 with $k_n l$ values listed in Table 2.2. The first modal resonance frequency is given by

$$f_1 = 0.1617\sqrt{\frac{E}{\rho}}\frac{t}{L_r^2} \qquad 3.12$$

Compared to the resonance frequency of the clamped-clamped beam given in equation 3.3, a cantilever beam resonator with the same beam length has a lower resonance frequency. Figure 3.8 shows the first two transverse modal shapes of the cantilever beam resonator.

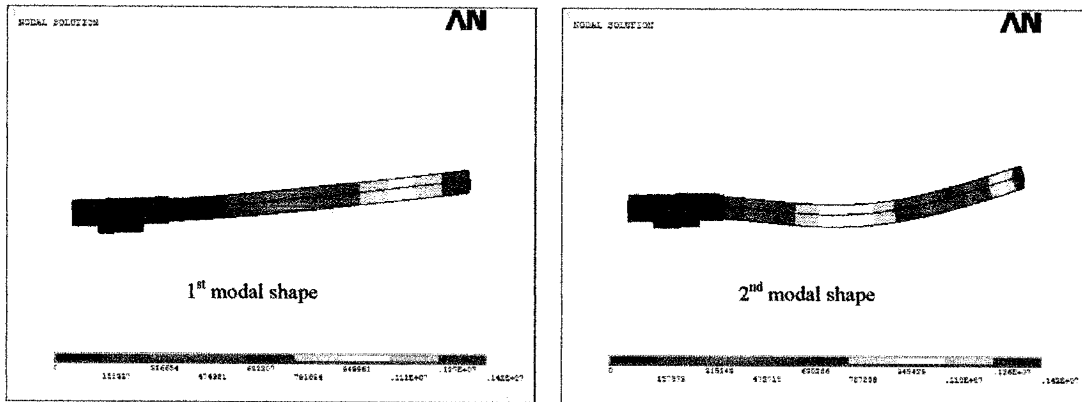

Fig. 3.8 Transverse modal shapes of the cantilever beam resonator

We are following the same design procedure as explained before for the clamped-clamped beam resonator. The beam length is L_r=40μm and using equation 3.12, the first modal resonance frequency occurs at f_1=1.6906MHz. However the FEM analysis gives a resonance frequency of f_1=1.5901MHz due to the fact that the real structure deviates from the simple classical model used in determining equation 3.12. The real resonance frequency will be decreased further because of the softening effect according to equation

3.6. For this resonator the applied DC bias voltage is $V_P = 60V$ which results in an overall resonance frequency of $f = 1.5888MHz$.

The design specifications of the cantilever beam resonator are listed in Table 3.4, based on the element values listed in this table, the equivalent electrical model has been used in harmonic analysis using SPICE to find the frequency response of the resonator presented in figure 3.9. As shown in this figure the simulated resonance frequency is 1.5901MHz and well matches with the design specifications in Table 3.4.

Parameter	**Value**	**Units**	**Parameter**	**Value**	**Units**
Beam Length, L_r	40	μm	Resonator Stiffness, k_r	322.81	N/m
Beam Width, W_r	8	μm	Center Frequency, f	1.5888	MHz
Beam Thickness, h	2	μm	Resonator Band Width, Δf	114	Hz
Electrode Width, W_e	16	μm	Modification Factor, κ	0.9406	–
Electrode-to-Beam Gap, d_o	2.0	μm	Poisson's Ratio	0.225	–
Resonator Q	13889	–	Young's Modulus, E	163	GPa
Resonator Mass, m_r	3.234×10^{-12}	Kg	Density of Polysilicon, ρ	2330	Kg/m^3
Damping Constant, C_r	2.3244×10^{-9}	Ns/m	DC Bias, V_p	60	V

Table 3.4 Design specifications and geometries of the Cantilever MEMS resonator

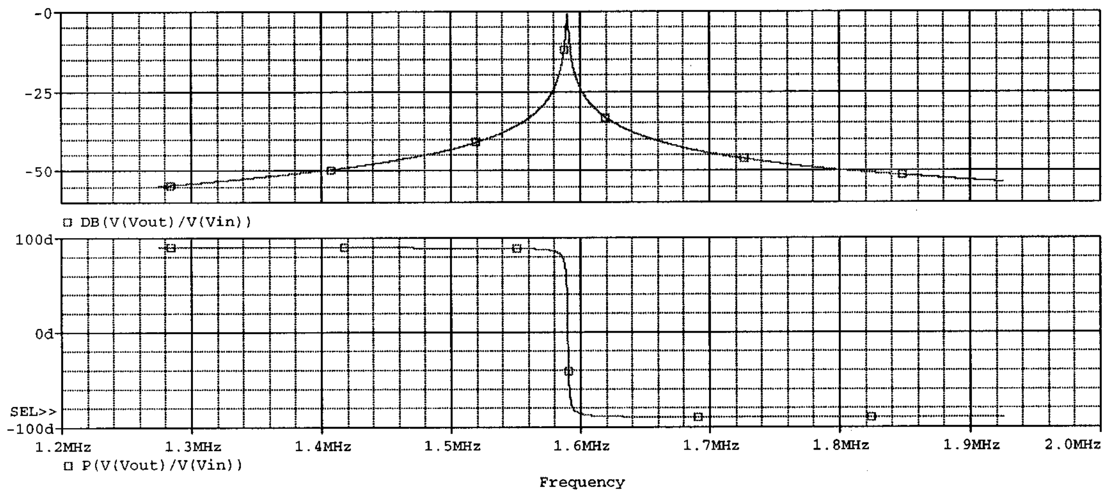

Fig. 3.9 Frequency response of the cantilever MEMS resonator

3.3 Flexural-Mode Disk Resonator

A schematic diagram presenting the flexural-mode disk resonator is shown in figure 3.10. The main advantage of this resonator compared to the discussed beam resonators, is its higher resonance frequency obtained by equation 2.40 which depends on the disk diameter. The drive electrode is made of Poly0 and the disk is fabricated using the first structural poly layer, as a result the air gap is $2\mu m$.

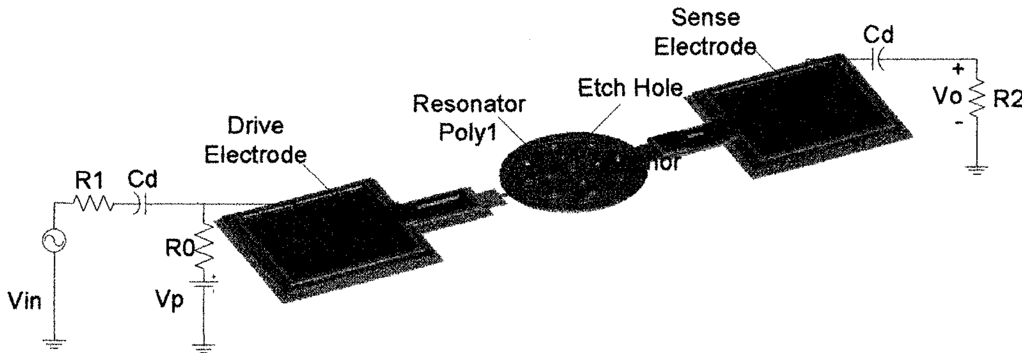

Fig. 3.10 Flexural-Mode disk resonator

The diameter of the designed disk resonator is $d = 80\mu m$ and the fundamental resonance frequency, using equation 2.40, occurs at $f_1 = 4.3486MHz$. However the FEM modal analysis gives a resonance frequency of $f_1 = 5.0251MHz$. By applying a DC bias voltage $V_P = 80V$ the maximum deformation using the FEM analysis is obtained to be just $14 \times 10^{-3}\mu m$ as shown in figure 3.11. As a result this DC bias voltage can be safely applied to the device without resulting in pull-in effect.

Besides the higher resonance frequency for the disk resonator another advantage of this resonator compared to the beam resonators is its large transduction factor Γ obtained by equation 2.63 which is repeated here

$$\Gamma = \frac{\varepsilon_0 A_e V_P}{(d + x_0)^2} \qquad 3.13$$

The effective area of the electrostatic transducer A_e for this resonator is larger than the beam resonators and by applying the same DC bias voltage more electrical energy will be transferred to the mechanical domain which in its turn results in stronger signal at the

output port. Table 3.5 presents the geometries and design parameters of the flexural-mode disk resonator and its amplitude response is depicted in figure 3.12. The quality factor of the resonator strongly depends on the testing conditions and the ambient pressure, for the quality factor we have used the numerical results presented in [56].

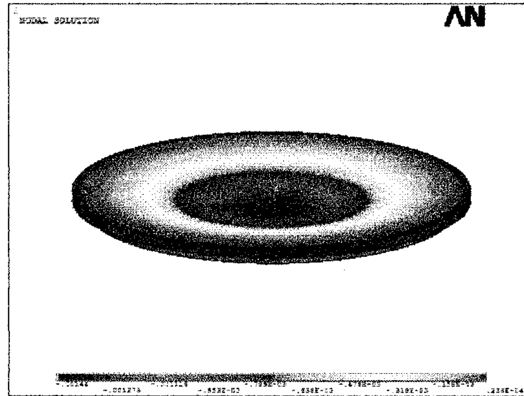

Fig. 3.11 Deformation of the disk resonator under $V_P = 80V$

Parameter	Value	Units	Parameter	Value	Units
Disk Diameter, d	80	μm	Resonator Stiffness, k_r	34818	N/m
Thickness, h	2	μm	Center Frequency, f	5.0251	MHz
Electrode Diameter, d_e	35	μm	Modification Factor, κ	1.1556	_
Electrode-to-Disk Gap, d_o	2.0	μm	Poisson's Ratio	0.225	_
Resonator Q	856	_	Young's Modulus, E	163	GPa
Resonator Mass, m_r	3.4927×10^{-11}	Kg	Density of Polysilicon, ρ	2330	Kg/m^3
Damping Constant, C_r	1.2883×10^{-6}	Ns/m	DC Bias, V_p	80	V

Table 3.5 Design specifications and geometries of the Disk resonator

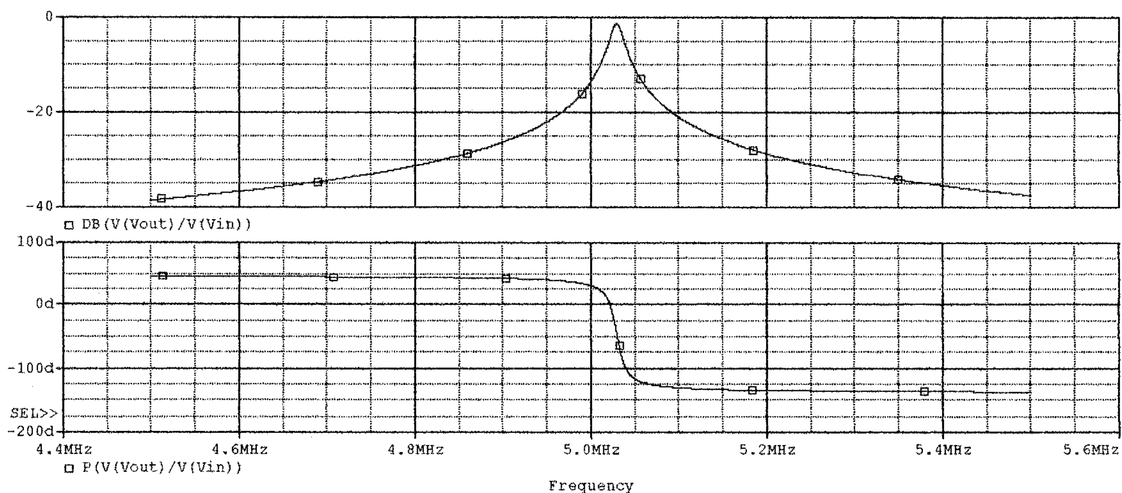

Fig. 3.12 Frequency response of the disk resonator

3.4 Microelectromechanical Band-Pass Filter

The microelectromechanical band-pass filters consist of flexural-mode clamped-clamped beam resonators, mechanically coupled to each other. Figure 3.13 presents a schematic view of a filter consisting of four resonators coupled in a close ring configuration. The close-ring configuration results in symmetric frequency response as discussed in section 2.2.7. The design procedure for the four-resonator filter of this work can be itemized as follows: 1) design and establish the MEMS resonator prototype to be used, choosing necessary geometries for the needed frequency 2) selecting a suitable value of coupling beam width and design coupling beams which corresponds to a quarter-wavelength of the filter center frequency 3) determine the coupling location on the resonators corresponding to the filter bandwidth of interest 4) generate a complete equivalent electrical circuit of the overall filter and verify the design using a circuit simulator such as SPICE.

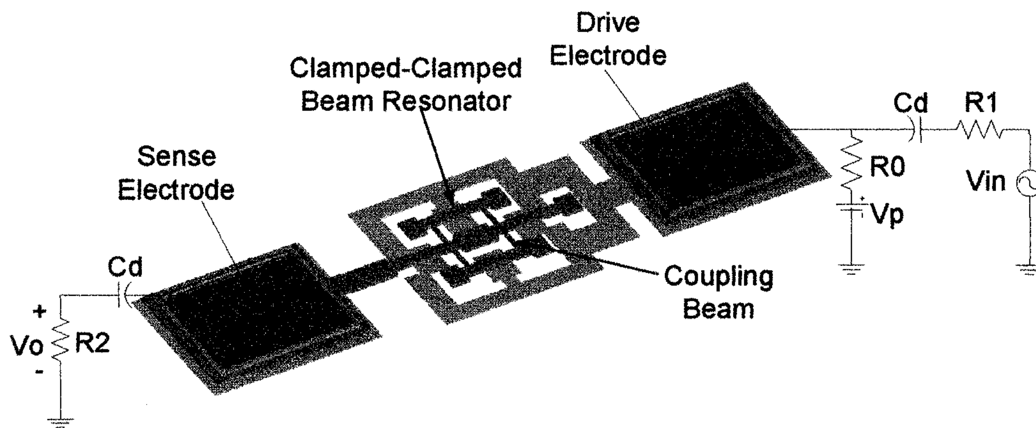

Fig. 3.13 Microelectromechanical band-pass filter

The clamped-clamped beam resonators are identical and have the same design specifications listed in Table 3.3. The center frequency of this filter depends on the resonance frequency of the constituent resonators which is 9.6562MHz. If each resonator is designed to have the same resonance frequency, then the pass band of the overall filter will be centered around this frequency. The coupling elements act to effectively pull the resonator frequencies apart, creating four closely spaced resonance modes that constitute the filter pass band.

The design of the coupling beam is based on the theory explained in section 2.2.8. The coupling beam is designed such a way that the beam corresponds to a quarter wavelength at the filter center frequency. In order to achieve this condition, equation 2.85 has been numerically solved

$$H_6 = \sinh\alpha\cos\alpha + \cosh\alpha\sin\alpha = 0: \quad \alpha_1 = 2.3650 \qquad 3.14$$

Then using equation 2.83 and setting $W_s = 2\mu m$ (coupling beam width) and $h = 2\mu m$ (coupling beam thickness), the required length of the coupling beam could be found

$$\alpha = L_s(\rho W_s h\omega^2 /(EI_s))^{0.25} = 0: \quad L_s = 17.26\mu m \qquad 3.15$$

The coupling beam location affects the quality factor of the band-pass filter obtained by equation 2.89. For the filter in this work, using the results in figure 2.30, the coupling location is selected to be close to the anchors at $x/L_r = 0.125$ corresponding to a normalized velocity of 0.2. This insures both high quality factor of the final filter and the design rule constraints by the fabrication process technology.

To operate this filter, a DC bias voltage V_P is applied to the drive electrode and then an ac input signal V_{in} is applied through resistor R_1 to the same drive electrode. There is also another terminating resistor R_2 at the output port which converts the current i_{out} to an output voltage. Based on equation 2.78, in order to flatten the pass band between the peaks, the quality factor of the constituent resonators must be reduced. Termination resistors R_1 and R_2 serve this function. The required value of the termination resistors for a band-pass filter with center frequency ω_o is given by [9]

$$R_i = \frac{k_r}{\omega_o q_i Q_{fltr} \Gamma^2} \qquad 3.16$$

where $Q_{fltr} = \omega_o / \Delta\omega$ and q_i is a normalized q parameter obtained from a filter cook-book. Table 3.6 presents the geometries, design specifications, and other parameters for the 10MHz band-pass filter, resonators, and the coupling beam elements. Based on the parameters in Table 3.6, an equivalent electrical circuit has been obtained for the overall filter, and then a harmonic ac analysis has been performed to verify the frequency response of the designed filter. As shown in figure 3.14, the center frequency is 9.6163MHz, the bandwidth is 26Khz, and the insertion loss is -1.34dB.

Parameter	Value	Units	Parameter	Value	Units
Beam Length, L_r	40	μm	Filter Band Width, $\Delta\omega$	19.31	KHz
Beam Width, W_r	8	μm	Filter Quality Factor, Q_{fltr}	500	–
Beam Thickness, h	2	μm	Coupling Beam Length, L_s	17.25	μm
Electrode Width, W_e	16	μm	Coupling Beam Width, W_s	2	μm
Electrode-to-Beam Gap, d_o	0.75	μm	Coupling Location, l_c	5	μm
Resonator Q	13834	–	Center Frequency, f	9.6562	MHz
Resonator Mass, m_r	5.9058×10^{-13}	Kg	Modification Factor, κ	0.9002	–
m_r at coupling point, m_{rc}	1.8726×10^{-11}	Kg	Poisson's Ratio	0.225	–
Resonator Stiffness, k_r	2174	N/m	Young's Modulus, E	163	GPa
k_r at coupling point, k_{rc}	68931	N/m	Density of Polysilicon, ρ	2330	Kg/m^3
Damping Constant, C_r	2.5901×10^{-9}	Ns/m	DC Bias, V_P	80	V
Transduction Factor, Γ	1.6118×10^{-7}	C/m	Termination Resistor, R_t	1.86	$M\Omega$

Table 3.6 Design specifications and geometries of the 10MHz band-pass Filter

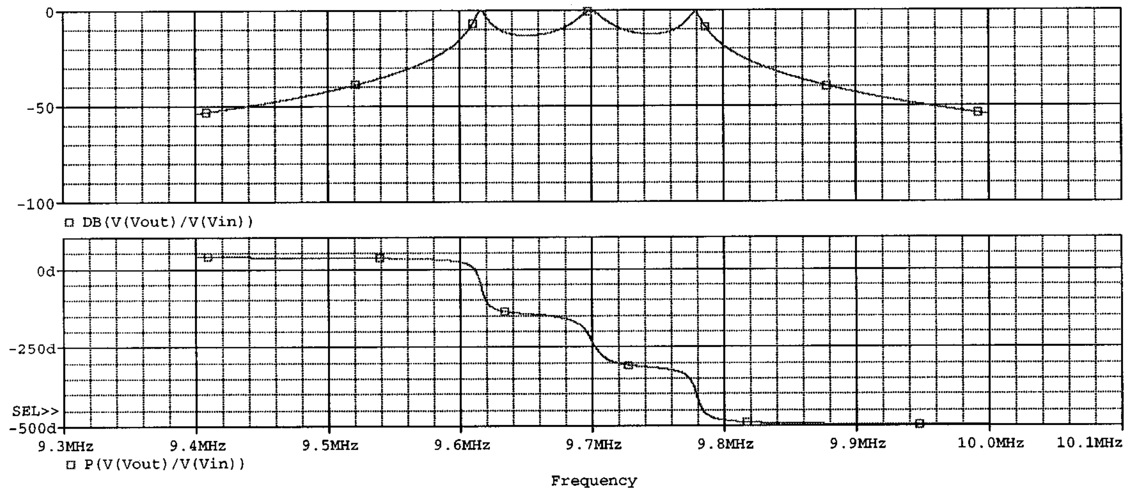

Fig. 3.14 Frequency response of the 10MHz band-pass filter

3.5 Fabrication Results

The proposed devices have been fabricated through CMC and by Cronos Integrated Inc. Normally each run (fabrication cycle) takes about 25 weeks. In total we have had two MUMPs runs from September 2003 to March 2005 to fabricate our devices by CMC. The first run was dedicated just for the clamped-clamped beam resonators and figure 3.15 shows an SEM picture taken from parts of our devices. The cantilever beam, disk resonators and the final band-pass filters have been sent for fabrication and we anticipated getting the chips by January 2005, however due to a delay in the foundry

service, the chips are scheduled to be shipped by April 2005. Figure 3.16 shows the whole layout of the second design which contains several resonators and band-pass filters with different configurations.

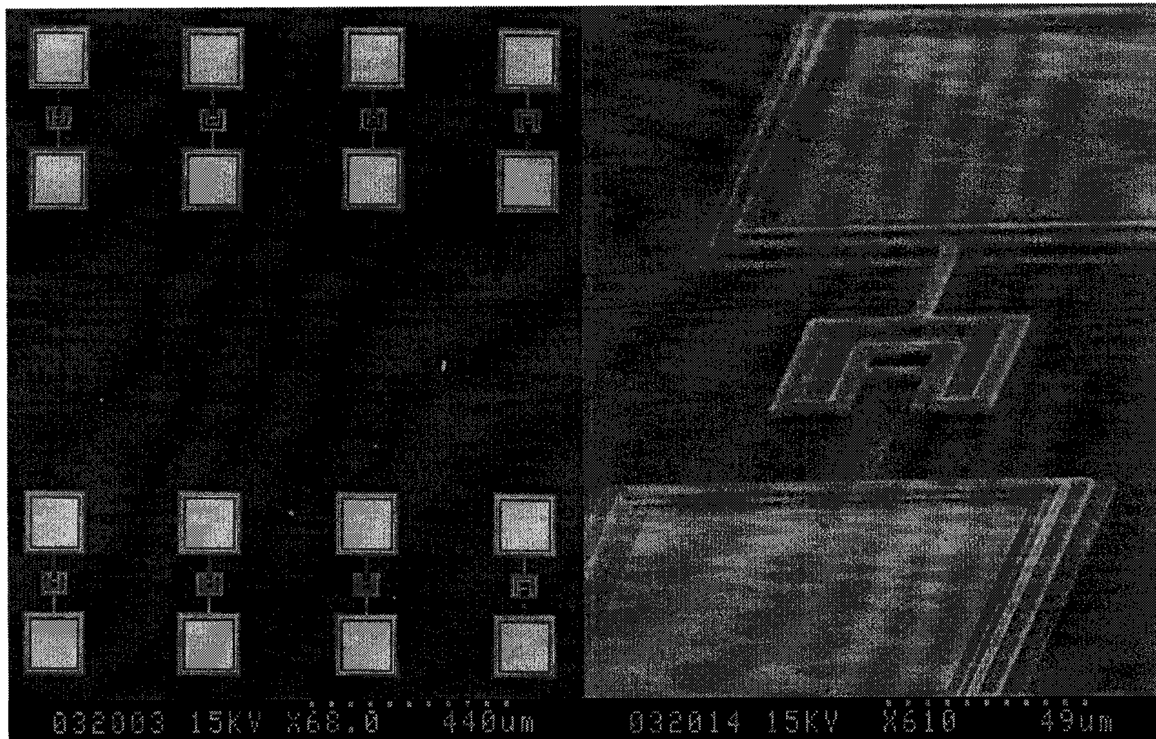

Fig. 3.15 SEM picture of the clamped-clamped MEMS resonators (first MUMPs design)

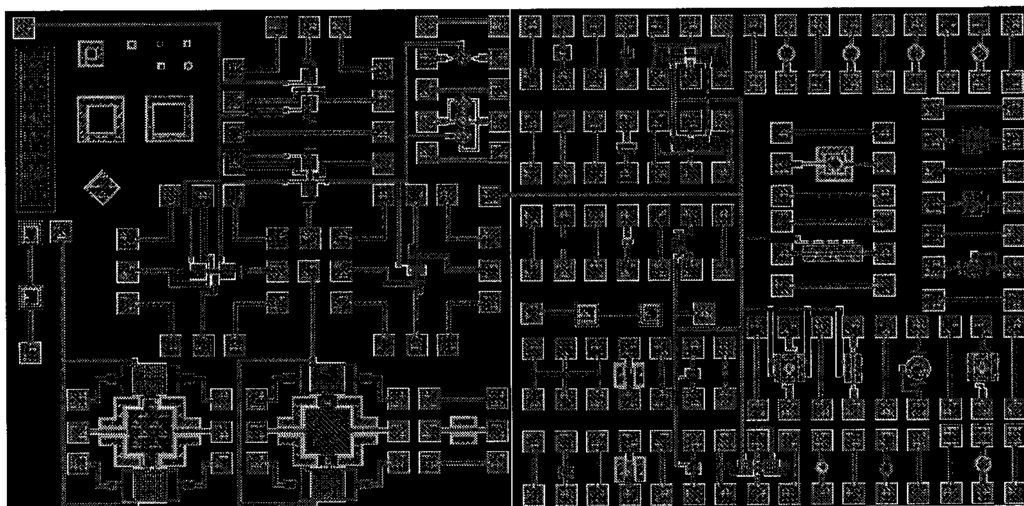

Fig. 3.16 Layout of the second MUMPs design

3.6 Post-Processing for MUMPs

After the device is fabricated, the chips are shipped back for post-processing. The only post-processing step for MUMPs is a simple HF release [25]. HF release is the process which uses concentrated (49% resolution) HF etchant to etch away the Phosphosilicate Glass (PSG) sacrificial layer between the poly structural layers and thus free the mechanical structures. The release process can be performed as recommended in MUMPs Handbook [25], firstly chips are immersed in acetone for 3 minutes, and then in De-ionized (DI) water for 30 seconds. Then chips are put in the 49% HF at room temperature and for 1.5 to 2 minutes to etch the oxide (PSG). This is followed by several minutes in DI water and then alcohol for 5 minutes to reduce the stiction, followed by at least 10 minutes in an oven at 110°C.

3.7 Variable MEMS Capacitor

This section presents the design and fabrication of a novel MEMS parallel-plate variable capacitor which can be used in integrated RF filters. This MEMS capacitor has been fabricated using the standard TSMC CMOS 0.35 μm technology and demonstrates the possibility of monolithic integration of a MEMS device with electronic circuitry within a single chip. A brief description of the fabrication technology has been presented in section 1.2.5. Four metallization levels are available through the process, metal1 to metal4. The last metal layer has been used as a mask to perform a DRIE post-processing after fabrication. The third and first metal layers have been used as the structural layers for the top and bottom plates, respectively. The second metal layer will be sacrificially etched away, using an aluminum etchant, during the post-processing steps to create the air gap between the capacitor plates. First we will discuss the design procedure of this capacitor and then the fabrication and post-processing results will be presented.

3.7.1 Design of the Variable MEMS Capacitor

Figure 3.17 shows the top and cross-section views of a 0.12pF tunable capacitor with two parallel plates. Metal1 and Metal3 aluminum layers were selected as capacitor plates, because of the superior electrical properties of aluminum at RF frequencies. A summary of selected CMOS 0.35 μm process parameters are presented in Table 3.7. The gap

between the electrodes consists of two silicon dioxide layers and an air gap created by sacrificial etching of the metal2 layer.

Layer	Thickness	Sheet Resistance	Layer	Thickness	Sheet Resistance
Metal1	0.665μm	0.083Ω/sq	Poly2	0.180μm	50 Ω/sq
Metal2	0.640μm	0.080Ω/sq	Oxide1	0.428μm	-
Metal3	0.640μm	0.080Ω/sq	Oxide2	1.000μm	-
Metal4	0.925μm	0.051Ω/sq	Oxide3	1.000μm	-
Poly1	0.275μm	8.0 Ω/sq	Oxide4	1.000μm	-

Table 3.7 Summary of selected CMOS 0.35 μm process parameters

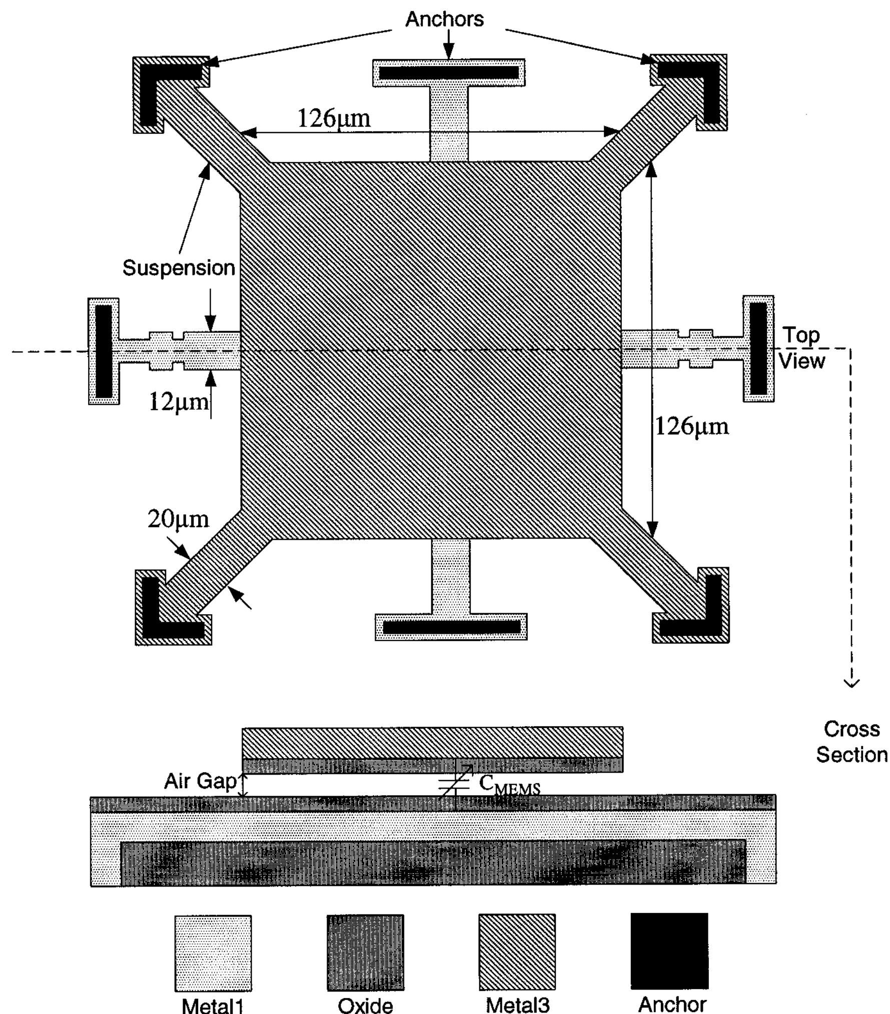

Fig. 3.17 Top and cross-section views of a two parallel-plate MEMS tunable capacitor

The desired capacitance of 0.12pF can be achieved with a 126μm×126μm plate area using the following equation

$$C_{MEMS} = \frac{\varepsilon A}{d_{air} + \dfrac{d_{ox1} + d_{ox2}}{\varepsilon_{ox}}} \qquad 3.17$$

where $\varepsilon_{ox} = 3.9$ is the relative permittivity of silicon dioxide, d_{ox1} and d_{ox2} are the thickness of the oxide2 and oxide3 layers respectively, given in Table 3.7. Figure 3.18 presents the simulation results for a specific 126μm×126μm parallel-plate MEMS capacitor. Transient response of this capacitor is shown in figure 3.18(a), when a 10V actuation voltage is applied between the parallel plates. Figure 3.18(b) presents the C-V characteristic for the same capacitor, the capacitance changes from 0.12pF to 0.15pF with an actuation voltage ranging from 0 to 12.5Volts.

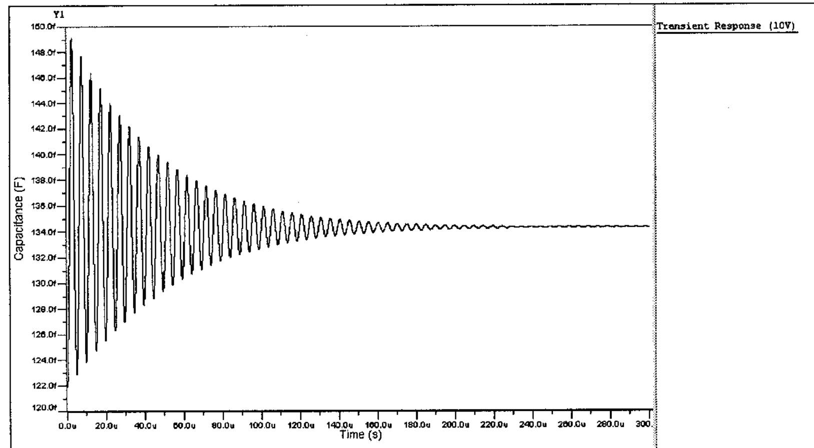

(a)

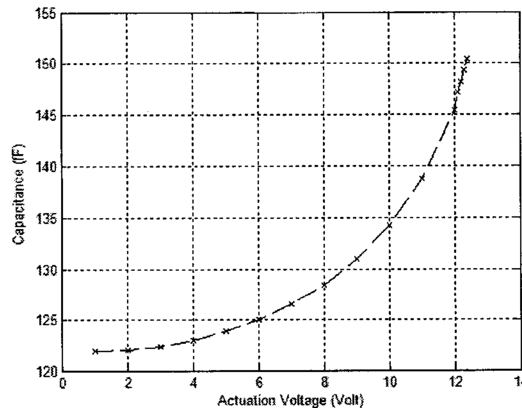

(b)

Fig. 3.18 Transient response and C-V characteristic of a MEMS capacitor

Based on the simulation results with ANSYS the pull-in voltage is 12.43V, a spring constant of 56 N/m is necessary in order to achieve a maximum capacitance of 0.15pF under the maximum bias voltage of 12.43V. The mass of the suspended top plate, which is composed of an aluminum and oxide layers, is $2.743\times10^{-11} Kg$. Figure 3.19 shows a diagram of the suspension which has been used in the design of the tunable capacitor. The equivalent spring constant of the suspension beam can be obtained by [57]

$$k = \frac{EWT^3}{L^3} \tag{3.19}$$

where W , T , and L are the width, thickness, and length of the beam, respectively and E is the Young's modulus of aluminum (approximately 70GPa). Totally there are four suspensions and the overall spring constant is $k_{tot} = 4k$.

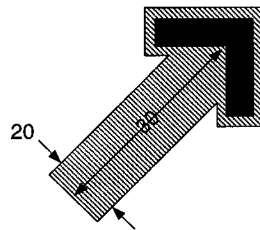

Fig. 3.19 Diagram of the suspension beam

3.7.2 Post-Processing for the Variable MEMS Capacitor

After the chips come back from the CMOS foundry, several post-processing steps are required in order to create the air gap between the parallel-plates. Also the fabricated MEMS capacitors suffer from low Q-factor at RF frequency range due to the stray capacitance between the bottom plate and the silicon substrate which produces high insertion losses. Flip-Chip technology can be used to transfer the fabricated devices to another alumina substrate by an extra fabrication cost. Our work describes a novel approach based on wet etching of silicon substrate with TMAH that improves the Q-factor of the fabricated MEMS variable capacitors at RF frequency range.

The first post-processing task involves the removal of silicon dioxide around the MEMS structure as presented in figure 3.20. The main purpose of removing oxide is two fold, first to expose metal2 layers which must be etched using an aluminum etchant in

order to create the air gap between the capacitor plates and second, to expose the silicon substrate in the areas that should be anisotropically etched using TMAH.

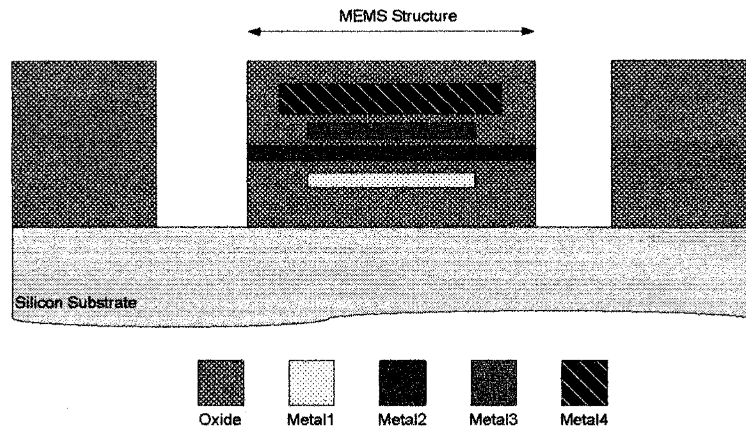

Fig. 3.20 Oxide removal for MEMS structures

As mentioned before in section 1.2.5, for previous CMOS processing, by proper stacking of "Via" layers which are the holes patterned in the oxide layers, it is possible to easily create the etch windows during the fabrication process. However, this method of creating etch windows are not supported anymore by the CMOS foundry (MOSIS), because it violates the new design rules made since September 2003. Thus the oxide removal should be performed during the post-processing steps after the chips are back. To this end we can use two different methods which have their own benefits and limitations. The first one is to do a Deep Reactive Ion Etching (DRIE) step on the fabricated CMOS chips and the top metal layer, metal4, must be used as an etch-resistant mask to cover the structural layers. This method has been used before and its efficiency has been well proven during several MEMS designs [58, 59, and 60]. In this work we have used a novel method which needs just a single photolithography and silicon dioxide removal using Hydro Fluoric (HF) acid. The main draw back of this method is that it is not a mask-less post-processing technique.

Figure 3.21(a) shows the fabricated chip which is come back from the CMOS foundry and without performing any post-processing step. This chip contains several MEMS devices from different designers along with the MEMS variable capacitor. Also the mask which will be used for the photolithography is presented in figure 3.21(b). The dark areas

are the transparent widows for the UV light and define the etch windows. Table 3.8 summarizes the post-processing steps and the parameters at each step.

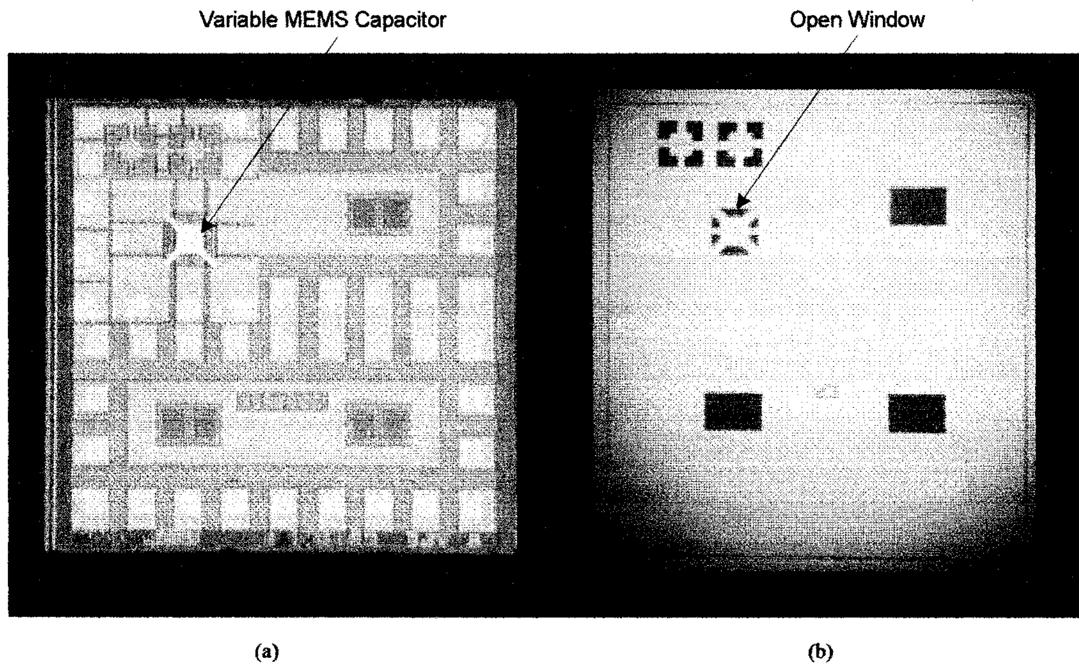

Fig. 3.21 The fabricated CMOS chip and the mask which will be used for post-processing

Post-Processing Step	Parameters
Spinning and photoresist deposition	Photoresist: Microposit S1813 Speed: 3000 RPM
Soft baking	Time: 30min, Temperature: 110°C
UV exposure	Exposure Time: 25sec
Developing	Developer: Microposit MF-319
Hard baking	Time: 30min, Temperature: 110°C
Oxide removal with HF	5:1 BHF (NH_4F:HF 49%), Room Temperature
Silicon removal with TMAH	TMAH 5%, Time: 1hr 45min, Temperature 90°C

Table 3.8 CMOS post-processing steps

First the chips are attached on top of a thin glass substrate which works as a holder during the post-processing steps and then using a spinner the photoresist is deposited on top of the chip. The deposited photoresist should be as thin as possible to facilitate the mask aligning process. Figure 3.22 shows the chip with a thin photoresist layer, as shown

in this figure, the deposited photoresist is not completely even due to the fact that the chip is too small and because of the limitations in the available lab facilities.

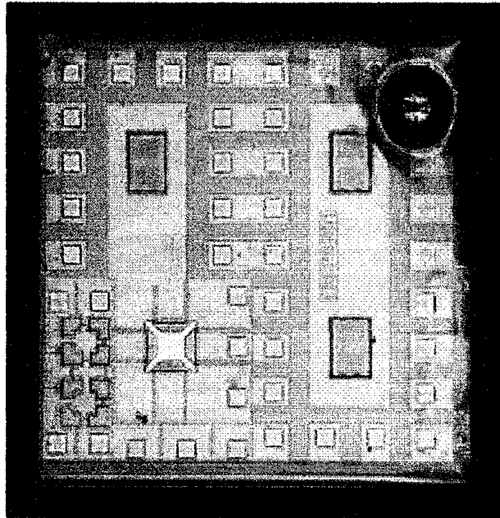

Fig. 3.22 A photograph of the chip after depositing the photoresist layer

Next the chips will be put inside an oven at 110°C for soft baking for 30 minutes and then they are ready to be exposed to the UV light. The mask aligning has been done using Quintel double-sided mask aligner in the microelectronics lab. This aligner has an accuracy of around 1μm in mask alignment. After aligning the chip will be immersed inside the developer for one minute followed by rinsing with DI water. The developed chips need to be hard baked in the oven at 110°C for another 30 minutes and then they are ready for silicon dioxide etching with HF.

The oxide etching step is very challenging process due to the fact that the etching is isotropic and the control on the etch rate is very important. HF etches both the oxide and metal layers simultaneously and in order to keep the pads and structural parts intact we have to find the best etch time and the best etchant recipe. Based on our experimental results, a 5:1 Buffered HF (BHF) solution is the best recipe where as a buffer we have used Ammonium Fluoride (NH_4F). Furthermore by adding Glycerol ($C_3H_8O_3$) to the final solution (6:70, $C_3H_8O_3$:BHF) we can decrease the etch rate of aluminum layers. The etch rate of the silicon dioxide using this solution is around 85 nm/min which means that to etch the total oxide layer with a thickness of 3.5μm, the samples should be left in this

solution for 40 minutes. In this work we didn't consider the effect of the temperature on the etch rate and we did all the experiments at room temperature, however it is an important parameter in determining the etch rate which for better control should be taken into account. Figure 3.23 presents an SEM image of the chip after the oxide removal which is ready for the substrate etching using TMAH.

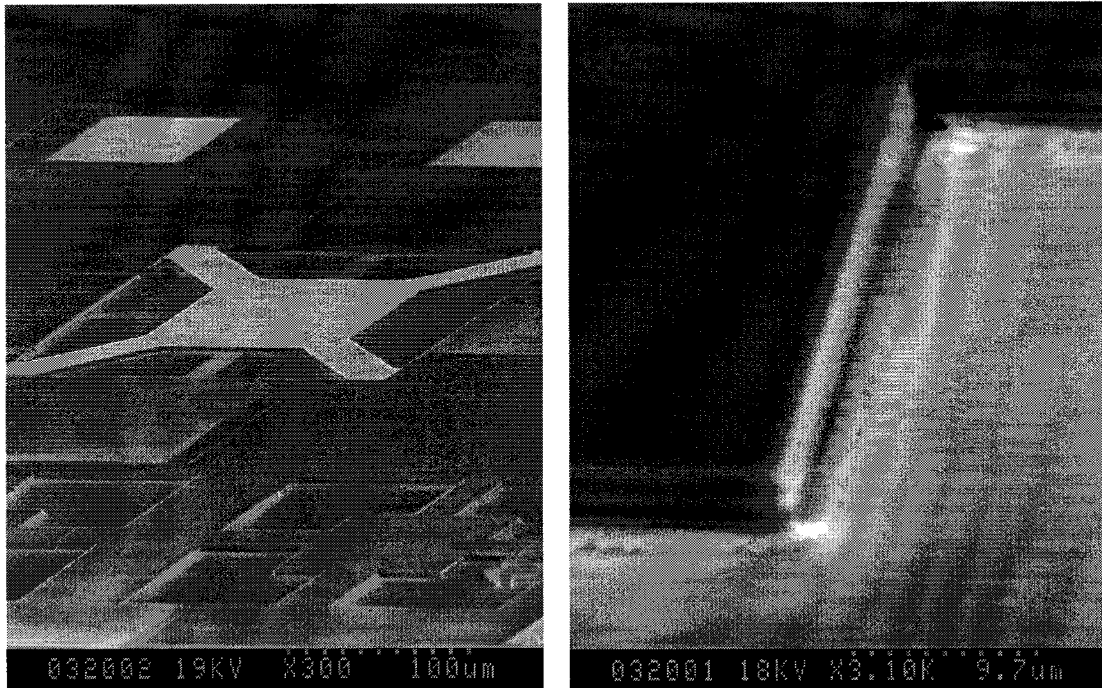

Fig. 3.23 SEM image of the device after removing the oxide layer

Typically low resistivity of silicon substrate imposes difficulties for RF design due to noise coupling and substrate loss and the last post-processing step, anisotropic substrate etching, is used to improve the device performance and characteristics. The etchant is diluted 5% TMAH and the etching temperature is 90°C. The etch rate of silicon at these working conditions is around 0.5μm/min. Figure 3.25 shows a schematic view of the TMAH setup.

An SEM image of the final released variable MEMS capacitor after 1 hour and 45 minutes in TMAH is presented in figure 3.24 where the depth of the created cavity is about 60μm. As shown in this figure the silicon beneath the bottom plate is not completely removed and for this purpose we have to perform an isotropic dry etching

with XeF_2 which will be discussed as a future work. As shown in figure 3.26 this isotropic etching step helps to totally remove the silicon under the bottom plate.

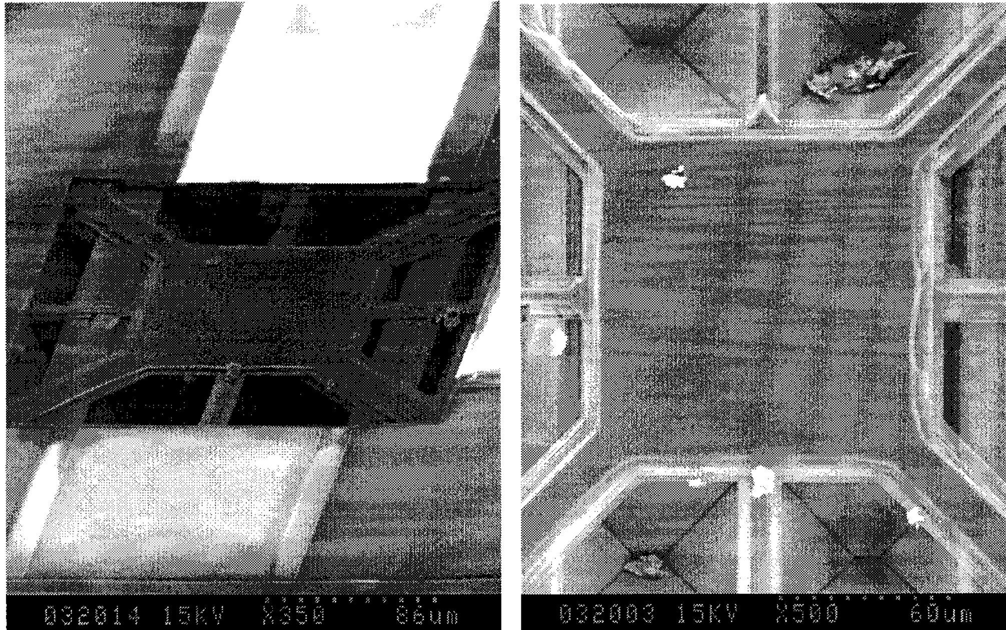

Fig. 3.24 SEM image of the final variable MEMS capacitor after post-processing steps

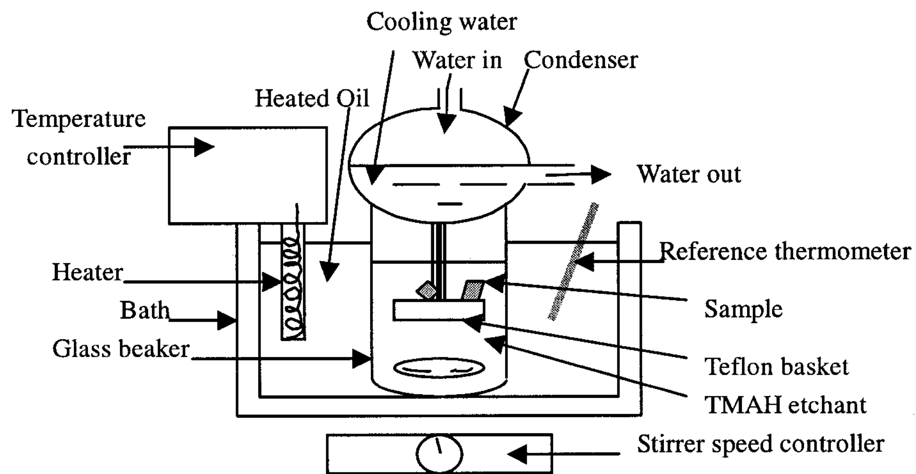

Fig. 3.25 TMAH setup [61]

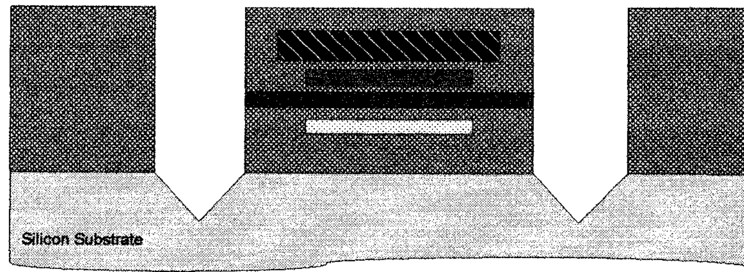

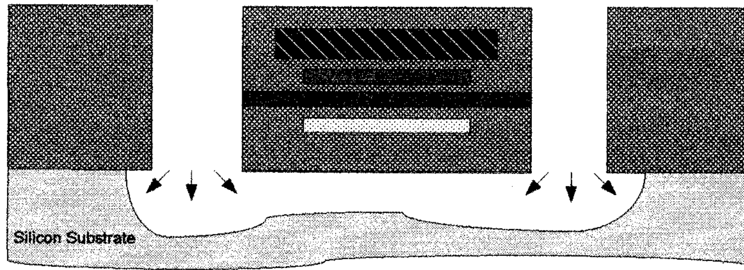

Fig 3.26 Anisotropic etching followed by isotropic etching with XeF_2

Chapter 4
Experimental Setup and Results

In this chapter we will discuss the test plan, experimental setups, observations, and results for the fabricated MEMS resonators and variable capacitor. For RF integrated circuits there are two different test approaches; the first one involves packaging and fixturing using RF test boards and the second approach is based on probing using special RF probes. Because of the parasitic effects of the package and the test fixture, the second approach is preferred, however it needs a sophisticated RF probed station and measurement equipment. In this work we have used the first test approach for both RF MEMS devices.

4.1 Bonding and Packaging

The first step after fabrication and post-processing steps, towards the test and measurement, is bonding and packaging of the chip. There are several packages such as DIP40, PGA68, or CFP80, the type of the package is selected according to the test fixture which will be used during the measurements. For the MEMS resonators we have used DIP40 and for the MEMS variable capacitors with a higher operating frequency range, CFP80 which is an 80 pin ceramic flat package, has been used as shown in figure 4.1. The bonding has been done in the mechanical department using a manual bonder machine from West-Bond Inc. For the MEMS resonators fabricated by PolyMUMPs technology the pads are made of gold but, for the CMOS MEMS capacitors the pads are aluminum and as a result each device requires different bonding conditions.

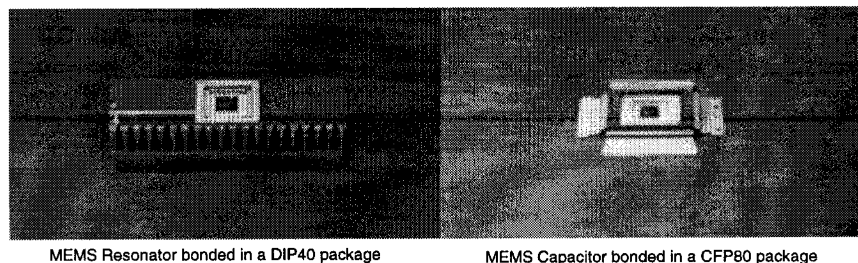

MEMS Resonator bonded in a DIP40 package MEMS Capacitor bonded in a CFP80 package

Fig. 4.1 Bonded devices

4.2 Experimental Setup and Results for the MEMS Resonators

The main characteristic of the MEMS resonators which should be measured is their resonance frequency. As shown in figure 4.2 the MEMS resonator could be considered as a two port network, where the input is an ac signal $A_1e^{j\omega_1 t}$ with amplitude A_1 and radian resonance frequency of ω_1. If the frequency of the input signal is close to one of the modal resonance frequencies of the MEMS resonator then at the output port we will observe an ac signal $A_2e^{j\omega_2 t}$, where $\omega_1 = \omega_2 = \omega_o$ and ω_o is the radian resonance frequency of the MEMS resonator.

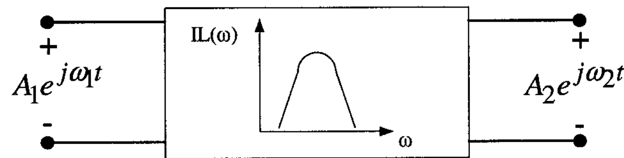

Fig. 4.2 MEMS resonator as a two port network

The ratio between the voltage amplitudes A_1 and A_2 is called the transmission coefficient. The transmission coefficient between two points in a circuit is often expressed in dB as the insertion loss IL, defined by

$$IL(\omega) = 20\log|T(\omega)|dB \qquad 4.1$$

Due to the fact that the maximum amplitude of the output signal occurs at the resonance frequency of the MEMS resonator, $IL(\omega)$ has a peak at $\omega = \omega_o$ and this characteristic can be utilized in determining the resonance frequency of the fabricated MEMS resonators. The best method to find the insertion loss of the resonators versus the frequency of the input signal is to use a network analyzer as depicted in figure 4.3 and to directly measure the S21 parameter of the device which is equivalent to the transmission coefficient from port 1 to port 2. The network analyzer measures the ratio of the amplitude at the test channel to the amplitude at the reference channel $\frac{A_t}{A_r}$ which is usually expressed in dB.

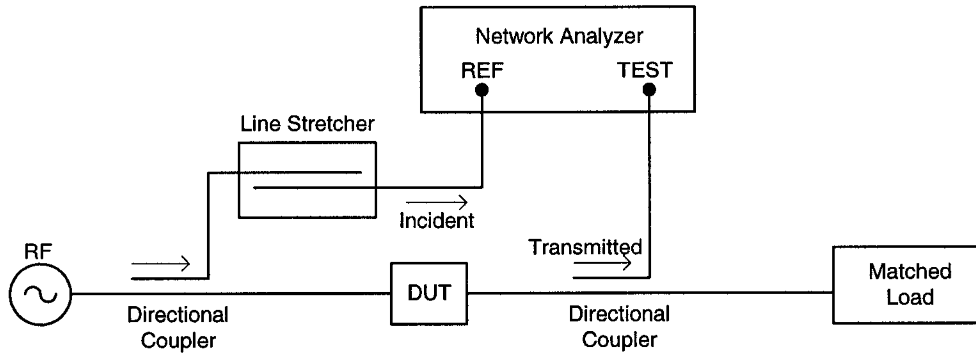

Fig. 4.3 S21 measurement with network analyzer

This method of S21 measurement is very accurate and using the calibration techniques prior to do the measurements for the Device Under Test (DUT), we can eliminate the effects of the coupling cables and connectors. However in measuring the resonance frequency of the MEMS resonators in this work, there are two main limitations using this technique. First as mentioned before, the resonators should be biased with a proper DC voltage which is applied to the drive electrode. At the same time the drive electrode is connected to the REF port of the network analyzer. For the available network analyzers which we have in the microwave lab, the maximum DC voltage which can be applied to the REF port is just 24V. The fabricated MEMS resonators need a DC bias voltage of at least 80V in order to have an acceptable transduction factor which yields a detectable output signal. This limitation can be resolved using a Bias-Tee which is a three port RF component as shown in figure 4.4. It has one RF and one DC input and the output is RF+DC. Using a bias tee it is possible to apply a DC bias voltage to the resonators, however again for the available bias-tee the maximum DC voltage is less than 50V.

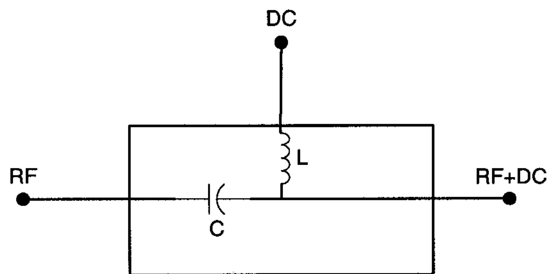

Fig. 4.4 Bias-Tee as a three port component

Another limitation of the network analyzer in measuring the center frequency of the resonators is the frequency range. Network analyzers are typically used for GHz frequency range but, the resonance frequency of the designed MEMS resonators are just a few ten mega hertz. Besides the minimum frequency range, as the quality factor of the MEMS resonators is very high, in order to be able to detect the pick in the transmission coefficient, the frequency of the input signal should be swept very gently in steps of less than 10Hz. These limitations push us to use another method in our measurements. Figure 4.5 presents the experimental setup which we have used in testing the MEMS resonators. A digital controllable Agilent ac signal source has been used for the input signal, using this signal source it is possible to obtain a minimum resolution of 0.01Hz for the frequency of the input signal which is small enough to be able to detect the pick in the transmission coefficient and hence the resonance frequency.

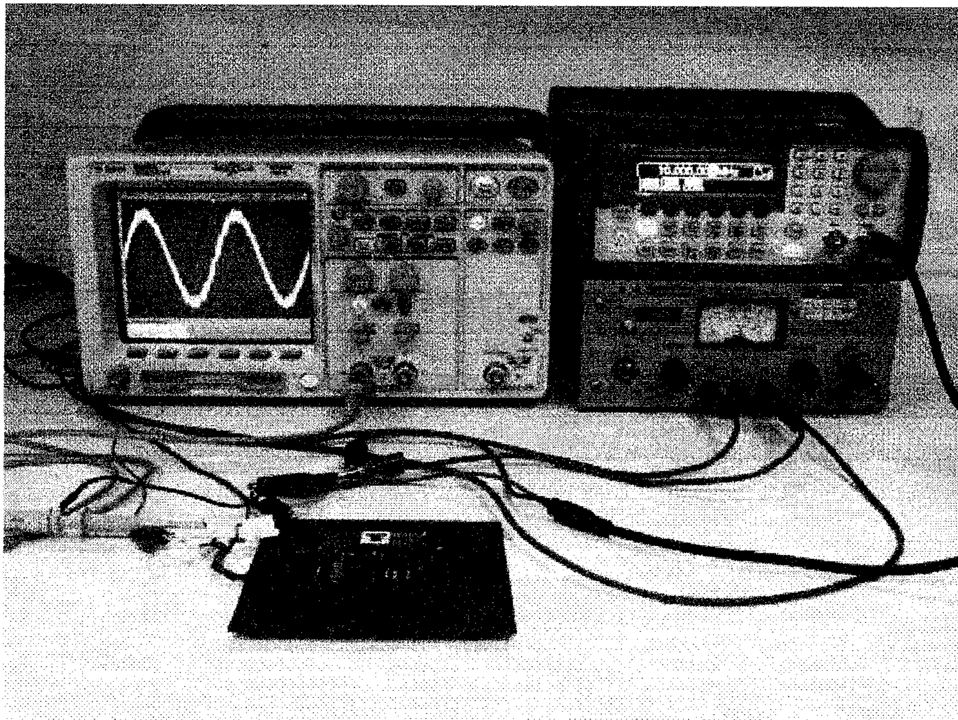

Fig. 4.5 Experimental setup for the MEMS resonators

A schematic view of the test setup, bias, and sensing circuitry is presented in figure 4.6. As shown in this figure, the input signal is fed to the drive electrode of the MEMS resonator along with a proper DC bias voltage taken from a high voltage DC power supply through a resistor. The resistor has been used as a current limiter in case of a short circuit between the drive electrode and the resonator beam due to the pull-in effect. The output port is connected to a high frequency Tektronix digital storage oscilloscope. The input frequency is swept within a frequency range close to the simulation results and the ratio of the amplitude at the output port to the amplitude at the drive electrode has been measured to find the transmission coefficient (insertion loss) versus frequency.

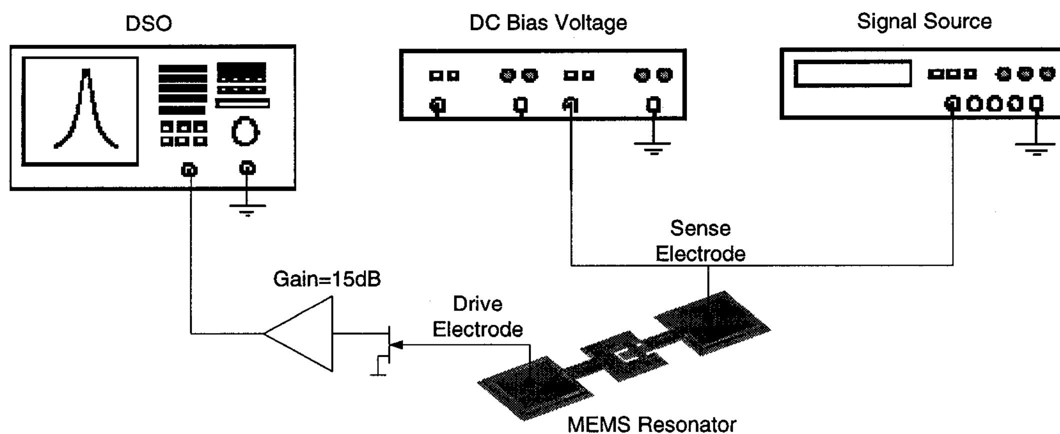

Fig. 4.6 Schematic view of the test setup

The resonance current at the output port was detected using an amplifier block with a low-noise high frequency junction field-effect transistor (JFET) 2N3819 as the first stage. The measured gain of this amplifier at 10MHz is 15dB. Figure 4.7 presents the schematic of the amplifier, the JFET operates in a common-source configuration using a drain resistor $R_d = 270\Omega$. Resistor R_1 allows us to set the input impedance to any desired value which commonly will be 50Ω. Transistor Q_2 is in common-base configuration and provides the isolation between the input and output stages, and Q_3 functions as an emitter-follower to provide low output resistance which is about 50Ω for the DSO. The simulation result of this amplifier is presented in figure 4.8, the simulated gain at 10MHz as shown in this figure is almost 14dB.

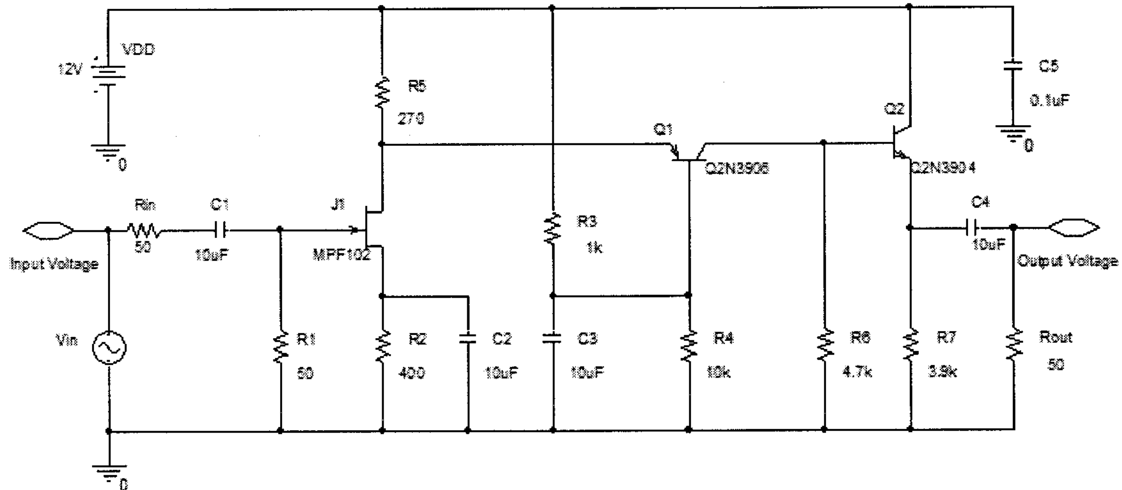

Fig. 4.7 Schematic view of the JFET amplifier

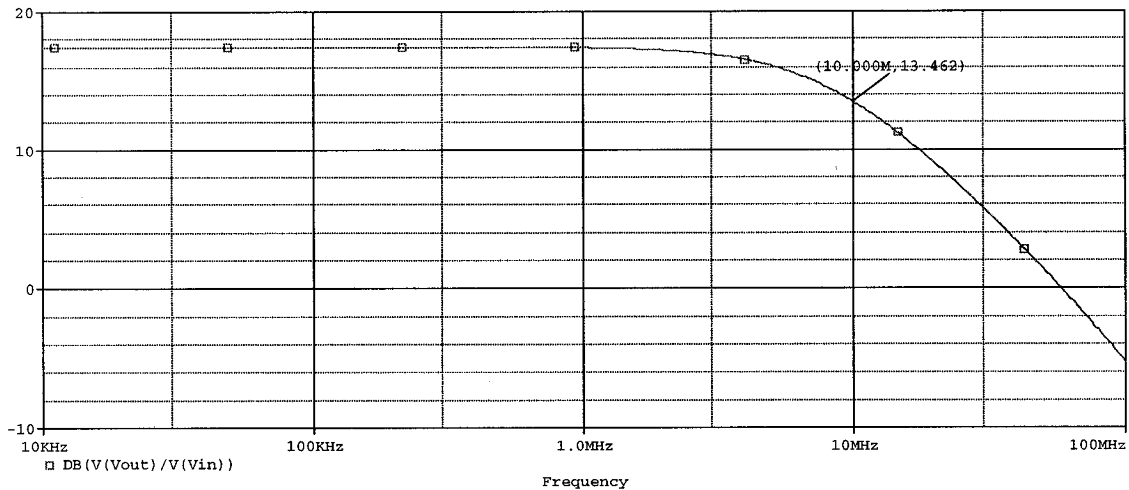

Fig. 4.8 Simulated gain of the JFET amplifier

The packaged chip along with the amplifier circuit is shown in figure 4.9. A simple comparison between the size of the fabricated MEMS chip and the analog amplifier circuit, implemented on a copper clad board, clearly presents the importance of MEMS integration with electronics. The PolyMUMPs process which has been used for the MEMS resonators is a process dedicated just for MEMS designs and using this process it is impossible to implement the electronic circuitry, however by using a standard IC fabrication technology such as CMOS for MEMS devices, it would be possible to integrate MEMS and electronics. The current standard CMOS process allows the

fabrication of some simple MEMS devices such as the variable MEMS capacitors in our work and it still needs more modifications in the design rules and materials to be able to fabricate a MEMS resonator using this technology.

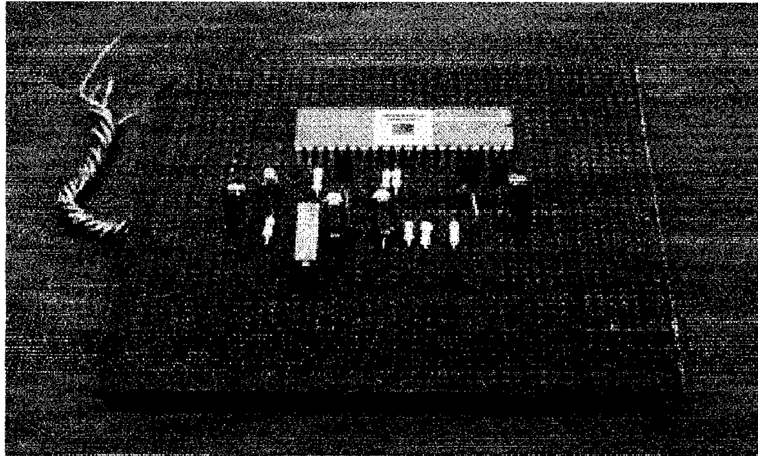

Fig. 4.9 MEMS chip and the required electronic circuitry

Using the test setup described above, three sets of measurements have been performed on the MEMS resonators; 1) transmission coefficient or frequency response of a 10MHz resonator 2) resonance frequency versus the applied DC bias voltage and 3) resonance frequency for different resonator beam lengths.

The 10MHz flexural-mode clamped-clamped MEMS resonator described in section 3.1 has been characterized to find its resonance frequency. Based on the simulation results the resonance frequency occurs at $f_O = 9.6562MHz$. In order to detect the peak in the amplitude response the frequency of the input signal has been linearly swept from 8.8MHz to 9.8MHz and totally we have obtained fifty data points on the curve shown in figure 4.10. The amplitude of the input signal is kept at 30mv during the test which guaranties that the device operates in the small-signal mode. As shown in this figure the peak occurs at $f_O = 9.21MHz$ and the amplitude response deviates from the one obtained by simulation shown in figure 3.5. There are several parameters affecting the measurement results. For example according to equation 3.3 the first modal resonance frequency depends on the Young's modulus of polysilicon E, which is a mechanical property related to the fabrication process and changes between two different runs due to

the conditions during the fabrication. Another parameter affecting the resonance frequency is the lithography tolerance. Because of this tolerance the exact dimensions of the fabricated MEMS resonators deviate from the ones listed in table 3.3 resulting in a measured resonance frequency different from the designed values.

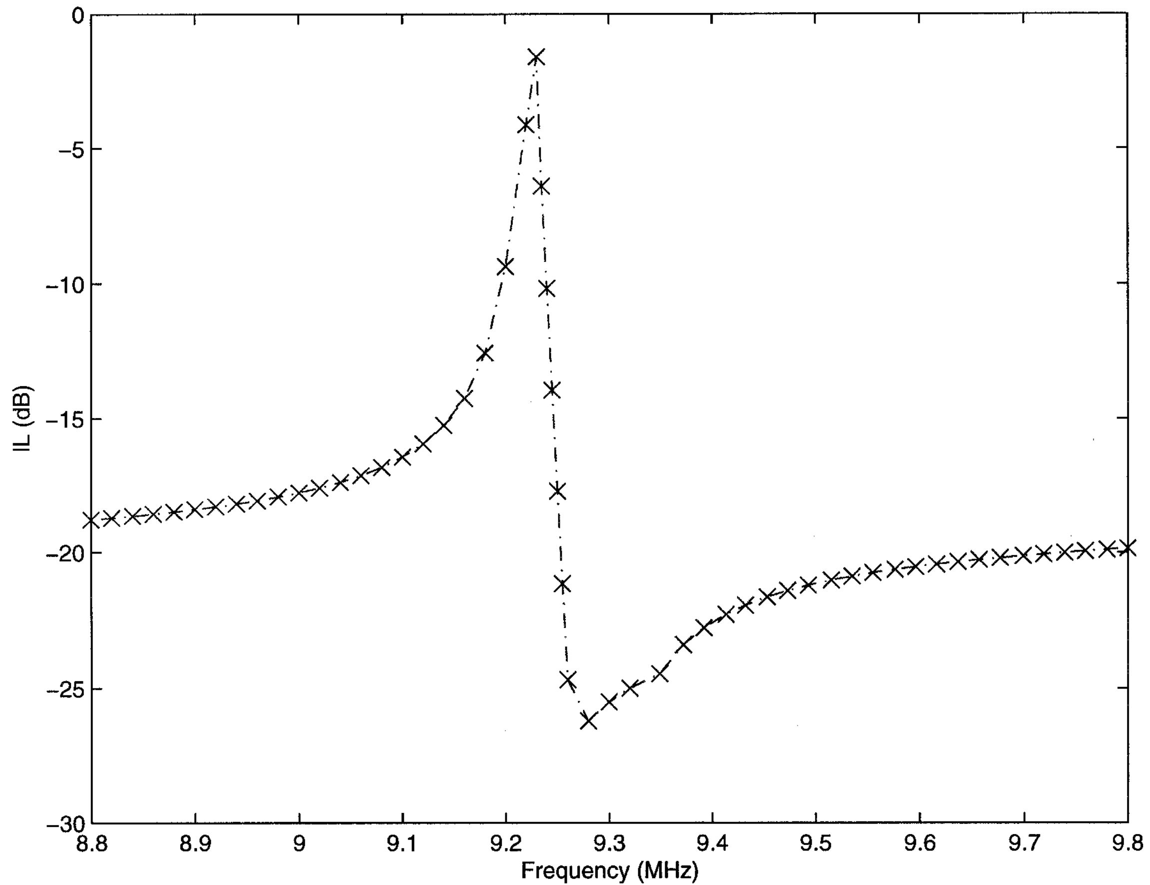

Fig. 4.10 Measured amplitude response of the 10MHz MEMS resonator

We can observe two different peaks, one negative and one positive, in the amplitude response depicted in figure 4.10. This divergence from the simulation result is because of the feedthrough parasitic capacitance which exists, in parallel with the resonator, between the drive electrode and the sense electrode. This parasitic capacitance can be determined by introducing a capacitor in the equivalent electrical circuit and fitting the simulation results with the measurement data. The feedthrough parasitic capacitance is obtained to be about 150fF.

Another factor causing the difference between the resonance frequency obtained by simulation and measurement is the variation in the air gap which can be explained using equation 3.6, and 3.7 repeated here for clarity

$$f = f_1\sqrt{1-g(d,V_P)} \text{ and } g(d,V_p) = \frac{1}{k_r}V_p^2\frac{\varepsilon_o W_r W_e}{d_o^3} \qquad 4.2$$

The air gap between the drive electrode and the resonator beam which for the simulations is assumed to be 2μm, is more than this value. During the HF release and sacrificial etch of the oxide, there is a minor etching of the poly structural layers which results in increasing the initial air gap and hence increasing the resonance frequency. The exact value of the air gap after HF release could be defined by doing the frequency measurement for different DC bias voltages and plotting the resonance frequency with respect to V_P as depicted in figure 4.11.

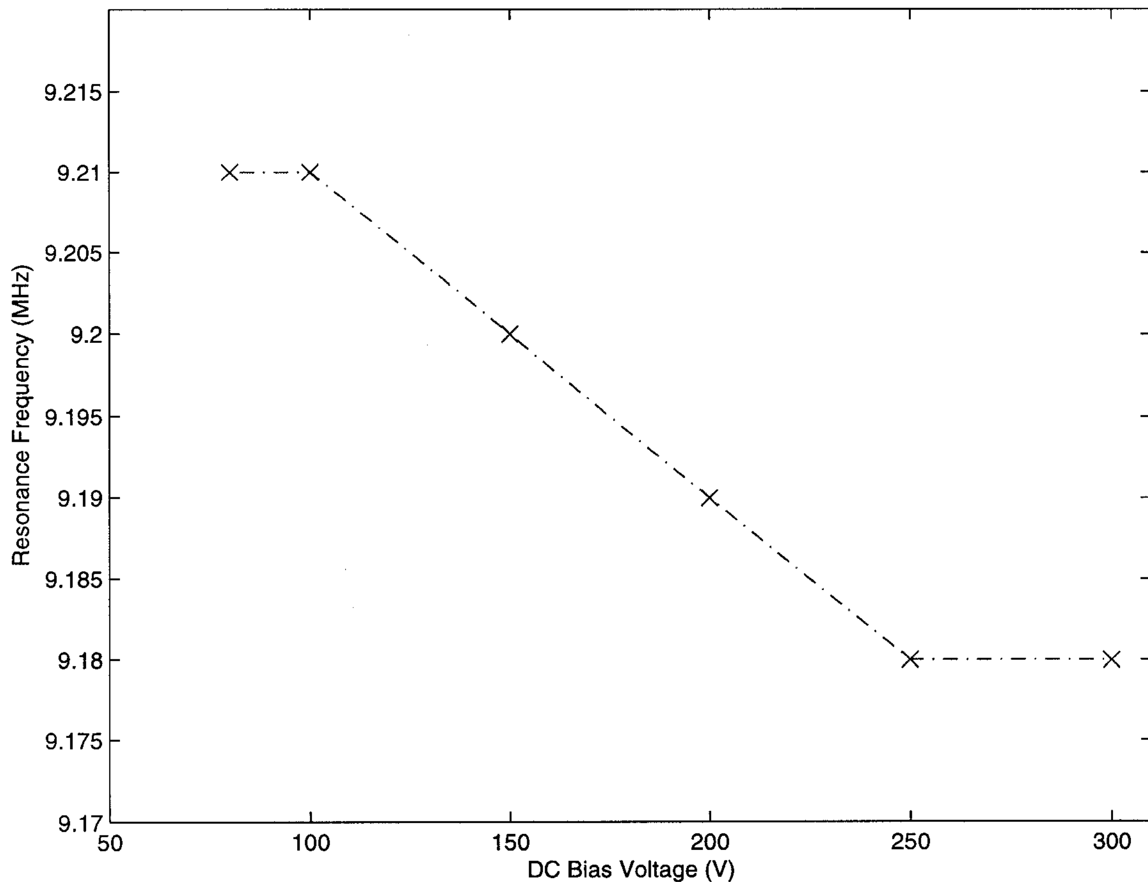

Fig. 4.11 Resonance frequency versus DC bias voltage

We have used the same 10MHz MEMS resonator for this measurement and changed the DC bias voltage from 80V to 300V. Using the described test setup it is very difficult to find the exact value for the resonance frequency, for example for both $V_P = 250V$ and $V_P = 300V$ we have obtained the same resonance frequency, a network analyzer can be used in determining the resonance frequency with more accuracy. By assuming that the other dimensions remains constant as listed in Table 3.3 the exact value of the final air gap after the HF release is obtained to be 2.08μm.

The first MUMPs design was dedicated just for the MEMS resonators with different dimensions and as a result different resonance frequencies ranging from 1 MHz up to 25MHz. Figure 4.12 shows the resonance frequency versus the beam length L_r for the fabricated MEMS resonators.

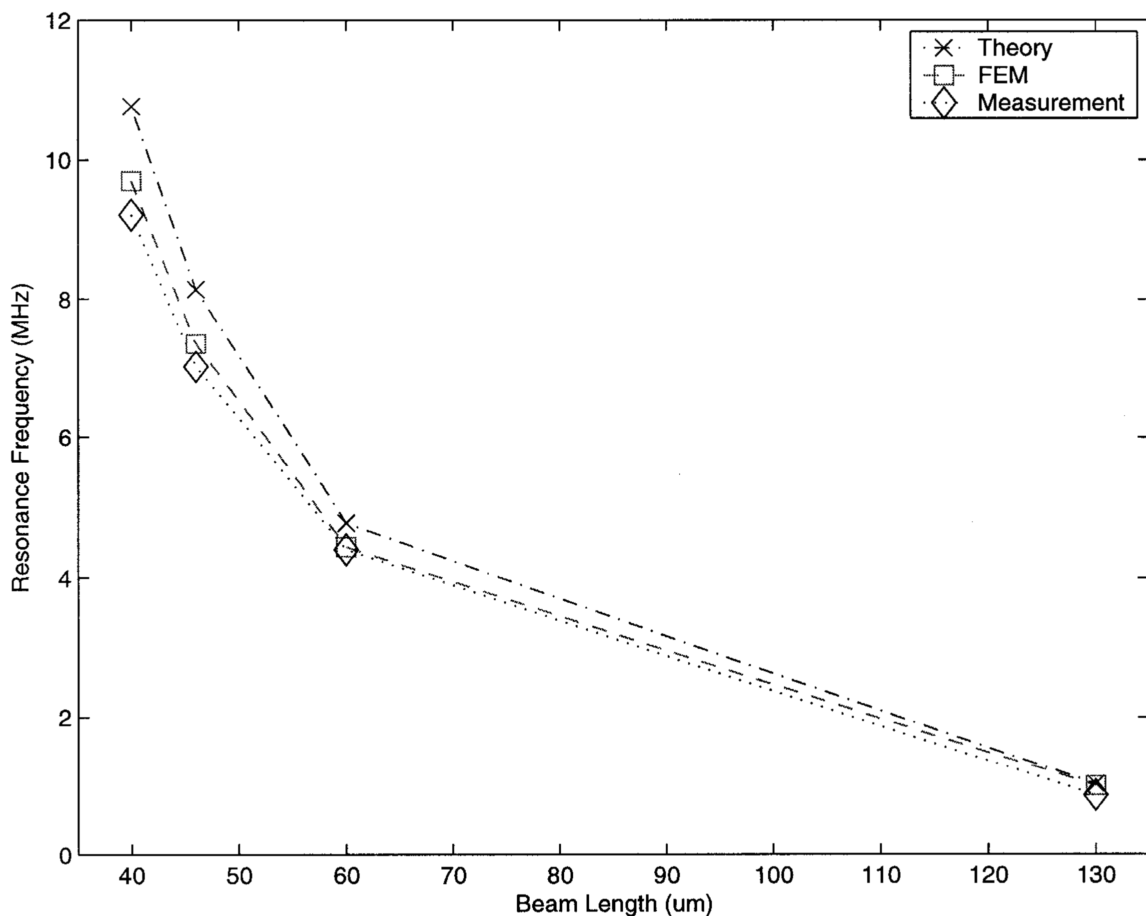

Fig. 4.12 Resonance frequency versus beam length

In this figure we can see the experimental results along with the theoretical and FEM simulation results. The theoretical results have been obtained using the classical beam theory and equation 3.4. For frequencies above 10MHz due to the limitations of the test setup we could not gather the experimental results. The limitation comes from the parasitic effects of the interface cables. This limitation in characterizing high frequency MEMS resonators again can be resolved using the network analyzer and calibration techniques or fiber optic interferometer explained in next section.

4.3 Fiber Optic Interferometer

Optical interferometric methods can be used for the analysis and measurement of resonant structures with the minimum impact on the device under test and with an extremely high resolution in determining the out of plane motions. The main advantage of the optical methods compared to the electrical measurement is their ability to operate without any physical contact and interaction with the device. Using this technique we can find the accurate resonance frequency of the MEMS resonators without the parasitic effects of the pads or other electrical interconnects.

Optical detectors for the motion of MEMS devices are mainly based on two basic interferometers known as Mach-Zehnder and Fabry-Perot. Figure 4.13 shows the principle of operation of the fiber optic Fabry-Perot interferometer.

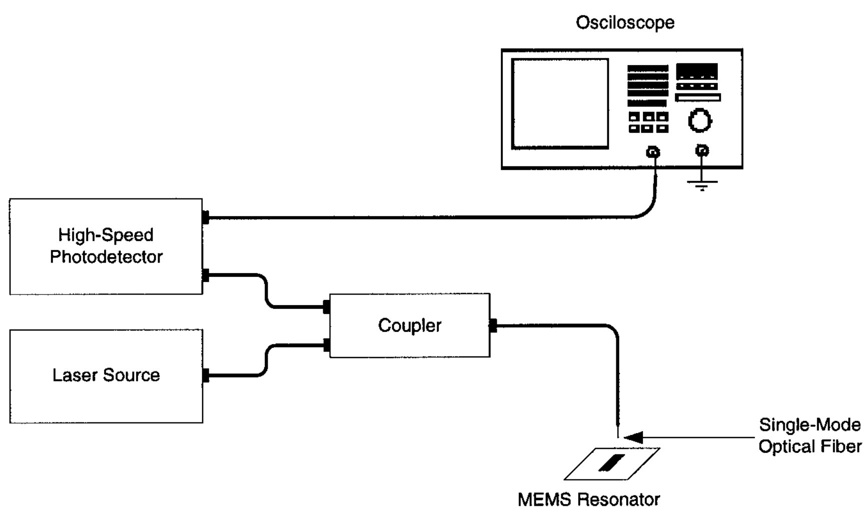

Fig. 4.13 Fiber optic Fabry-Perot interferometer

A probing laser beam is partly reflected by the surface of the resonating structure with its phase modulated due to the variation in the optical path length. By interference with a reference beam which remains unaffected from the sample motion, the phase modulation of the probe beam leads to an intensity modulation in the superposition and a high speed optical detector transforms intensity to a corresponding electrical signal. With an FFT analysis on the obtained electrical signal it is possible to find the resonance frequency of the MEMS device. The detailed theory of this type of interferometer is explained in [62]. Based on this principle, the size of the device can be as small as the diameter of a single mode fiber, i.e. typically 125μm.

For the fabricated flexural-mode beam resonators the width of the resonator beam is just around 8μm and it is very difficult to use this method of resonance frequency measurement, however for the disk resonators with a diameter of 40μm, the fiber optic interferometer seems to be a good candidate. The limitation for smaller devices can be resolved by using a fiber with a small diameter. As shown in figure 4.14 by using a diluted solution of Hydro Fluoric acid (HF) it is possible to obtain a single mode fiber which is suitable to do the measurements on the MEMS beam resonators. The diameter of the fiber shown in this figure has been decreased from 125μm to 10μm. The measurement of the MEMS resonators using the fiber optic interferometer has been left as a future work.

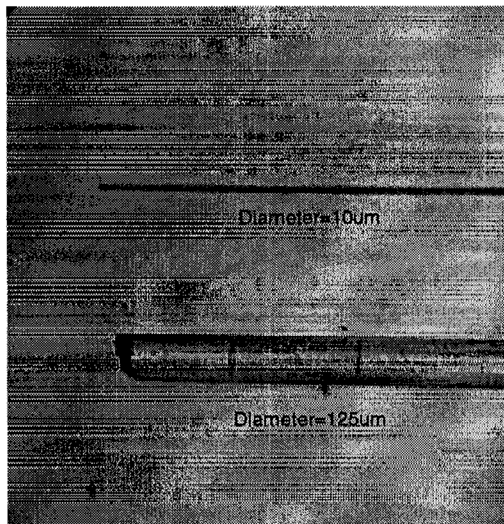

Fig. 4.14 A single mode optical fiber with a diameter less than 10μm

4.4 Experimental Setup and Results for the MEMS Variable Capacitor

The measurements on the MEMS variable capacitor have been done using an RF test board (CFP80TF) provided by CMC and an HP 8505A network analyzer in the microwave lab. After the chip is bonded in a CFP80 package it has been mounted on the RF test board using a plastic clamp as shown in figure 4.15. The CFP80TF RF test board has been developed for testing integrated circuits operating at frequencies up to 4.8GHz that have been packaged in the CFP80 package [63]. The main purpose of this test fixture or test board is to create an interface between the fabricated chip and the network analyzer. Totally there are twelve RF signal lines with SMA connectors for this board, in order to characterize the capacitors we will use just two of these RF lines. There are also four power lines which can be used to apply the DC actuation bias voltage between the capacitor plates. However because there should not be any DC voltage present at the test and reference ports of the HP 8505 network analyzer, during the measurements we won't apply the DC actuation voltage.

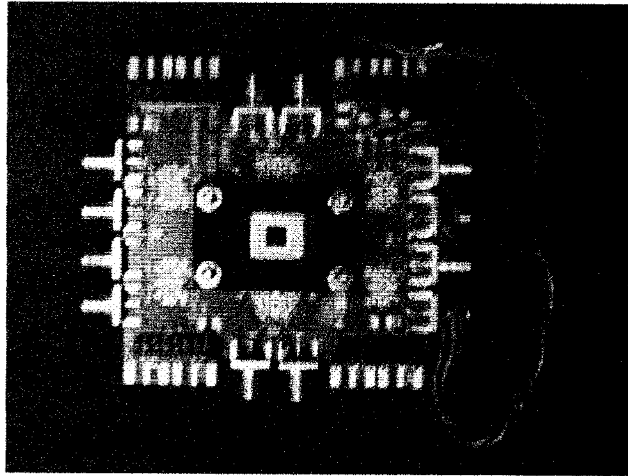

Fig. 4.15 RF test fixture and the clamped chip

As explained in section 3.7.2 and presented in the SEM image in figure 3.24, the silicon under the bottom plate has not been completely removed and as a result the measurements will include the parasitic capacitance between the bottom plate and the silicon substrate. Another parasitic capacitance which should be taken into account during the measurements is the parasitic capacitance of the pads.

The capacitor has been connected in the Ground-Signal-Ground (GSG) configuration to the RF signal lines as shown in figure 4.16 and using a network analyzer, we have found the impedance of the MEMS capacitor within a frequency range from 500MHz to 1GHz. The complete release of the bottom plate, using a dry etching such as XeF_2, and then accurate characterization (capacitance and quality factor) of this device has been left as a future work due to the unavailability of the network analyzer which we are planning to rent from CMC.

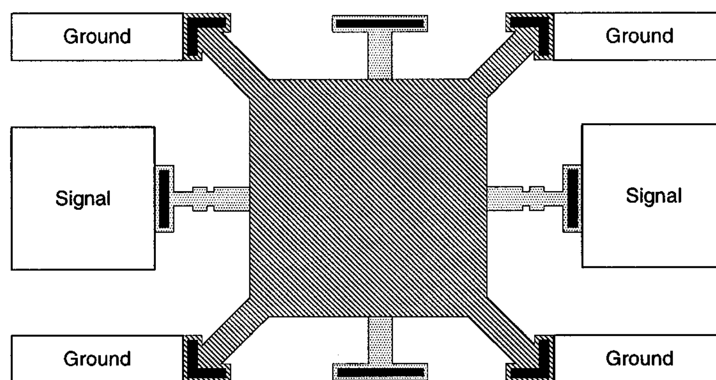

Fig. 4.16 MEMS capacitor in GSG configuration

Figure 4.17 shows the measured S11 parameter from 500MHz to 1GHz. The input impedance at 500MHz is $1.117 - j98.12$ which results in a measured capacitance of 3.16pF and the Q-factor is 88. The measured Q-factor at 1GHz is 28 and is less than the one obtained at 500MHz due to the skin-depth effect and also because of the increased capacitance at this frequency.

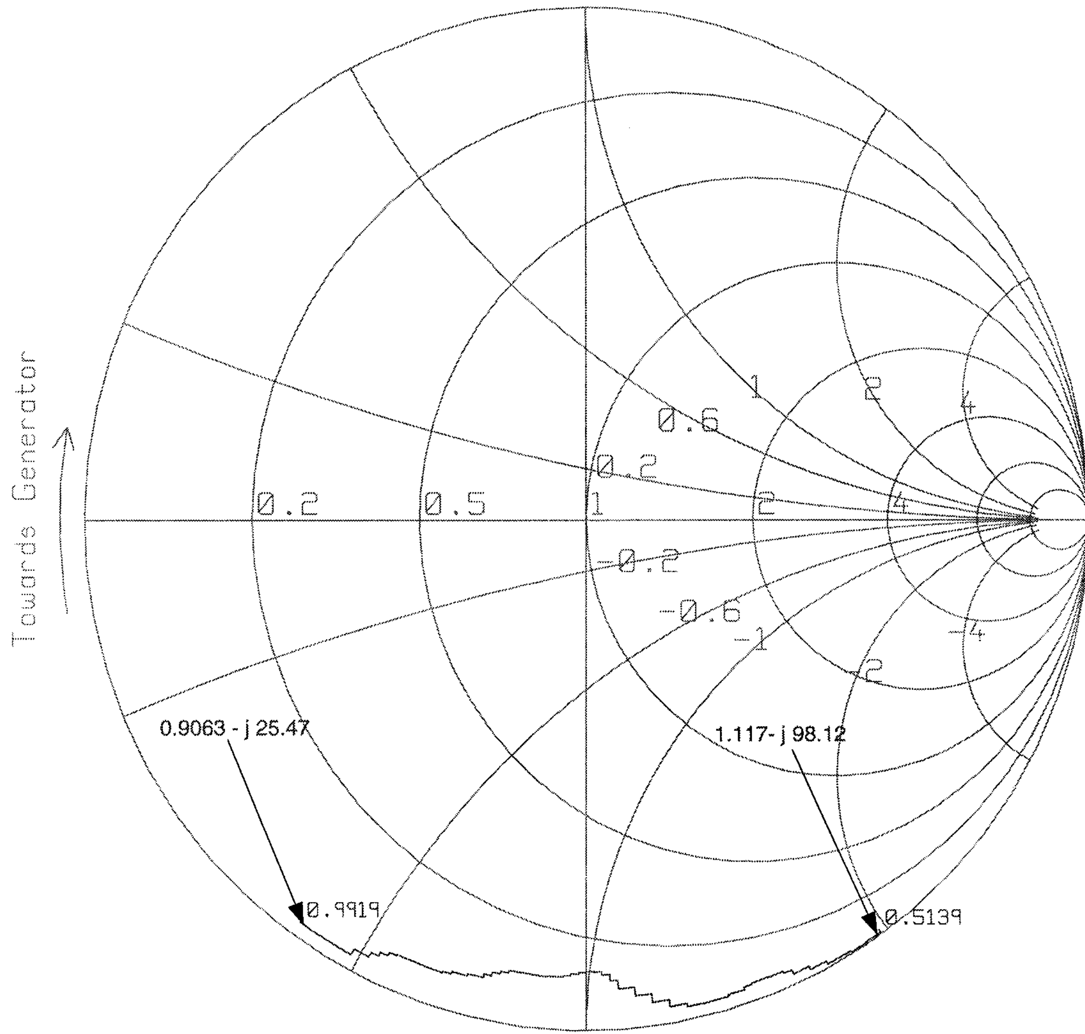

Fig. 4.17 Measured S11 parameter for the MEMS capacitor

Chapter 5

Conclusions, Contributions and Future Work

5.1 Conclusions

In this thesis, we have studied and analyzed the theory, modeling, simulation, design, and finally fabrication of MEMS filters for RF applications. We covered microelectromechanical filters based on MEMS resonators and also RF MEMS variable capacitors which can be used in constructing RF filters. Several new MEMS resonator designs have been documented in chapter 3. The microelectromechanical filters were fabricated using the multi user silicon surface micromachining process, PolyMUMPs.

A lumped-element modeling approach based on the principles of electromechanical analogy was used to study the multi-domain physics of the filters. Three different modeling approaches were used in developing the lumped-element macromodels; small-signal, large-signal, and reduced order modeling or ROM. Then behavioral description of the MEMS resonators were used along with the sensing and biasing circuitry in a unique VHDL-AMS simulator to perform a system-level simulation of the band-pass filters.

In chapter 3 we also introduced the MEMS integration concept through the design and fabrication of a MEMS variable capacitor using a standard TSMC CMOS 0.35μm technology. This capacitor is fully CMOS compatible and after fabrication it just needs a single mask post-processing step which has been presented in detail. In order to completely remove the silicon substrate, another dry etching step is required which will be considered as a future work.

Finally we studied different test and measurement techniques in chapter 4 and we discussed on the measurement results for the MEMS resonators. The testing of the MEMS resonators involves the determination of their resonance frequency. The described test setup in this work can be used in characterizing resonators with frequencies up to 10MHz and for the higher frequency MEMS resonators we have proposed two other measurement methods; fiber optic interferometery and RF probing using a network analyzer.

5.2 Contributions

The main contributions of this research work are listed as follows

(1) Design and fabrication of several MEMS resonators:

The theory, modeling, and design of clamped-clamped, cantilever, and disk resonators have been covered and then we proposed lumped mechanical and electrical models for these resonators. The simulation results using the electrical models with SPICE are very close to the ones obtained by FEM. Then by taking the design rules and the limitations of the fabrication technology into account, the resonators have been fabricated.

(2) Developing the behavioral macromodels of MEMS resonators:

In this work we proposed two different behavioral models for the MEMS resonators which could be used in VHDL-AMS simulators for system-level simulation of a band-pass microelectromechanical filter. One is based on the behavioral description of the electrostatic transducer and the other is based on the reduced order modeling of the clamped-clamped resonators. The functionality of these models in non-linear and large-signal simulation of the band-pass filter have been proven by performing a Fourier analysis which is impossible using the FEM with ANSYS. Besides the large-signal modeling capability, another importance of these modeling techniques is the possibility of integration of these models of MEMS devices with other digital and analog circuits in order to simulate the whole system on chip which contains MEMS components.

(3) Design and fabrication of band-pass filters:

We considered two different coupling configurations for the mechanically coupled resonators within a band-pass filter and as explained through the simulation results, the closed ring configuration results in a symmetric frequency response. For the fabricated bend-pass filters we have used this coupling method.

(4) Design of a novel parallel plate MEMS variable capacitor:

The capacitor has been fabricated using the standard 0.35μm CMOS technology and demonstrates the possibility of the MEMS integration with electronic circuitry into an RF module. Post-processing steps have been performed on the fabricated chips in order to create the air gap between the parallel plates and also to remove the lossy silicon substrate under the device. The previous MEMS variable capacitors implemented in the

CMOS technology all use the comb-finger configuration and in this work, for the first time we have fabricated a MEMS variable capacitor using the parallel-plate configuration.

(5) Publications related to this work:

- S. Fouladi, A. Hajhosseini and M. Kahrizi, "System-Level Modeling and Simulation of Microelectromechanical Filters", IEEE International Conference on Systems, Signals and Devices, SSD2005, Tunesia, March 2005.
- S. Fouladi, A. Hajhosseini and M. Kahrizi, "Behavioral Modeling of Microelectromechanical Filters", International Conference of Physics and Control, PhysCon2005, Saint-Petersburg, August 2005.

5.3 Future Work:

The work presented in this thesis can be subject to further study and analysis as a future work

(1) Precise characterization of the MEMS resonators using the fiber optic interferometer and wafer probing with special RF probes and network analyzer. The first method is a non-contact measurement method and result in a very accurate measurement of the resonance frequency.

(2) Investigation of the stability of the MEMS resonators, for example considering the shift in resonance frequency due to the variations in the operating temperature and also the pressure of the measurement ambient and modification of the design to improve the stability.

(3) Characterization of the cantilever, disk and the band-pass filters which are fabricated with the second PolyMUMPs run using the measurement methods which have been discussed before.

(4) For the MEMS variable capacitors as explained another post-processing step is required to completely etch the silicon under the device. For this post-processing step we will use the dry isotropic etching method using XeF_2.

(5) Test and characterization of the MEMS variable capacitor using the RF test board and also RF wafer probing after the final post-processing step which explained above. For the available network analyzer we can not apply any DC voltage to the test port and this limitation could be resolved by using a bias-tee and then we can measure the capacitance

under different actuation voltages to find the C-V characteristic of the variable MEMS capacitor.

(6) Design and fabrication of MEMS inductors using the standard CMOS and PolyMUMPs technologies and then combining these inductors with the fabricated MEMS variable capacitors to implement RF integrated filters.

References

[1] E. R. Brown, "RF-MEMS Switches for Reconfigurable Integrated Circuits", *IEEE Transactions on Microwave Theory and Techniques,* vol. 46, no. 11, pp. 1868-1880, November 1998

[2] V. K. Varadan, K. J. Vinoy, and K. A. Jose "RF MEMS and Their Applications", Wiley, New York, 2003

[3] Y. Liu, "MEMS and BST Technologies for Microwave Applications", Ph.D. Thesis, University of California, Electrical and Computer Engineering department, September 2002

[4] Y. Sun, H. Van Zelj, J. L. Tauritz, "Suspended Membrane Inductors and Capacitors for Application in Silicon MMICs", *Microwave and Milimeter-Wave Monolithic Circuits Symposium,* pp. 99-102, Jun 1996

[5] J. B. Yoon, B. K. Kim, C. H. Han, E. Yoon, and C. K. Kim, "Surface Micromachined Solenoid On-Si and On-Glass Inductors for RF Applications", *IEEE Electron Device Letters,* vol. 20, no. 9, pp. 487-489, September 1999.

[6] A. Dec, and K. Suyama, "Micromachined Electro-Mechanically Tunable Capacitors and Their Applications to RF IC's", *IEEE Transactions on Microwave Thory and Techniques,* vol. 46, no. 12, pp. 2587-2596, December 1998

[7] R. L. Borwick, P. A. Stupar, J. F. DeNatale, R. Anderson, and R. Erlandson, "Variable MEMS Capacitors Implemented Into RF Filters Systems", *IEEE Transactions on Microwave Theory and Techniques,* vol. 51, no. 1, pp. 315-319, January 2003

[8] R. A. Johnson, "Mechanical Filters in Electronics", Wiley, New York, 1983

[9] F. D. Bannon, J. R. Clark, and C. T.-C. Nguyen, "High-Q HF Microelectromechanical Filters", *IEEE Journal of Solid-State Circuits,* vol. 35, no. 4, pp. 512-526, April 2000

[10] K. Wang, A. C. Wong, and C. T.-C. Nguyen, "VHF Free-Free Beam High-Q Micromechanical Resonators", *IEEE Journal of Microelectromechanical Systems,* vol. 9, no. 3, pp. 347-360, September 2000

[11] W. T. Hsu, J. R. Clark, and C. T.-C. Nguyen, "Q-Optimized Lateral Free-Free Beam Micromechanical Resonators", *11th International Conference on Solid-State Sensors and Actuators,* pp. 1110-1113, June 2001

[12] J. R. Clark, W. T. Hsu, C.T.-C. Nguyen, "High-Q VHF Micromechanical Contour-Mode Disk Resonator", *International Electron Devices meeting,* pp. 493-496, December 2000

[13] S. Pourkamali, and F. Ayazi, "SOI-Based HF and VHF Single-Crystal Silicon Resonators with SUB-100 nanometer Vertical Capacitive Gaps", *The 12th International Conference on Solid-State Sensors, Actuators and Microsystems,* pp. 837-840, June 2003

[14] B. Bircumshaw, G. Liu, H. Takeuchi, T.-J. King, R. Howe, O. O'Reilly, and A. Pisano, "The Radial Bulk annular Resonator: Towards a 50W RF MEMS Filter", *12th International Conference on Solid-State Sensors, Actuators, and Microsystems,* pp. 875-878, June 2003

[15] K. Wang, and C. T.-C. Nguyen, "High-Order Medium Frequency Micromechanical Electronic Filters", *IEEE Journal of Microelectromechanical Systems,* vol. 8, no. 4, pp. 534-557, December 1999

[16] R. Gabriel M. "RF MEMS Theory, Design, and Technology", Wiley, NJ, 2003

[17] H. T. Kim, J. H. Park, S. Lee, S. Kim, J. M. Kim, Y. K. Kim, and Y. Kwon, "V-Band 2-b and 4-b Low-Loss and Low-Voltage Distributed MEMS Digital Phase Shifter Using Metal-Air-Metal Capacitors", *IEEE Transactions on Microwave Theory and Techniques,* vol. 50, no. 12, pp. 2918-2923, December 2002

[18] R. Simons, "Coplanar Waveguide Circuits, Components, and Systems", Wiley, New York, 2003

[19] V. Milanovic, M. Gaitan, E. D. Bowen, and Mona E. Zaghloul, "Micromachined Coplanar Waveguides in CMOS Technology", *IEEE Microwave and Guided Wave Letters,* vol. 6, no. 10, pp. 380-382, October 1996

[20] V. Gaitan, M. Bowen, E. D. Tea, N. H. Zaghloul, "Design and Fabrication of Micromachined Passive Microwave Filtering Elements in CMOS Technology" *International Conference on Solid-State Sensors and Actuators,* pp. 1007-1010, June 1997

[21] G. T. A. Kovacs, N. I. Maluf, and K. E. Petersen, "Bulk Micromachining of Silicon", *Invited Paper, Proceedings of the IEEE,* vol. 86, Issue 8, pp. 1536-1551, August 1998

[22] K. Boustedt, K. Persson, D. Stranneby, "Flip Chip as an Enabler for MEMS Packaging", *IEEE International Conference on Electronic Components and Technology,* pp. 124-128, 2002

[23] S. Gary, "Trends in micromechanics: micron machinations" Scientific American, November 1992

[24] K. Peterson, P. Barth, J. Poydock, J. Brown, J. Mallon, J. Bryzek, "Silicon Fusion Bonding for Pressure Sensors", *IEEE Technical Digest on Solid-State Sensors and Actuators Workshop,* pp. 144-147, June 1988

[25] "PolyMUMPs Design Handbook", MEMSCAP, Revision 10.0

[26] "CMC CMOS 0.35 technology Kit"

[27] G. T. Mulhem, D. S. Soane, and R. T. Howe, "Supercritical Carbon Dioxide Drying of Microstructures", Transducers' 93, Yokahama, Japan, pp. 296-299, June 1993

[28] J. H. Lau, "Flip chip technology", McGraw-Hill, New York, 1995

[29] R. Irvin, Z. Wenge, K. Harsh, and Y. C. Lee, "Quick Prototyping of Flip Chip Assembly with MEMS", *IEEE International Conference on Radio and Wireless Systems,* pp. 293-296, August 1998

[30] M. Behera, S. De, N. Aluru, and K. Mayaram, "A Coupled Circuit and Device Simulator for Design of RF MEMS VCOs", *3rd IEEE International Conference on Nanotechnology,* pp. 347-350, August 2003

[31] E. Christen, and K. Bakalar, "VHDL-AMS A Hardware Description Language for Analog and Mixed-Signal Applications", *IEEE Transactions on Circuits and Systems II: Analog and Digital Signal Processing,* vol. 46, Issue 10, pp. 1263-1272, October 1999

[32] D. Muller, and W. Dotzel, "Analyzing and Simulation of MEMS in VHDL-AMS Based on Reduced Order FE-Models", *IEEE Proceedings on Sensors,* vol. 2, pp. 866-871, October 2003

[33] A. C. H. Tilmans, "Equivalent circuit representation of electromechanical transducers: I. Lumped-parameter systems", *Journal of Micromechanics and Microengineering,* vol. 6, pp. 157-176, 1996

[34] A. C. H. Tilmans, "Equivalent circuit representation of electromechanical transducers: II. Distributed-parameter systems", *Journal of Micromechanics and Microengineering,* vol. 7, pp. 285-309, 1997

[35] P. V. Nikitin, C. R. Shi, and B. Wan, "Modeling Partial Differential Equations in VHDL-AMS", *IEEE International Conference on System on Chip,* pp. 345-348, September 2003

[36] D. M. Pozar, "Microwave Engineering", Wiley, New York, 1998

[37] F. D. Bannon, J. R. Clark, C. T.-C. Nguyen, "High-Q HF microelectromechanical Filters", *IEEE Journal of Solid-State Circuits,* vol. 35, no. 4, pp. 512-526, April 2000

[38] W. Weaver, "Vibration Problems in Engineering", Wiley, New York, 1990

[39] J. J. Thomsen, "Vibrations and Stability, Advanced Theory, Analysis, and Tools", Springer, New York, 2003

[40] F. S. Tse, "Mechanical Vibrations, Theory and Applications", Allyn and Bacon, Boston, 1978

[41] W. Flugge, "Handbook of Engineering Mechanics", McGraw-Hill, New York, 1962

[42] H. H. Woodson, "Electromechanical Dynamics Part I, II and III", Wiley, New York, 1968

[43] L. Meirovitch, "Elements of Vibration Analysis", McGraw-Hill, New York, 1986

[44] D. S. Greywall, and P. A. Busch, "Coupled micromechanical drumhead resonators with practical application as electromechanical bandpass filters", *Journal of Micromechanics and Microengineering,* vol. 12, pp. 925-938, 2002

[45] M. Konno, S. Oyama, and Y. Tomikawa, "Equivalent Electrical Networks for Transversely Vibrating Bars and Their Applications", *IEEE Transactions on Sonics and Ultrasonics*, vol. SU-26, no. 3, pp 1140-1152, May 1979

[46] S. Fouladi, A. Hajhosseini, and M. Kahrizi, "System-Level Modeling and Simulation of Microelectromechanical Filters", *IEEE International Conference on Systems, Signals, and Devices,* March 2005

[47] B. Romanowicz, M. Laudon, P. Lerch, P. Renaud, H. P. Amann, A. Moser, and F. Pellandini, "Modeling and Simulation of Electromechanical Transducers in Microsystems using an Analog Hardware description Language", *European Design and Test Conference,* pp. 119-123, March 1997

[48] P. J. Ashenden, "The System Designers Guide to VHDL-AMS, analog, mixed-signal and mixed-technology modeling", Morgan Kaufmann, 2003

[49] B. Romanowicz, M. Laudon, P. Lerch, P. Renaud, H. P. Amann, A. Boegli, V. Moser, "Analyzing and Simulation of MEMS in VHDL-AMS Based on Reduced Order FE-Models", *European Design and Test Conference,* pp.866-871, March 1997

[50] F. Bebbini, J. Mehner, W. Dotzel, "Computational Methods for Reduced Order Modeling of Coupled Domain Simulations", *11th International Conference on Solid-State sensors and Actuators,* pp. 260-263, 2001

[51] B. Romanowicz, "Methodology for the Modeling and Simulation of Microsystems", Kluwer, Boston, 1998

[52] C. Goldsmith, A. Malczeewski, Z. J. Yao, S. Chen, J. Ehmke, D. H. Hinzel, "RF MEMS Variable Capacitors for Tunable Filters", *International Journal of RF and Microwave Computer-Aided Engineering,* vol. 9, no. 4, pp. 362-374, July 1999

[53] D. S. Senturia, "Microsystem Design",Kluwer, Boston, 2001

[54] "PolyMUMPs faq document", MEMSCAP, Revision 1.0

[55] G. Xu, C. Zhang, and Q. Jiang, "Air-damping Effect on a Micro- and Nano-machined Beam Resonator" *Tech. Proc. of MSM 2000,* pp. 579-582, Chapter 13

[56] D. Bindel, S. Govindjee, "Elastic PMLs for Resonator Anchor Loss Simulation", Technical Report, Department of Civil and Environmental Engineering, University of California, Berkeley, February 2005.

[57] A. Dec, and K. Suyama, "Micromachined Electro-Mechanically Tunable Capacitors and their applications to RF IC's", *IEEE Transactions on Microwave Theory and Techniques,* vol. 46, no. 12, pp. 2587-2596, December 1998

[58] G. K. Fedder, S. Santhanam, M. L. Reed, S. C. Eagle, D. F. Guillou, M. S.-C. Lu, and L. R. Carley, "Laminated High-Aspect-Ratio Microstructures in a Conventional CMOS Process", *IEEE 9th International Workshop on 'An Investigation of Micro Structures, Sensors, Actuators, Machines and Systems',* pp. 13-18, February 1996

[59] H. Xie and G. K. Fedder, "Fabrication, Characterization, and Analysis of a DRIE CMOS-MEMS Gyroscope", *IEEE Sensors Journal,* vol. 3, no. 5, pp. 622-631, October 2003

[60] X. Zhu, S. Santhanam, H. Lakdawala , H. Luo, and G. K. Fedder, "Copper Interconnect Low-K Dielectric Post-CMOS Micromachining", *The 11th International Conference on Solid-State Sensors and Actuators,* pp. 1548-1551, June 2001

[61] "Characterization of Material Surface by Using Fiber Bragg Grating", Jun Chen, M.A.Sc Thesis, Department of Electrical and Computer Engineering, Concordia University, January 2005

[62] F. Larmer, A. Schilp, K. Funk, and C. Burrer, "Experimental Characterization of dynamic micromechanical transducers", *Journal of Micromechanics and Microengineering*, vol. 6, pp. 177-186, 1996

[63] "Printed Circuit Board Test Fixture For 80-Pin CFP User Guide", Version 1.0, Canadian Microelectronics Corporation